MICROFLUIDIC METHODS FOR THE CRYSTALLIZATION OF ACTIVE PHARMACEUTICAL INGREDIENTS

TOLDY ARPAD ISTVAN

B.Sc., Budapest University of Technology and Economics

A THESIS SUBMITTED FOR THE DEGREE OF DOCTOR OF PHILOSOPHY IN CHEMICAL AND PHARMACEUTICAL ENGINEERING

SINGAPORE-MIT ALLIANCE

NATIONAL UNIVERSITY OF SINGAPORE

2014

DECLARATION

I hereby declare that this thesis is my original work and it has been written by me in its entirety. I have duly acknowledged all the sources of information which have been used in the thesis. This thesis has also not been submitted for any degree in any university previously.

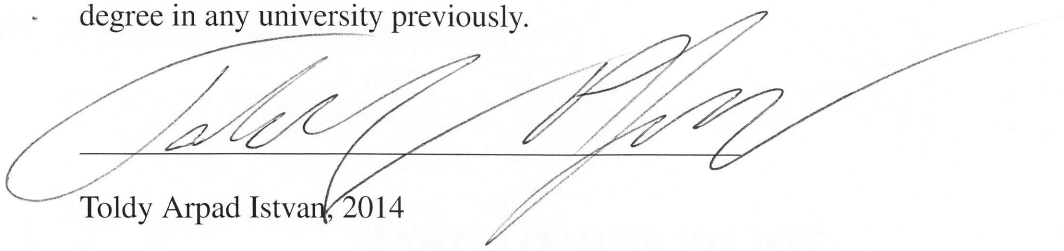

Toldy Arpad Istvan, 2014

”Lehúzol így pár évet, és amikor szabadulsz,
úgy tűnik a pár, hogy lepergett vagy húsz.“
Ganxsta Zolee

Acknowledgements

First and foremost, I would like to express my deepest gratitude to my advisors, Prof. Saif A. Khan and Prof. T. Alan Hatton for their invaluable guidance. I would like to thank my thesis examiners in advance for their valuable feedback. I would also like to thank my lab mates for making the Khan and the Hatton labs such fun places to be. At NUS, I would particularly like to thank Zita Zheng, Dr. Abu Z. Md. Badruddoza, Reno A. L. Leon, Zhang Chunyan, Anirudha Vishvakarma, Sanjay Saroj and our FYP students for all the work that we did together on crystallization. I thank Dr. Brian Crump of GSK for keeping our project in touch with the industry. I'm greatly indebted by David Conchouso, David Castro and Prof. Ian G. Foulds from KAUST for providing us with robust PMMA emulsion generators and saving several hours of our lives that would have otherwise been spent on cursing at glass capillaries.

I am very thankful for having the opportunity to spend six amazing months at MIT. I owe a big thanks to Dr. Emily Chang for being my mentor and lab buddy; my eternal gratitude goes out to my American relatives, John, Matt&Amy, Janet&Mark and Öcsi&Edit for providing accommodation, advice, machine shop access, bicycles, brewing equipment, and generally whatever I needed. I would also like to thank Prof. Allan S. Myerson and Dr. Vilmali Lopez-Mejias for letting me use the Raman microscope.

I thank my family for all the support that I received during the past 27 years, and for believing in me. See? I made it. My loving wife, Ági, and my son, Miki deserve praise for enduring all the time that we had to spend far from each other. I promise that in the future, I will avoid places that make it prohibitive for us to be together.

I am blessed to have friends all over the world who keep in touch with me despite the distance; we shall meet soon.

An honorable mention goes out to all the artists and friends who unknow-

ingly helped me keep my sanity by reminding me of the 'outside world' through sports, music, movies, books, etc. I could not have made it without you.

Finally, I would like to thank the Chemical and Pharmaceutical Engineering Program of Singapore-MIT Alliance and the GSK-EDB Fund for Sustainable Manufacturing for the financial support.

Contents

List of Tables

List of Figures

List of Symbols

β	Compressed exponent
κ	Nucleation rate per droplet (s^{-1})
λ	Nucleation rate parameter (s^{-1})
σ	Interfacial tension between nucleus and solution
σ_{d_A}	Standard deviation of agglomerate diameter (μm)
τ	Nucleation time constant (s)
θ	Incident angle (XRD) (degrees)
θ_c	Contact angle (degrees)
χ	Diffusivity ratio
a	Activity
a_S	Activity at saturation
A	Classical nucleation theory parameter A ($m^{-3}s^{-1}$)
B	Classical nucleation theory parameter B
d	Diameter (μm)
d'	Shrinkage rate ($\mu m \cdot s^{-1}$)
d_0	Initial droplet diameter (μm)
d_A	Agglomerate diameter (μm)
d_c	Critical droplet diameter (μm)
d_m	Molecular diameter (nm)
D_{rot}	Rotational diffusivity (m^2s^{-1})
D_{tr}	Translational diffusivity (m^2s^{-1})
f_I	Fraction of Morphology I SAs
h_e	Effective film thickness (mm)
h_f	Continuous phase film thickness (mm)
J	Nucleation rate ($m^{-3}s^{-1}$)
k	Boltzmann constant ($J \cdot K^{-1}$)
n_{Cr}	Solid density (of glycine) ($kg \cdot m^{-3}$)

P_0	Probability of no nucleation observed in a droplet over time
P_n	Probability of n nuclei observed in a droplet over time
Q_{CP}	Continuous phase flow rate (μL·min^{-1})
Q_{DP}	Dispersed phase flow rate (μL·min^{-1})
Q_t	Total flow rate (μL·min^{-1})
r	Radius (μm)
S	Supersaturation
S_c	Critical supersaturation
t	Time (s)
t_c	Crystallization time (min)
t_r	Residence time (min)
t_s	Shrinkage time (s)
T	Temperature/set temperature ($^\circ$C)
T_B	Belt surface temperature ($^\circ$C)
T_{CP}	Continuous phase temperature ($^\circ$C)
v	Molecular volume (nm^3)
V	Volume (m^3)
v_b	Belt Velocity (cm/min)
w	Emulsion stream width (mm)
Y_e	Experimental productivity (g/day)
Y_t	Theoretical productivity (g/day)

Summary

Crystallization is one of the most important downstream processing steps of active pharmaceutical ingredients (APIs), signified by the fact that ∼90 % of all APIs are formulated as crystals. The outcome of crystallization is ideally a population of uniform particles of the desired crystalline form and a favorable habit that facilitates subsequent solid formulation steps. However, currently available API crystallization processes often fail to achieve this goal and require several energy-intensive and time consuming intermediate processing steps. Moreover, the recent industrial, regulatory and academic push for sustainability created a great need for new crystallization processes that facilitate intensified manufacturing. Emulsion-based crystallization techniques to produce spherical agglomerates (SAs) of API crystals are of great interest due to the favorable downstream processing properties of the particles produced by these methods. Still, the utility of emulsion-based crystallization is limited by the fact that it is typically performed in batch tanks, resulting in a polydisperse population of particles and a lack of knowledge regarding the formation mechanism of the individual SAs. While microfluidic devices are well known to be capable of generating monodisperse emulsions of various morphologies and compositions, their application to emulsion-based API crystallization has yet to be explored.

Work presented in this thesis brings together emulsion-based crystallization and droplet microfluidics to develop a scalable, continuous API crystallization platform that robustly produces SAs of unprecedented uniformity. First, an overview of the existing body of relevant literature is given in Chapter 1. Subsequently, in Chapter 2 a semi-batch spherical crystallization platform is presented. This platform coupled monodisperse microfluidic emulsion generation with off-chip thin-film evaporation to produce uniform SAs of glycine, a model API molecule. On-line microscopic monitoring of the crystallization pro-

cess enables the delineation of the distinct phases of SA formation: shrinkage, stochastic nucleation, spherulitic growth and agglomerate aging. Next, Chapter 3 presents experimental studies and mathematical modeling to determine the effect of operating conditions on the morphological outcome of a thin-film spherical crystallization process. It is found that droplets must first shrink to a critical size before nucleation occurs to form complete SAs, whereas the opposite leads to the formation of incomplete agglomerates or single crystals. Insights gained in this study provide valuable guidelines for the design of similar processes in the future. A proof of concept continuous thin-film evaporator to complement continuous microfluidic emulsion-generation is presented in Chapter 4. This apparatus is capable of producing $\sim$1-10 g/day of high quality SAs with a volumetric footprint of only $\sim$10 L, and can straightforwardly be scaled up to industrially relevant production rates by parallelization. Finally, Chapter 5 summarizes the future outlook of this platform: an example of a newly developed advanced formulation technique for hydrophobic compounds is discussed along with the technological challenges and scientific questions raised by the work presented herein.

1 Introduction

1.1 The Backdrop: Sustainable Manufacturing

In a broader context, this thesis addresses a gradually arising, yet urgent issue, the strive for sustainability in pharmaceutical manufacturing, both in the environmental and the economic sense. Sustainability in the context of the pharmaceutical industry manifests itself in ”green chemistry” and ”green engineering” principles, and essentially refers to choosing the process with the lowest possible economic and environmental footprint (i.e. the one that requires less raw materials - including energy - and produces less hazardous waste) [1]–[3]. The emergence of this push for sustainable manufacturing is the natural consequence of rising drug development costs [4]. Since product development - which includes the manufacturing process - can account for as much as 35% of drug development costs [5], streamlining manufacturing processes could save both financial and environmental resources. This is especially true if one considers that due to the unique characteristics of pharmaceutical process development - the goal is to get a marketable product in the smallest possible time frame, as opposed to robust, long-term manufacturing solutions [5], [6] - advances have been lagging behind other industries. So much so, that a 2003 article in the *Wall Street Journal* mocked drug manufacturing for being less advanced than the processes for making potato chips and laundry detergents [7], and a 2004 white paper released by the FDA called for a shift from ”art-based” empirical methods to rigorous, science-based process development [8]. Having realized that conventional processes and empirical process development methods have reached their limits, both academia and industry started looking for more advanced options [9].

Recent developments spawned by these efforts include the emergence of rational design approaches aided by advanced process analytical techniques [10], [11] and a massive push for process intensification - in which the footprint of a

given process is dramatically reduced while retaining the original output [12]. Two emerging technological solutions for process intensification, continuous manufacturing and microreactors are at the forefront of these recent advances, culminating in an end-to-end continuous plant of aliskiren hemifumarate built by the Novartis-MIT Center for Continuous Manufacturing [13], [14]. In this first of a kind demonstration, the authors highlighted two main advances as the most important factors in achieving their goal: 1) novel continuous processes and pieces of equipment [13]; 2) the integration of cascaded continuous processes aided by process analytical tools and control loops [15]. This thesis focuses on the former, in the context of pharmaceutical crystallization.

1.2 Pharmaceutical Crystallization

Crystallization, the process in which crystalline solids are precipitated, typically from a supersaturated solution, is one of the most prominent downstream processing steps in the manufacturing of active pharmaceutical ingredients (APIs) [16]. Its importance is signified by the fact that more than 90% of APIs are formulated as crystals [17]. Ideally, the output of crystallization is a population of particles with a narrow size distribution, uniform shape and of the desired crystalline form [18], [19]. Such a particle population possesses the advantage of 'direct tablettability' and requires little or no additional unit operations before formulating the solid dosage [20]. However, achieving such an exquisite control is rarely possible, as crystallization is an extremely complex phenomenon, and our understanding of the underlying physics is still limited.

Conceptually, the process of crystallization is separated into two phases: nucleation and growth [21]. In practice, this demarcation is used to indicate the dominant mechanism of solid mass generation in a crystallization process [18]. The first phase, nucleation, refers to the formation of 'nuclei', i.e. clusters of a new, thermodynamically more stable phase that are large enough to grow spontaneously over time. According to the commonly used Classical Nucleation Theory (CNT), the surface energy required to form a new phase competes with

the free energy gain from phase transformation, resulting in a critical size above which the further growth of the cluster results in a reduction of overall free energy. Such clusters then tend to grow spontaneously [22], [23]. The rate of formation of these clusters - the rate of nucleation - in a supersaturated solution depends on chemical composition and temperature [23]:

$$J = AS\exp\left(-\frac{B}{\ln^2 S}\right) \tag{1.1}$$

where J is the rate of nucleation in $\mathrm{m}^{-3}\mathrm{s}^{-1}$, A is a (temperature-dependent) pre-exponential factor (also in $\mathrm{m}^{-3}\mathrm{s}^{-1}$), B is a kinetic barrier term that depends on temperature and molecular properties and S is supersaturation, defined as a/a_S where a is the actual activity of the solute, and a_S is the activity of the solute at saturation [23], [24]. The calculation of these parameters will be discussed in Chapter 3 in detail. Figure 1 shows how this steep dependence is exploited in the most widely employed strategy to control particle size distribution in crystallization: if the process starts out with a comparatively high supersaturation, a large number of individual nuclei form, and subsequent crystal growth yields a population of smaller particles as the solute is being depleted from the solution (i.e. nucleation is the dominant mechanism of solid mass generation [18]). On the other hand, a lower initial supersaturation results in a smaller number of nuclei that can grow into larger crystals. This simple principle to control particle size distribution is at the heart of most highly optimized industrial crystallization processes that typically involve the temporal variation of supersaturation in the form of heating and cooling cycles or a separate 'nucleation' and 'growth' stage [25], [26]. However, the sheer number of variables still makes crystallization more of an empirical endeavor than rigorous science, even if only the aspect of nucleation is considered first. To start with, the validity of CNT is limited [27], [28], as there are known cases of solutes exhibiting multiple regimes of the J - S relationship and solutes that experience a radical drop in nucleation rate at high supersaturations [18], [29]. Secondly, the presence of

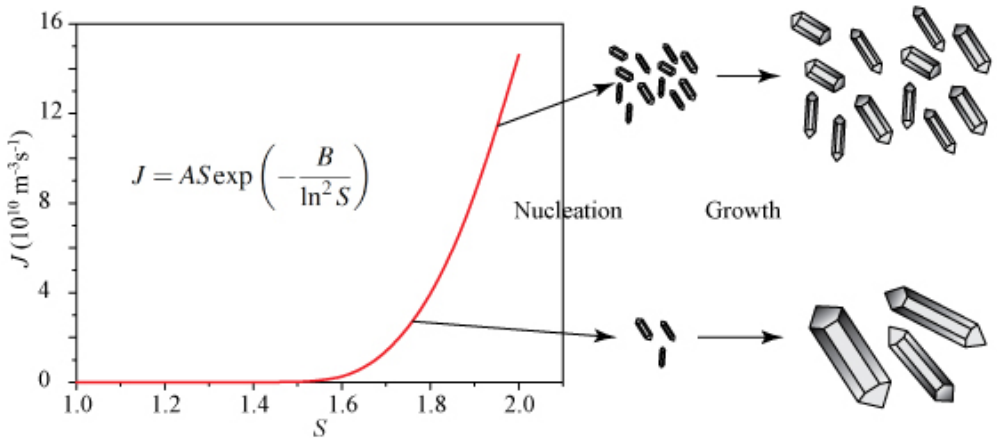

Figure 1: Schematic of the most commonly employed strategy to control crystal size distribution: if crystallization is performed at a high initial supersaturation, a large amount of nuclei form, leading to a population of smaller crystals. On the other hand, crystallization at lower initial supersaturation values produces few nuclei which then grow into larger crystals [18].

a heterogeneous interface within a supersaturated solution greatly reduces the free energy barrier for nucleation, thereby increasing nucleation rate [22]. This implies that crystallization performed in a large vessel (be it a stirred batch tank or a plug-flow reactor) is very likely to proceed via heterogeneous nucleation on the vessel wall or impurities rather than homogeneous nucleation in solution [30]. While the complete elimination of these unwanted impurities is usually not feasible, adding ”impurities” or *seeds* to template crystallization is a well established means of controlling size distribution and crystalline form [18]. Polymorphism, the ability of a single compound to exhibit multiple crystalline packing arrangements, poses the final - and arguably the most formidable - challenge in understanding and controlling nucleation. Different crystalline polymorphs of the same molecule can have dramatically different downstream properties, some of which directly affect the engineering and economic feasibility of a process - such as their powder properties - while others influence the shelf life and the *in vivo* performance of the drug - such as their stabilities and dissolution rates [31]. Despite recent advances in the subject, most notably in templating [32], [33] and nucleation in confined spaces [34]–[39], there is still no generally applicable and robust method to predict and control polymorphism for a new

compound [40], and even extensive screening exercises are known to miss more stable or more desirable forms which can then incidentally appear and disrupt an approved manufacturing process [41]. In addition, the appearance of multiple polymorphs under the same nominal experimental conditions, concomitant polymorphism [37], [42], is a very common phenomenon in API crystallization, especially in molecules that have several polymorphs of nearly identical stabilities (typically these are APIs that exhibit conformational polymorphism [43]). To make matters even worse, some polymorphs tend to transform into more stable ones in the solid state [44] or in the presence of solvent [45], the prevention of which is of paramount importance in the final formulation of solid dosage forms. Therefore, until these issues all get resolved, the development of a crystallization process for a polymorphic compound still retains its artistic aspect [31].

After nuclei form, crystal growth takes place. This step controls the final morphology and habit of crystals. The morphology of a crystal is determined by the facets present in the given crystal form, while crystal habit is determined by the relative growth rates of these facets - i.e. the facets that grow slower are the *largest* facets of a crystal [21]. The presence of disproportionately rapid-growing facets can lead to needle-, blade- or plate-like crystals [21], [46]. Since these habits tend to result in inferior downstream properties (such as longer filtration times, poor packability, compactability and flowability), they are generally undesirable from a processing standpoint [18], [47]. Crystal habit (i.e. the growth rate of facets) can be controlled by the rational design of intermolecular interactions between crystal facets, growth units, the solvent and additives in an academic setting [48]–[51]. In practice, however, the semi-empirical approach of solvent screening is still the most widely used technique to regulate crystal habit [18].

Despite all the efforts and techniques discussed above, many currently available API crystallization processes still yield acicular or blade-like particles.

Therefore, the downstream process of transforming these crystals into a marketable form (such as tablets) often requires milling and comminution to produce uniform crystals of the desired size [52]–[54]. These steps are not only energy intensive, but can result in complications, such as solid-state polymorphic transformation [55]. Next, the resulting crystals are typically blended with excipients, another step that, beside being stochastic in nature [56], is not fully understood in terms of API-excipient interactions [57]–[59]. Finally, the granulation of the API-excipient particles to a tablettable solid form is yet another energy- and time consuming step that might result in excessive dust formation in the case of dry granulation [60] or undesirable polymorphic transformations during wet granulation [61]. To avoid at least some of these additional processing steps, one would require a powder with superior flowability, packability, and compactability. The next section introduces a technique that is capable of producing such powders: emulsion-based crystallization.

1.2.1 Emulsion-based Crystallization

History, Categorization and Applications

Emulsion-based crystallization is the process in which crystallization occurs in the presence of an emulsion (i.e. a dispersed liquid phase within an immiscible continuous phase) that can be stable, metastable, or transient. The technique arose in 1982, when Kawashima *et al.* applied their insights of spherical aggregation of sands in presence of a bridging liquid [62] to API crystals, and defined a solvent-antisolvent-bridging liquid system for salicylic acid to produce spherical crystalline agglomerates (SAs) [63]. Although in their study crystallization was performed before the bridging liquid was added to form the emulsion and bring the individual crystals together, this piece of work inspired much of the emulsion-based API crystallization methods that have been developed since then. These techniques can be divided into four major categories: spherical agglomeration (Kawashima's method), (quasi-) emulsion solvent diffusion, evapo-

rative emulsion crystallization, and melt crystallization from emulsions. Figure 2 describes the differences between these techniques.

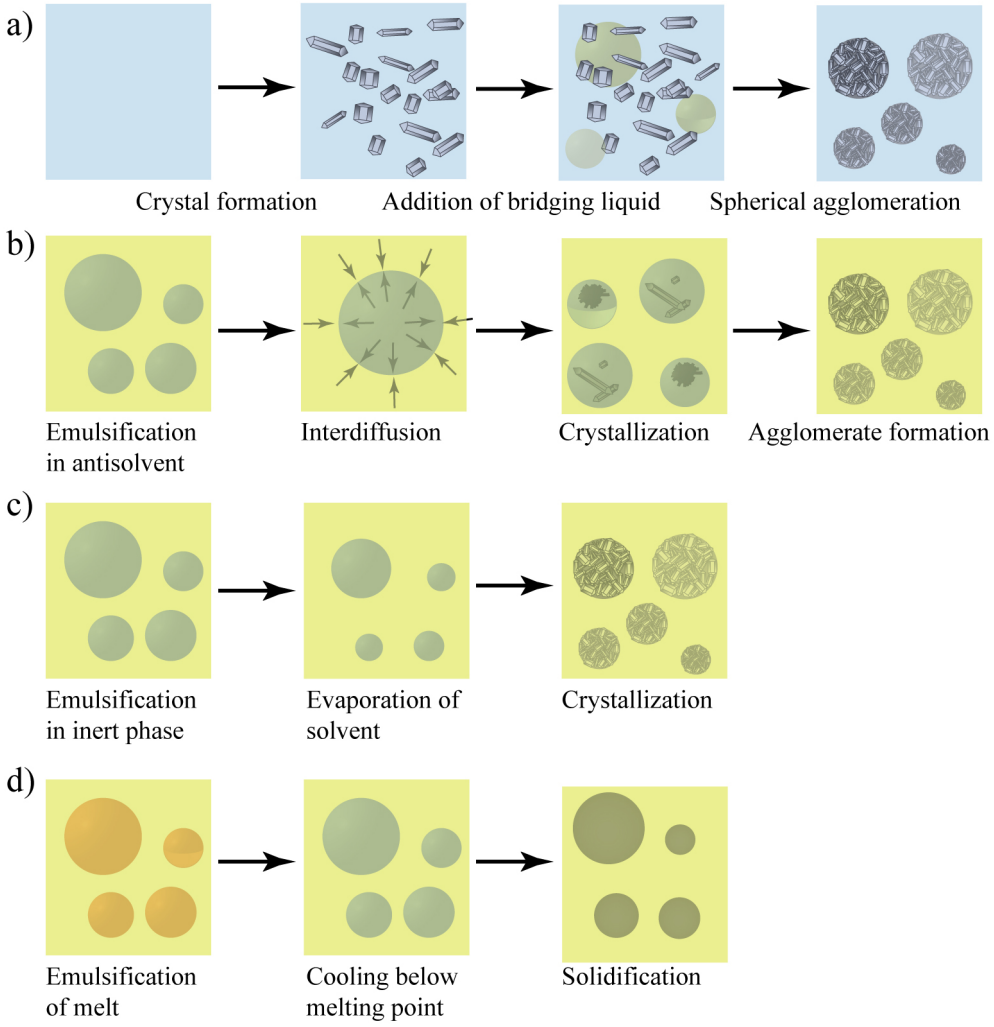

Figure 2: Schematic explaining the differences between the four major categories of emulsion-based crystallization: a) spherical agglomeration, b) emulsion solvent diffusion or quasi-emulsion solvent diffusion, c) evaporative crystallization, d) emulsion-based melt crystallization.

In spherical agglomeration, crystals are pre-formed by cooling, antisolvent addition, or reactive crystallization, and a bridging liquid is added to form an emulsion [63]–[65]. This bridging liquid is selected so that it preferentially wets the formed crystals which then aggregate via two possible mechanisms, depending on the size of the bridging liquid droplets, and therefore, agitation : 1) if the droplets are significantly larger than the crystals, crystals will partition into the droplets, and spherical particles form (shown on Figure 2a); 2) in all

other cases, aggregation happens via the coalescence of droplets on the surface of the crystals, producing irregular agglomerates [64]. Owing to its relatively well understood mechanism, spherical agglomeration remains the most popular emulsion-based API crystallization technique. Solvent-bridging liquid systems have been developed for an extensive variety of API molecules (e.g. naproxen [66], ibuprofen [67], aspirin [68] - see Table 1 of reference [65] for more examples).

Emulsion solvent diffusion or quasi-emulsion solvent diffusion (ESD or QESD), shown in Figure 2b, relies on a completely different mechanism of agglomerate formation. In this technique, the API solution is dispersed in a partially (ESD) or completely miscible phase (QESD) that contains the antisolvent [69]–[71]. While in the case of QESD these emulsions are transient - hence the name - supersaturation is typically achieved rapidly by the inter-diffusion of the solvent and the antisolvent between the two phases, and crystallization occurs within or at the surface of the droplets. According to a series of extensive experimental and modeling analyses performed by Espitalier *et al.*, the final agglomerate structure is determined by an interplay of heat and mass transfer and the hydrodynamics in the system [72], [73]. Their study suggests that beside the ratio and the relative temperatures of the two phases [72] the presence of internal circulation within the emulsion droplets above a critical radius (~450 μm) is necessary for a homogeneous supersaturation profile and a homogeneous agglomerate structure, whereas the opposite leads to core-shell structures [73]. Akin to spherical agglomeration, the ESD and QESD methods have successfully been applied to a wide variety of molecules [74]–[77]. Aside from the host of QESD systems, a very innovative ESD study was carried out by Tanaka *et al.*, where aqueous solutions (of glycine or sodium chloride) were atomized and sprayed directly into an antisolvent (1-butanol or 2-butanone), resulting in compact SAs [78]. Finally, several studies of ESD and QESD show that the presence of phase boundaries lends itself to the exploration of surface-active additives to

control the outcome of the process. Firstly, because QESD relies on transient emulsions, the short term stability of these emulsions is of great importance in forming spherical particles - Teychene and Biscans even contend that it is impossible to perform QESD-type spherical crystallization without additives due to secondary agglomeration (SAs sticking together) in their absence [79]. On the other hand, these additives can also play additional roles, such as influencing the habit or polymorphic form of crystals that constitute the SAs [80].

The third emulsion-based crystallization technique, evaporative crystallization, is also the most relevant for this thesis (Figure 2c). Here, the API solution is dispersed as droplets in an immiscible continuous phase. Subsequent evaporation of the solvent through the continuous phase leads to crystallization within the droplets. Interestingly, this conceptually straightforward method generated only a few studies after surfacing in 1993 when Sjostrom *et al.* used it to crystallize a hydrophobic drug from an oil-in-water emulsion [81], [82]. Later on, the Davey group applied the technique to aqueous solutions of glycine. In their 2002 paper they demonstrated that the dimensions of the emulsion generated can affect both spherical agglomeration and polymorphic outcome: in macroemulsions they produced SAs of the β polymorph, while in microemulsions and lamellar phases single crystals of the stable γ polymorph could be obtained [83]. Their 2009 study, which is one of the starting points of this thesis, investigates the role of operating conditions and surface-active additives in the batch emulsion-based crystallization of three water-soluble molecules (ephedrine, glutamic acid hydrochloride and glycine) [84]. They found that crystallization in such batch systems typically takes several hours, and vigorous stirring is necessary to obtain agglomerates of a reliable quality. In the case of glycine, some surfactants, particularly CTAB could largely improve the structure of the SAs obtained while controlling the polymorphic outcome (increasing the fraction of β-glycine in a mixture of the α and β polymorphs) [84]. This example shows that evaporative emulsion-based crystallization also lends great opportunities for

the exploration of additives to control SA structure and polymorphic outcome. Beside the studies mentioned above, our group explored functionalized silica nanoparticles as a means of polymorphic control in the emulsion-based crystallization of glycine. It was found that by appropriate selection of nanoparticle surface properties (in this case, surface charge) the glycine-glycine and glycine-surface interactions could be tuned to achieve polymorphic control [85].

Finally, melt crystallization from emulsions (Figure 2d) bears both historical, scientific and industrial relevance. In this technique, the dispersed phase of the emulsion is a melt, and supersaturation is induced by cooling the emulsion below the melting point. Historically, Vonnegut [86] was the first to point out that by splitting a metallic melt into a large number of small droplets allows for the decoupling of nucleation from growth (i.e. for one and only one nucleation event to occur per droplet) and Turnbull and Cech [87] realized that the number of droplets will be significantly greater than the number of impurities present in the system, thereby confining heterogeneous nucleation to a small fraction of the droplets. Thus, in such a system, one can study homogeneous nucleation.[1] While the study of nucleation kinetics certainly is one of the well-established applications of emulsion-based (melt) crystallization [89], the significance of Turnbull and Cech's finding with respect to emulsion-based crystallization is even greater from a purification standpoint: if the presence of impurities facilitates the formation of an undesirable side product, the confinement of the impurities to a few droplets will greatly increase the overall purity of the product. In the context of organic molecules, this concept was first applied by Davey *et al.* in 1995, when they purified a mixture of *meta*- and *para*-chloronitrobenzene below the eutectic by emulsion-based melt crystallization [90]. Naturally, this concept of superior purification also applies to (Q)ESD and evaporative emulsion-based crystallization. From an API-crystallization perspective, a superior quality of

[1] In this thesis, "homogeneous nucleation" refers to nucleation in the absence of extraneous impurities. However, it must be noted that nucleation almost always occurs at a surface of some sort [88].

the produced crystals reduces the number of downstream processing steps, leading to a more streamlined, less costly process. Outside this remarkable application, melt crystallization from emulsions is the subject of great interest in the food and cosmetics industry, where the solidification of emulsified fats can be a crucial determinant of the product quality [91] and where solid fat particles can be used for the delivery of active ingredients [92].

Advantages and Challenges

While the previous sections implied several advantages associated with emulsion-based crystallization, they are worth reiterating. To start with, the interest in emulsion-based API crystallization arose with the need for API crystals that have consistently good downstream powder properties: packability, flowability, and (direct) tablettability. Spherical agglomerates, formed from emulsions, are well known to exhibit these properties [74], [93], in addition to the superior bioavailability of the small individual crystals that make up the SAs [63], [94]. Secondly, the number of impurities in an emulsion is usually much smaller than the number of droplets. Therefore, impurities are confined to a minute fraction of the droplets, which results in a better overall product quality [90]. Next, the presence of a liquid-liquid phase boundary lends itself to the exploration of additives to control the outcome of the process [80], [83]–[85].

The main challenges associated with emulsion-based crystallization all arise due to the fact that these processes are typically performed in stirred batch tanks that are prone to inhomogeneities in operating conditions. These inhomogeneities influence the outcome in two ways: 1) polydisperse populations of SAs that will necessarily have non-uniform downstream properties [95], 2) there is no way to pinpoint the exact operating conditions under which individual SAs formed, which means that current knowledge regarding the mechanism of SA formation is typically based on *post factum* analysis of the product. These challenges call for platforms which enable both the production of monodisperse

emulsions and the on-line monitoring of SA formation. Fortunately, such platforms already exist, and are extensively used for the precise execution of unit operations both in academia and industry. An overview of these platforms, microfluidic systems, is presented in the next section.

1.3 Microfluidics

The general term 'microfludics' refers to the manipulation of minute amounts of fluids (in the nL-aL range) within channels of small dimensions ($<$1 mm) [96]. Microfluidic devices or microreactors are pieces of equipment that facilitate such manipulations. The extensive use of such devices for research purposes took off with the development of rapid prototyping techniques, most notably soft lithography [97]. Microfluidics offers a diverse toolbox of stationary and continuous flow unit operations that provide chemical engineers with distinct advantages over conventional synthetic and analytical processes. These advantages are all associated with the ease of control over processing parameters that is enabled by the small dimensions of microreactors. Firstly, due to the high surface to volume ratio of such small channels, reactions that require rapid heat transfer can be performed with ease - an early and extremely illustrative example is the application of a continuous flow microreactor to PCR (polymerase chain reaction), a reaction that requires several heating and cooling cycles [98]. Secondly, hydrodynamic flow in microfluidic channels is usually laminar, which enables an exquisite control over diffusive mixing times, allowing for interesting applications [99]. It can therefore be seen that microreactors are usually superior to their large-scale counterparts when the operation performed is limited by mass or heat transfer, i.e. when the reaction rate is comparable to the heat or mass transfer rate [100]. However, it must be noted that the characteristics listed above are also a pre-requisite of the usefulness of microreactors in any particular reactive application, and attributing 'magical' properties to microreactors has resulted in comic relief at the expense of the authors in at least one reported case [101], [102]. Several collateral advantages of microreactors

over their batch counterparts arise from the fundamental physical advantages listed above. These include their small footprints per kilogram product [103], their smaller reagent consumption when used for the purposes of gathering information (high throughput screening) [104], [105], their ability to safely carry out otherwise hazardous reactions [106]–[108], their reduced environmental impact due to their superior heat transfer properties (leading to a lower energy consumption [109]) and their improved selectivity [110], [111]. Finally, as mentioned above, microreactor technology is suitable for continuous processing [112], and the scale-up of microreactors by scaling out (parallelization) is conceptually straightforward [113], and has been pursued to various degrees of industrial success [114].

The following sections will discuss the aspects of microfludics that are relevant to this thesis: droplet microfludics and its use for microparticle production, with a special emphasis on microfluidic crystallization

1.3.1 Droplet Microfluidics

Droplet microfluidics is the sub-field of microfluidics, in which two or more immiscible liquid phases are injected to meet at a microfluidic junction to form droplets (dispersed phase) in a carrier liquid (continuous phase) [115]. Performing various unit operations in droplet microfluidics rather than single-phase microfluidics has several distinct advantages. When one performs a chemical unit operation, the process often requires contact and mixing between different liquid phase reagents. In microfluidic channels, co-dispensing two miscible reagents usually leads to a laminar co-flow scenario, in which the mixing time is controlled by the characteristic diffusion length (and thus, channel dimensions). However, for fast reactions, diffusive mixing might be inadequate and lead to unwanted effects (such as undesired side products). In droplet microfluidics, on the other hand, mixing times can be drastically reduced due to the shear-induced recirculatory motion within the droplets [116]–[119].

The other important property of droplet microfluidics is its capability of monodisperse emulsion generation. The formation of droplets in microscale geometries is governed by the balance between interfacial, viscous, and inertial forces, which are affected by the surface properties and the geometry of the microchannel, the presence of surfactants and the properties of the immiscible phases [120]–[123]. By choosing the right combination of the aforementioned conditions, microfluidic devices are capable of generating monodisperse emulsions of various compositions and morphologies [124], [125]. Besides simple single emulsions, monodisperse multiple emulsions (or compound droplets) of various morphologies [126], [127] can be produced by tuning the interfacial properties of the continuous and dispersed phases [128]–[130]. A study by Lee *et al.* has taken the idea of microfluidic multiple emulsions a step further by showing that the internal structure of double emulsions can be tuned by adjusting the shear rate to achieve non-equilibrium morphologies [131]. Finally co-dispensing a gas phase with the liquid phases, functional composite foams [132] and reversibly attached gas-liquid compound droplets [133] of a remarkable uniformity can be formed.

Studies performed in microfluidic droplets cover an immense range of fundamental, synthetic and analytical areas. Therefore, only two relevant applications will be discussed in the following sections: the production of microparticles in droplet microfluidics and microfluidic crystallization; the interested reader is referred to three great comprehensive reviews for other applications [115], [116], [134].

Droplet Microfluidics for Microparticle Production

In the microfluidic production of microparticles (the size of which is typically of the order of tens to hundreds of microns), monodisperse microfluidic emulsions are generated and used as templates for particle formation. Beside the fact that the morphology of these particles is often inaccessible with conventional

methods, the monodispersity of microfluidic particles generally makes them superior for most applications [135], [136]. The most obvious candidates that can be turned from monodisperse microfluidic droplets into particles are polymers: typically, a monomer is first emulsified in an inert continuous phase, followed by a curing step that preserves the morphology of the droplets, thereby producing monodisperse polymeric microparticles [137]. Initially, however, particle morphologies were restricted to spherical and deformed spherical shapes (i.e. disks, rods, and cylinders) that could be obtained through the geometric confinement of droplets in the microchannels [138], [139]. To circumvent these constraints of droplet microfluidics, two inventive methods, continuous-flow lithography [140] and stop-flow lithography [141] went back to single-phase flow to synthesize polymeric particles of arbitrary shapes specified by a lithographic mask. The high resolution of stop-flow lithography, in particular, made the technique especially suitable for the synthesis of bar-coded microparticles that are advantageous for multiplexed biological assays [142].

Beside homogeneous polymeric microparticles that are either functional *per se* (e.g. for chromatographic use [137], [143]) or bear a functional payload (e.g. polymerized ionic liquid microbeads loaded with pH-responsive dyes [144]), there is a great interest in microstructured particles with well-defined domains. These microstructured particles can both be synthesized in single and multiple emulsions. In single emulsions, the microstructure is typically generated through a phase separation or a self assembly process, such as the synthesis of porous polymeric microbeads in presence of a porogen [145], the partitioning of microgel suspensions [146], [147], or colloidal self assembly through a reactive [148], [149] or evaporative pathway [150], [151]. Double emulsions, on the other hand, are inherently inhomogeneous, and can directly be used as templates for microstructured particles [126]. When the outer layer of a double or multiple emulsion is polymerized or solidified, microcapsules loaded with the innermost phases form [126], [127], [152]. These capsules, in turn, can be engi-

neered to respond to various stimuli, and are therefore very promising vehicles for controlled delivery and release of active ingredients [152], [153]. Finally, polymerizing one segment of a biphasic compound droplet can yield particle morphologies that result from sphere-sphere intersections, such as lenses, hemispheres, and dimpled spheres [154].

One class of microparticles produced in microfluidics, that of crystals, is of special relevance to this thesis, and will therefore be discussed in detail in the next section.

1.3.2 Crystallization in Microfluidics

The precise spatio-temporal control of operating conditions achievable in microfluidics, especially coupled with the compartmentalization of the reagents in droplet microfluidics, makes these platforms very attractive for performing crystallization experiments. Previous research on crystallization in microfluidic systems took two major directions: data acquisition and the production of crystals.

Microfluidic Crystallization for Data Acquisition

In the most widespread application of microfluidic crystallization, populations of microfluidic droplets are treated as individual, nanoliter-sized batch crystallizers with a precise control over operating conditions. These populations of uniform droplets can then be used to gather statistically significant information about various aspects of crystallization [155].

Firstly, as mentioned in the previously, segmenting a solution into small droplets is an ideal way to probe nucleation without disturbances from extraneous impurities. In fact, Vonnegut and Turnbull's aforementioned studies on the subject [86], [87] inspired most nucleation-related research in microfluidics. Since nucleation is inherently a stochastic process, and microfluidic droplets are far from the thermodynamic limit [30], [156], a series of studies in the 1950s

established that in a droplet-based system with sufficiently fast crystal growth (so that only one nucleation event can happen within a droplet) and a constant supersaturation, the probability of *no* nucleation observed within a droplet over time, $P_0(t)$, is governed by the following equation [157], [158]:

$$P_0(t) = \exp(-JVt) \tag{1.2}$$

where J is the nucleation rate, V is the volume of the droplet and t is time elapsed after the attainment of supersaturation. In a statistically significant population of droplets, this probability corresponds to the *fraction* of droplets that have not yet crystallized at a given time point [158]. The populations of droplets used in these studies, however, were far from monodisperse, making the extraction of meaningful data difficult [159]. An 1959 study by White and Frost was the first to overcome these challenges and extract nucleation rates from monodisperse emulsions [160]. These emulsions were generated in an "oil flow dropper", a device conceptually very similar to those used in modern capillary microfluidics [125], [126]. Since White and Frost's pioneering paper, several microfluidic devices and methods have been invented to gather insights about the nucleation kinetics of a large variety of materials: small inorganic [161] and organic molecules [162]–[164], colloidal crystals [165], and proteins [166]–[168]. The theoretical considerations of stochastic nucleation have also been refined by Goh *et al.* to account for droplets with multiple nucleation events and time-varying volume or supersaturation [169] (the specifics of which will be discussed and utilized in Chapter 3). Recently, Chen *et al.* coupled this theoretical advancement with experimental data and a numerical algorithm to identify upper and lower bounds of nucleation rates [29]. This approach can be used to identify the exact dependencies of nucleation rates at higher supersaturations [29].

High throughput screening of crystallization conditions is the other data acquisition method that is greatly improved by droplet microfluidic techniques. The crystallization of proteins, in particular, is a well-known challenge that tra-

ditionally requires a lengthy screening process to obtain a diffraction-quality single crystal [170]. The ability of microfluidic setups to rapidly screen a large piece of operating parameter space with high precision generated several well-executed studies to explore conditions that yield diffraction-quality protein crystals [171]–[174]. Since crystallization processes are often governed by kinetics, an especially interesting extension of screening studies is the exploration of *kinetic pathways*, i.e. trajectories on the phase diagram taken during crystallization to obtain protein crystals of superior quality [175]–[177]. In addition to optimizing protein crystallization conditions, kinetic pathway screening can lead to insights about the formation of different polymorphs in small molecule crystallization, which can then aid the rational design of API crystallization processes [178]–[180].

Production of Crystals in Microfluidics

One could reason that the precise metering of reagents and the exquisite control of operating conditions in microfluidics might enable continuous, scalable *production* of crystalline materials with tailor-made kinetic pathways to obtain the desired crystal form. However, there is a major limitation of performing crystallization in microreactors: the formation of crystalline solids in such confined spaces quickly leads to flow disruption and channel blockage [155]. While solids deposition can be prevented during the synthesis of nanomaterials by confining the reaction to droplets [181], the deposition of micron-sized crystals is almost inevitable. Therefore, it is not surprising that the first report on a robust on-chip crystallization process of pharmaceutically relevant microparticles was only published in 2012, when Sultana and Jensen reported a continuous, seeded microfluidic crystallization platform for API molecules [182]. However, the fact that extensive reactor design, seeds, and surface modifications of the microchannel had to be used in order to overcome the challenges of precipitating crystals in a microchannel highlight the difficulties of such an endeavor [182], [183]. Be-

side this study, pharmaceutically relevant on-chip microfluidic crystallization is confined to nanomaterials produced either in flow [184] or in microfluidic spray driers [185], [186] and the thermal quenching of fats to produce microparticles of various morphologies [187].

A promising alternative to on-chip crystal production is performing the crystallization step off-chip while retaining monodisperse microfluidic droplets as templates. Prior to the studies presented in this thesis, this technique has only been explored in the context of fats [188], [189] and colloidal crystals [151], [190]. The work presented herein fills this gap, and extends this method to API crystallization.

1.4 Thesis Outline and Contributions

This thesis presents the development of a continuous, scalable, microfluidics-enabled emulsion-based crystallization platform for the production of uniform spherical agglomerates of API crystals. Firstly, it is shown in Chapter 2 that monodisperse microfluidic droplet generation in conjunction with off-chip thin film evaporation can produce SAs of a model API compound, glycine with an unprecedented uniformity and drastically reduced crystallization times. In addition to solving problems faced by batch emulsion-based crystallization, decoupling emulsion generation from crystallization also circumvents the typical microfluidic crystallization challenge of clogging. In addition, microscopic observation of the crystallizing droplets revealed the distinct phases of the process that have previously not been reported due to the lack of on-line monitoring opportunities in conventional systems.

Next, in Chapter 3, the effect of operating conditions (temperature, droplet size, rate of srhinkage) on the morphological outcome of thin-film spherical crystallization is investigated and modeled. It is determined that spherulitic crystal growth [191]–[193] is required to obtain complete SAs, which can only be achieved if a critical supersaturation is attained within a droplet before nucleation occurs. This scenario is modeled by using the classical nucleation theory

[22], [23] in conjunction with a theory developed for nucleation in small volumes with time-varying supersaturation [169] to obtain $P_0(t_s)$, the probability of *no* nucleation occurring within a single droplet before attaining critical supersaturation. This calculated probability is compared to f_I , the experimentally observed fraction of complete SAs among the ensemble. The experimentally observed trends are accurately captured by the simulations.

To move on from the semi-batch platform used in Chapters 2 and 3, Chapter 4 presents a proof-of-concept continuous emulsion-based crystallizer based on the belt evaporator. This prototype crystallizer is capable of producing high quality SAs at the rate of ~1-10 g/day, while having a volumetric footprint of only ~10 L. Owing to the straightforward scale-up of this process by scaling out, its throughput makes the setup suitable for the production of small- to medium-volume, high value APIs.

Finally, Chapter 5 explores future prospects of the developed process. First, ongoing research on advanced microfluidic formulation methods for a selected hydrophobic compound (ROY) with an excipient is presented. It is shown that by tuning the rate of evaporation, the morphology of the agglomerates and the polymorphic form of the crystals can be tuned. It can be anticipated that such advanced processes, along with scaled-up continuous microfluidic crystallizers will be the main directions of research and industrial development in the near future. The second part of this chapter focuses on potential issues that have to be overcome in order to bring the process up to speed with potential industrial applications. In the final part of Chapter 5, potential fundamental research directions are addressed. These directions have been opened up by the platform developed in Chapter 2, which enables the investigation of spherical crystallization dynamics in unprecedented detail.

In summary, the main contribution of the work presented herein is the start-to-finish development of a scalable, continuous, microfluidics-enabled crystallization process for the production of uniform and spherical particles of API

crystals. Scientific contributions include the elucidation of the nucleation kinetics and formation mechanism of SAs, the delineation of the operating parameter space under which SAs form and the mathematical modeling thereof. Owing to the increased need for novel processes and equipment for continuous pharmaceutical manufacturing, this work is of direct industrial relevance.

2 Spherical Crystallization of Glycine From Monodisperse Microfluidic Emulsions

2.1 Introduction

As seen in Chapter 1, emulsion-based crystallization to produce spherical crystalline agglomerates (SAs) is an attractive route to control crystal size and shape during the downstream processing of active pharmaceutical ingredients (APIs). It was also discussed that conventional methods of emulsification in stirred vessels pose several problems that limit the utility of emulsion-based crystallization, such as the polydispersity of the resulting particles and the lack of on-line monitoring opportunities.

In this chapter, a capillary microfluidic platform was used to generate monodisperse water-in-oil emulsions, which, in conjunction with evaporative crystallization on a flat heated surface, enables controllable production of uniformly-sized SAs of glycine in the 35-150 μm size range. By performing the crystallization step off-chip, the processing challenges previously associated with microfluidic API crystallization platforms (such as clogging, and device fouling) were completely bypassed. Detailed characterization of particle size, size distribution, structure and polymorphic form is reported. Furthermore, online high-speed stereomicroscopic observations revealed several clearly demarcated stages in the dynamics of glycine crystallization from emulsion droplets. Rapid droplet shrinkage was followed by crystal nucleation within individual droplets. Once a nucleus formed within a droplet, crystal growth was very rapid (complete in 0.1 s) and occurred linearly along radially advancing fronts at speeds of up to 1 mm/s, which suggests a spherulitic crystal growth mechanism. The spherulitic aggregate thus formed ages to yield the final SA morphology. This aging mechanism was determined to be solvent-mediated phase transformation. Overall crystallization times were of the order of minutes, as compared to hours in con-

ventional batch processes.

2.2 Experimental Section

Glycine (>99%), dodecane (>99%), Span-20, Span-80, and Trichloro-(1H,1H,2H,2H-perfluorooctyl)-silane (97%) were purchased from Sigma-Aldrich and used as received. Ultrapure water (18.3 M) obtained using a Millipore MilliQ purification system was used to prepare aqueous glycine solutions. Sterile syringes (3 and 10 cc) and sterile single use needles (21 G 1.5") were purchased from Terumo Corporation, Japan. Syringe filters (0.45 μm) were purchased from Cole-Parmer. Microscope slides (Corning 75x50 mm) were used as a crystallization platform and for sample collection.

A schematic of the experimental setup and procedure is provided in Figure 3. Monodisperse emulsions were produced in a coaxial capillary setup, in which a round capillary (1 mm outer diameter) with a tapered end functions as a collection tube and the two immiscible liquids are infused through a coaxial outer square capillary (1 mm inner side). Two devices were used with different end diameters of the tapered round capillary - 'narrow': 90μm and 'wide': 450 μm - to generate droplets within two broadly different size ranges. Dodecane was used as a continuous phase (CP) with a 2% (w/w) surfactant mixture consisting of 70% Span-20 and 30% Span-80 (w/w) [84]. The dispersed phase (DP) was a glycine solution saturated at room temperature (22 °C); therefore the glycine content was approximately 24.4 g glycine/100 g water. This solution was filtered through a 0.45 μm syringe filter before each experiment. As shown in Figure 3, the glycine solution and dodecane-surfactant mixture were loaded into separate syringes and infused into the capillary emulsion generator using syringe pumps (Harvard PHD 22/2000 series) at various flow rates. The emulsions generated were directly dispensed for 10 seconds onto glass slides placed on a hotplate (Thermo Scientific CIMAREC) set to 90 °C. The surface temperature of the glass slides was measured with a thermometer (Lutron TM-914C) to be 84 °C. Imaging of the droplet breakup and crystallization was performed with

high-speed digital cameras (Basler pI640 or Miro Phantom EX2) mounted onto a stereomicroscope (Leica MZ16). An Olympus LG-PS2 light source with a gooseneck was used for illumination.

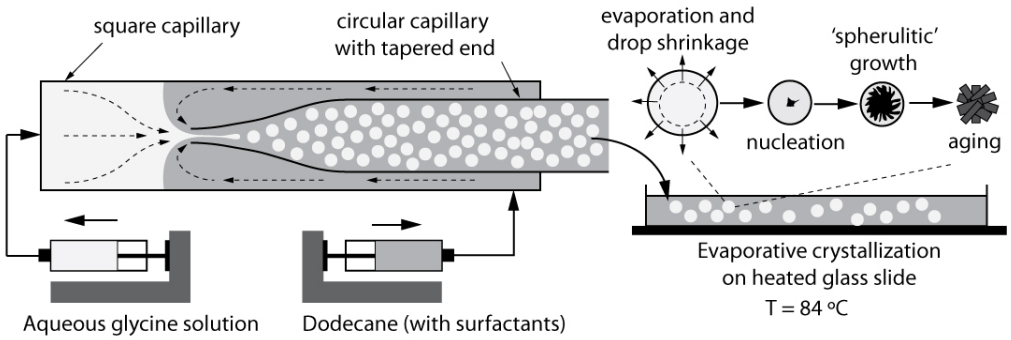

Figure 3: Schematic of experimental setup. Emulsion generation is performed in a concentric microfluidic glass capillary setup, where a square capillary (ID=1 mm) houses a tapered round capillary (OD=1 mm). The two ends of the square capillary function as inlets and the round capillary functions as a collection tube and outlet. The continuous phase (CP) of dodecane (with dissolved surfactants) and a dispersed phase (DP) of aqueous glycine are infused by syringe pumps into the square capillary. The emulsions are collected on a heated glass slide, where evaporative crystallization occurs. A more detailed description of the fabrication and assembly of the devices used is provided in Appendix A.

The SAs obtained were characterized in three different ways: microscopic image analysis for size distribution studies, field emission scanning electron microscopy (FE-SEM) for structural characterization and powder X-ray diffraction (XRD) for polymorphic characterization. For the size distribution studies we used an inverted microscope (Nikon Eclipse Ti) operated in dark field mode. The inbuilt software (NIS Elements 3.22.0) was used to measure the diameter of the agglomerates (circle by three points method) and to estimate the average diameters and standard deviations based on measurements of at least 100 SAs. A field-emission scanning electron microscope (JEOL JSM-6700F) at 5 kV accelerating voltage was used to acquire further structural information on the SAs. All samples were prepared on conventional SEM stubs with carbon tape, and were coated with ~10 nm of platinum by sputter coating. An XRD diffractometer (LabX XRD-6000, Shimadzu) with characteristic Cu radiation was used for polymorphic characterization. The crystal samples were ground

into a fine powder and filled into the cavity of an aluminum sample holder that was mounted to a motorized stage for sample scanning. The X-ray diffractometer was operated at 40kV, 30 mA and at a scanning rate of 2°/min over the range of $2\theta = 10 - 40^{\circ}$, using the Cu radiation wavelength of 1.54 Å.

2.3 Results and Discussion

2.3.1 Emulsion Generation

Two different end taper sizes were used for the circular capillary in the emulsion generator - see Figure 3 - to produce broadly two size ranges of aqueous emulsion droplets that were classified as 'large' ($d_0 = 200 - 320$ μm range) and 'small' ($d_0 = 70 - 120$ μm range). By choosing appropriate combinations of oil and water volumetric flow rates (as indicated in Table 1), droplets with tightly controlled sizes and distributions could be dispensed in the above ranges. Typical standard deviations for the emulsion droplets were $<1\%$ in all cases, highlighting the efficacy of the capillary microfluidic method in generating highly monodisperse water-in-oil emulsions.

Table 1: Summary of the experimental conditions and the properties of droplets and agglomerates obtained. Condition: as seen on Figures 4 and 5; Q_{CP} : flow rate of continuous phase; Q_{DP} : flow rate of dispersed phase; d_0 : droplet diameter (with a standard deviation of less than 1% in all cases); d_A : average agglomerate diameter; σ_{d_A} : standard deviation of agglomerate diameters.

Condition	Device	Q_{CP}	Q_{DP}	d_0	d_A	σ_{d_A}
		μL/min	μL/min	μm	μm	%
a	Narrow	100	20	80	38	9
b	Narrow	100	30	115	48	3
c	Wide	1000	20	210	86	7
d	Wide	1000	40	310	149	6

2.3.2 Crystallization and Agglomerate Characterization

The emulsions generated were dispensed onto a heated glass slide maintained at 84 °C via a short length of tubing, where they formed a thin film of ~0.2-0.5 mm depth. The following sequence of phenomena were observed to occur in each dispensed droplet: (1) rapid (i.e. within ~10 s) shrinkage by ~50% of the dispensed diameter in all cases, (2) onset of nucleation, with nucleation times varying from ~10-300 s, (3) very rapid (<0.1 s) growth of the nucleus along radially advancing fronts that eventually stopped at the droplet boundary and (4) ageing of the crystal-filled droplet to yield spherical agglomerates (SAs). These individual stages are discussed in further detail in the next sections.

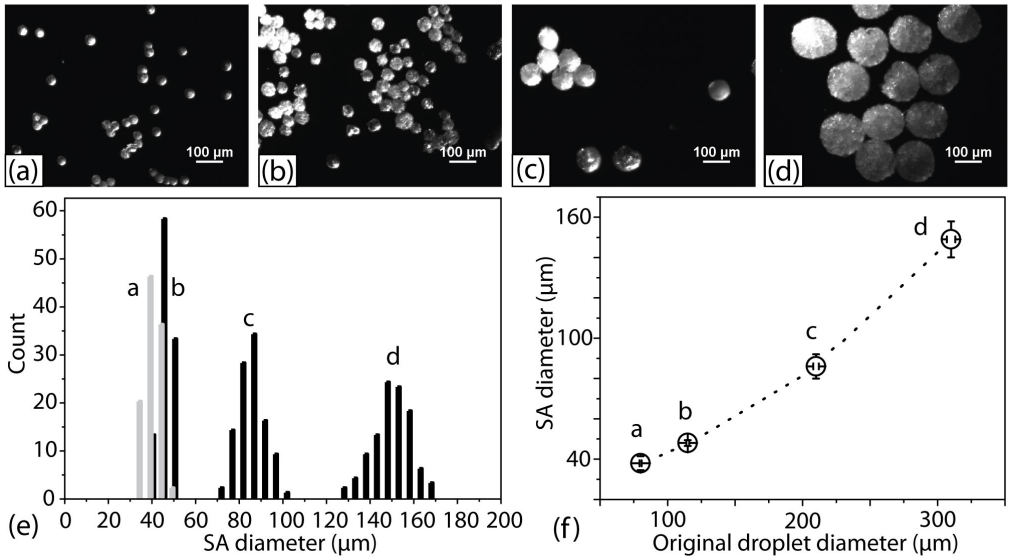

Figure 4: (a)-(d) Dark-field microscopy images of spherical agglomerates obtained under different conditions, (e) SA size distribution histograms for these samples (key parameters are summarized in Table 1) and (f) comparison of the dispensed droplet diameters with the average SA sizes obtained; droplets shrink to ~50% of their original size before crystallization initiates.

A collection of microscopic images (under dark-field illumination) of SAs obtained under different conditions, histograms of particle sizes from the four samples, and a comparison of droplet and SA sizes are provided in Figure 4. The smooth size distribution of SAs obtained by this method is much narrower than that of comparable SAs produced by batch crystallization [84], the most

striking difference being the complete absence of extremely small or large SAs. For all sizes shown here, the diameter of SAs obtained is ~50% of the original droplet diameter. Similar observations regarding droplet and SA diameters were reported by Chadwick *et al.* for the batch case [84]. Sphericity of the agglomerates was confirmed by field-emission scanning electron microscopy (FESEM) observations with a tilted stage (Figure 5). It was observed that the size of the individual crystals that constitute the SAs increases as the size of the SAs increases. Larger SAs (>100 μm) were also more susceptible to breakage and flattening during handling and characterization, suggesting a balance between the structural integrity and the size of the SAs obtained, which has to be controlled by optimizing crystallization parameters (such as droplet size and the rate of supersaturation-generation).

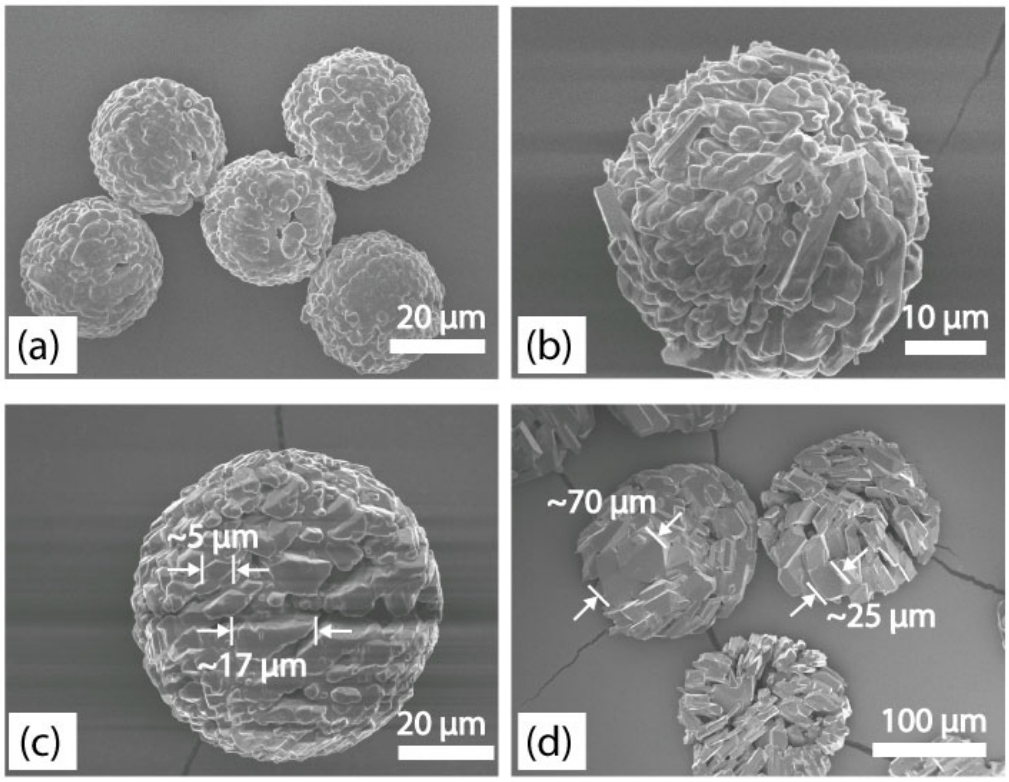

Figure 5: FE-SEM images of SAs obtained under different conditions (Table 1 and Figure 4). Smaller SAs [(a) and (b)] are comprised of compactly packed crystals of small (<10 μm) size while larger SAs [(c) and (d)] consist of larger and, for the latter case, loosely packed crystals.

Finally, XRD results confirmed that the SAs obtained were composed of

predominantly the α polymorphic form under all conditions (a sample XRD pattern is provided in Figure 6; $\alpha-$glycine has characteristic peaks at 2θ values of 15, 19, 24 and 29.8° [194]), the β and γ forms were present only in minute amounts. It should be noted that this is the expected result when crystallizing glycine from an aqueous solution [83].

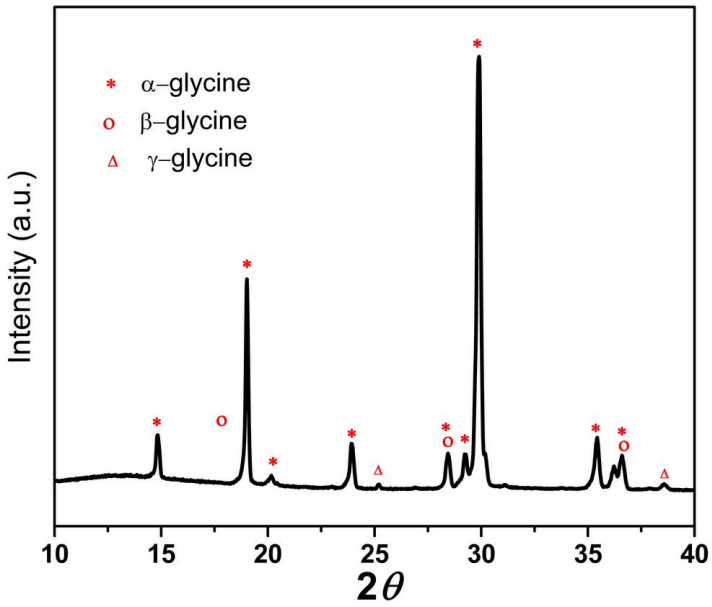

Figure 6: XRD characterization of SAs obtained from condition (d) (Table 1). Characteristic peak positions of all three polymorphs are indicated; the α polymorphic form is the dominant component.

2.3.3 Crystallization Dynamics

Stereomicroscopic observations have shed light on the various stages of crystallization. The dispensed emulsions started crystallizing on the heated slide after a short induction time (~10-40 s) in all cases, with a typical ensemble crystallization time of a few minutes. This overall crystallization time is significantly less than that observed in batch processes (typically on the order of hours [84]). As mentioned briefly in the previous section, the droplets first shrank rapidly as water evaporated through thin films of oil surrounding the droplets on the slide, following which nucleation occurred within the individual droplets. Time-resolved droplet shrinkage and nucleation statistics measurements were

conducted (sample results provided in Figure 7) to uncover the details of crystallization dynamics.

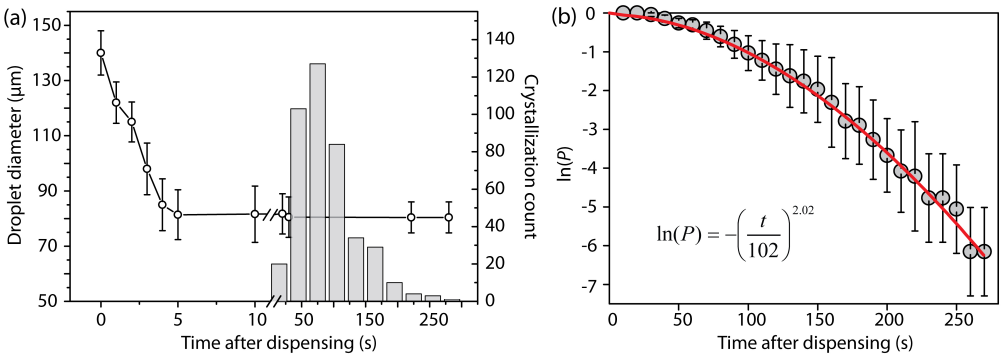

Figure 7: (a) Plot of droplet size versus time indicating shrinkage dynamics, with an overlayed histogram of nucleation statistics (number of droplets with nuclei in a given time interval) for a population of droplets of ~140 μm initial size. Droplets shrink rapidly in <10 s, followed by nucleation events in individual drops. (b) Statistical analysis of nucleation induction time measurements for the same sample: the horizontal axis shows the time after dispensing (t), while the vertical axis corresponds to the natural logarithm of the probability (P_0) of no nucleation in a drop within a time t (as obtained from five different ensembles of drops, with a total of 415 nucleation events observed). A compressed exponential model $P_0 = \exp[-t/\tau]^{\beta}$ was fitted to the data with an R^2 value of 0.99, an average induction time τ of 102 s, and a compressed exponent β of 2.02.

Firstly, it can be seen that droplets underwent rapid initial shrinkage following which the size remained essentially constant; the onset of nucleation and crystallization occurred during this latter phase. Shrinkage was complete within ~5 s while the earliest nucleation event occurred at ~25 s, implying that nucleation events could essentially be decoupled from shrinkage. Next, online nucleation induction time measurements were conducted on ensembles of droplets via direct microscopic observation, with ensemble sizes varying from 50-200; a typical histogram of measured nucleation events is superimposed in Figure 7(a). Figure 7(b) shows a plot of the logarithm of probability of observing no nucleation event in a given drop versus time t , and reveals an interesting feature of nucleation in this system. If nucleation in this system were a simple

homogeneous Poisson process

$$P_0 = \mathrm{e}^{-t/\tau} \tag{2.1}$$

with a constant rate parameter $\lambda = 1/\tau$, the plot in Figure 7(b) would be linear. However, clear deviation from linearity was observed and, remarkably, it was found that a compressed exponential model,

$$P_0 = \mathrm{e}^{(-t/\tau)^{\beta}} \tag{2.2}$$

with time constant τ ~102 s and compressed exponent β ~2, fits the data most satisfactorily. The compressed exponential model reflects a non-homogeneous Poisson process with a time-dependent rate parameter $\lambda(t) \sim t/\tau^2$, which increases with time [195].

These results are interpreted by commenting on the possible mechanisms of nucleation within drops. Heterogeneous nucleation by external impurities such as dust particles can be ruled out, because the likely number of impurities is significantly smaller than the number of droplets in an emulsion-based system [90]. Moreover, it was observed that in the rare cases where a visible impurity was present in a droplet - a fibrous dust particle for example - large, faceted α-glycine crystals were obtained. If each drop is assumed to be isolated from the influence of other drops in the ensemble, then two mechanistic candidates remain for our consideration (i) homogeneous nucleation within the drops and (ii) heterogeneous nucleation at the oil-water interface (aided by surfactants or otherwise), which has been documented in several reports of crystallization in emulsions [83], [84], [196]. While neither mechanism can be ruled out, it should be noted that both can be modeled by homogeneous Poisson processes, albeit with different time constants. However, attempts to fit the data with simple two-exponential models [197] were unsuccessful. On the other hand, the compressed exponential process could accurately describe the process, as stated

above. This model highlights an important fact about this experimental system that the drops on the heated slide are not necessarily isolated from the influence of events in surrounding drops. The increasing rate parameter of the compressed exponential model likewise suggests that the presence of formed SAs increases the likelihood of nucleation in the un-crystallized droplets. As an extreme example of this phenomenon, it was observed that formed SAs can trigger nucleation within droplets in their immediate vicinity (a sample image sequence is provided in Appendix A).

Next, high-speed stereomicroscopic visualization at the single-droplet scale provided insights into the physics of crystal growth. Nucleation typically occurred at a random location within or at the surface of a droplet, and crystal growth occurred rapidly from the nucleus along radially advancing fronts at speeds of $\sim$1 mm/s. Digital image analysis of crystal growth within the droplets was conducted by measuring the radial interface position from the nucleation site r for several directions versus time t . The image analysis package of MATLAB was used to measure the radius of the forming SAs: the images were converted into binary images with a threshold value suitable for the individual agglomerate. The number of black pixels was counted from the origin (set as the nucleation site) in +X, -X, +Y, and -Y directions for each frame. The image was rotated by 10 degrees and the process was repeated until the rotation reached 80 degrees. Digital micrographs captured at high imaging speeds and image analysis results are provided in Figure 8 for selected typical cases. Interestingly, linear crystal growth was observed (i.e., $r \sim t$) in all cases, strongly suggesting a spherulitic growth mechanism observed commonly in impure melts, where crystal growth is faster than diffusive mass transfer [191]–[193]. Simple estimates of glycine concentrations within the droplets support the hypothesis that conditions within the emulsion droplets after shrinkage are conducive to a spherulitic growth mechanism. Assuming a uniform temperature of 84 $^{\circ}$C, droplet shrinkage of $\sim$50% and no glycine leaving the droplets, it can be estimated that su-

persaturation values within the shrunk droplets range between 3.5-6.5 (for the range of drop sizes used in this study), with dissolved glycine concentrations of 18.6-20.0 kmol/m^3 and water concentrations of 0.3 kmol/m^3. These values correspond to glycine concentrations of 1.3-1.5 g/mL, which are very close to the solid density of glycine (~1.6 g/mL). Moreover, drastic decreases in mutual diffusivities have been reported for supersaturated aqueous glycine solutions, with very low ($<<10^{-9}$ m^2/s) values above supersaturations of ~1.5 [198]. Given these facts, it is plausible that the contents within the droplets resemble impure melts, with water acting as the impurity, in which the spherulitic crystal growth mechanism has been well documented [191]. Further, extremely low molecular diffusivities at high supersaturation could also account for the observation of rapid initial shrinkage of droplets followed by a prolonged stagnation of their sizes.

Finally, once formed, most agglomerates go through an aging process which is typically completed within ~3-10 s of crystallization, and leads to a coarser surface, likely due to phase transformation and Ostwald ripening mediated by trapped water within the agglomerate [45]. A typical series of microscope images showing the observable coarsening of an agglomerate is provided in Appendix A. In the next section, experimental evidence is provided to show that the primary mechanism behind the aging process is solvent-mediated phase transformation.

2.4 Aging and Polymorphism

As reported in Figure 6, the final SAs obtained from microfluidic emulsions exclusively consist of α-glycine [199]. However, batch emulsion-based crystallization experiments reported in the literature yielded a significant percentage of β-glycine [83]–[85], with the only apparent differences of droplet size and the overall crystallization time. It was also observed that not only do most agglomerates undergo an 'aging' process of visually discernible coarsening (as opposed to the relatively smooth structure of batch SAs), but larger SAs also consist of

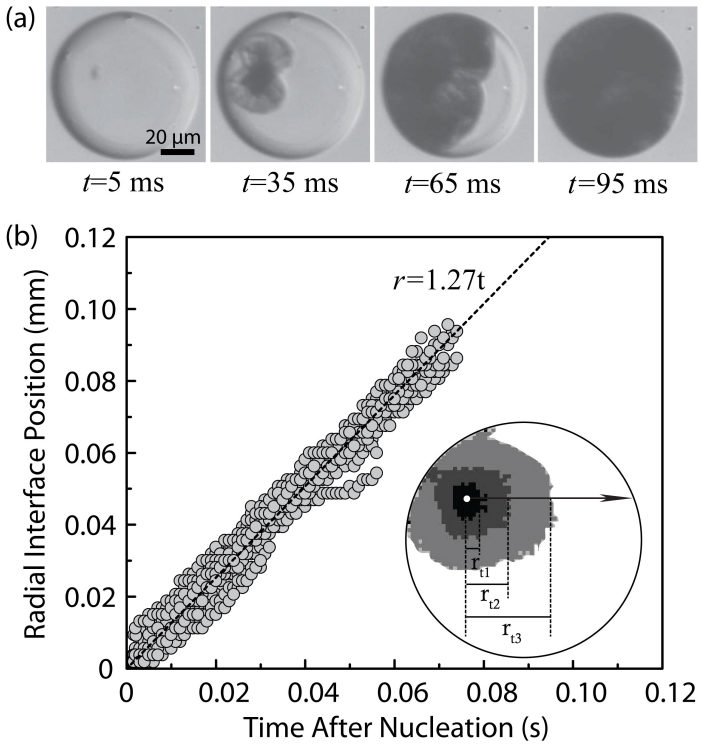

Figure 8: Growth of spherical agglomerates after the nucleation event: (a) high-speed microscopic images of a growing SA obtained at the flow rate combination Q_{CP} =1000 µL/min, Q_{DP} =20 µL/min. (b) the evolution of a 110 µm SA after the nucleation event. It can be seen that radial crystal growth, measured as the position of the interface versus time, assumes a distinctly linear profile (with crystallization speeds of ~1.3 mm/s), a characteristic of spherulitic crystallization. The inset shows an example of how crystal growth is measured via digital image analysis: the radial interface position is tracked along a variety of directions from the point of nucleation; a sample direction is indicated.

larger individual crystals. The 'aging' process can most likely be attributed to a combination of solvent-mediated phase transformation [45] and Ostwald ripening [200] facilitated by the trapped water in the SAs' structure. However, it is very likely that one of these two processes is dominant, and experimental evidence is provided below that 'aging' is primarily caused by solvent-mediated polymorphic transformation in the case of glycine SAs.

To test this hypothesis, Raman microscopy was used on the single SA scale to determine the composition of smooth and coarse agglomerates. Crystallizing droplet populations were dispensed on aluminum foil-coated glass slides, and a Raman Workstation (Kaiser Optical) was used to acquire Raman spectra on the microscopic level. Figure 9a shows a microscopic image of a representative ~60 μm SA population crystallizing at room temperature (22 °C) along with the Raman spectra of α-glycine, β-glycine and two typical 'smooth' and 'coarse' SAs in the 1300-1500 cm^{-1} range. This range was chosen because the other ranges with representative glycine peaks suffered from significant interference from the other compounds present in the emulsion. Specifically, the 1321 (β) to 1324 cm^{-1} (α) shift of the CH_2 wagging peak and the features around 1450 cm^{-1} were found to be the only reliable indicators of polymorphism[36], [201], [202]. Smooth SAs were found to be predominantly made up of β-glycine, while coarse SAs showed the predominance of the α polymorph, thus corroborating the dominant role of solvent-mediated phase transformation.

Further experimental evidence to support this hypothesis was gathered when spherical crystallization experiments were performed in systems that preclude or reduce the rate of polymorphic transformation. Figure 9b and 9c show SEM micrographs of SAs obtained from two such experiments. Figure 9b shows SAs that consist of α and γ-glycine, induced by the addition of sodium dodecyl sulphate to the aqueous phase under conditions that were presented in another paper by our group [203] (and that are nearly identical to the ones presented in Chapter 2), while Figure 9c shows SAs of L-alanine, another simple amino acid obtained

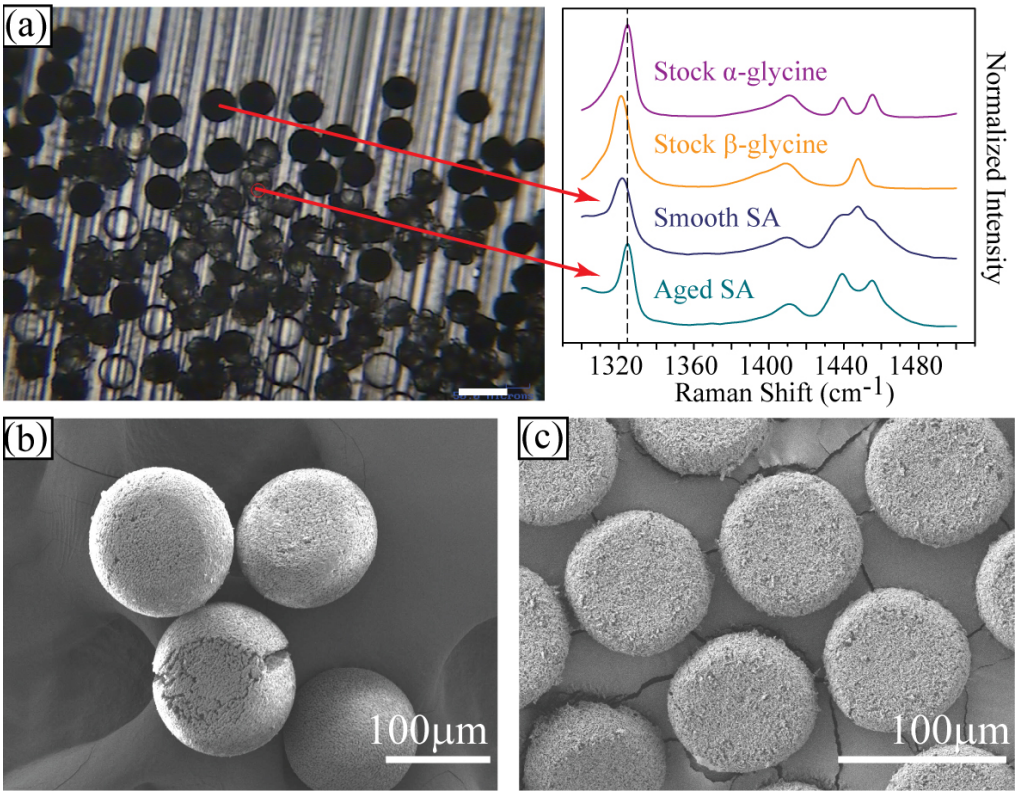

Figure 9: a) a population of crystallizing 60 μm agglomerates under a Raman microscope at 22 °C along with the Raman spectra (in the 1300-1500 cm^{-1} range) of pure glycine polymorphs and two representative SAs in different stages of 'aging'. The 1324 cm^{-1} peak of the α-polymorph is highlighted with a dashed line for clarity. It can be seen that the recently crystallized and still smooth SAs predominantly consist of β-glycine, and 'aged' SAs are predominantly made of α-glycine. This observation suggests that SA 'aging' is a solvent-mediated phase transformation process in the case of glycine. b-c) Spherical agglomerates of b) α and γ-glycine, and c) L-alanine, two systems in which solvent-mediated polymorphic transformation is very slow or nonexistent (respectively). The surface of these agglomerates is extremely smooth, with no observable faceted features.

under identical to the ones described in Chapter 2. L-alanine has only been reported to exhibit polymorphism under high pressure [204] or laser irradiation [205], and therefore could be expected not to undergo a phase transition from a simple evaporative experiment. Owing to the similar experimental conditions, it could also be expected that if Ostwald-ripening played a significant role in the aging phenomenon, these SAs should consist of rather large individual crystals. As can be seen, however, this is not the case: these agglomerates consist of very small domains; note that even crystalline facets are difficult to identify, whereas even the smallest glycine SAs in Figure 5 that have the smoothest texture, are clearly faceted.

In the case of α- and γ-glycine SAs, one could still expect that the transformation of α-glycine to the more stable γ-glycine could lead to the appearance of faceted γ-glycine crystals in the SAs' structure. However, no such crystals were observed, most likely due to the fact that this transformation is very slow [201] because of the relatively small difference between the stability of the two enantiotropic polymorphs [206]. Moreover, the formation of β-glycine in the first place is not unexpected, as it was observed to crystallize from highly supersaturated aqueous glycine solutions in a study by Ferrari et al. [207]. They also pointed out that β-glycine rapidly transforms to α-glycine in pure aqueous solutions, and that this transformation is governed by the dissolution rate of β-glycine crystals [207]. Therefore, it seems that for 'aging' to occur, the presence of a metastable form with respect to another is not enough: the difference between the stabilities (and the dissolution rates) has to be high enough. Alternatively, if one could find a solute that has a very high dissolution rate, Ostwald ripening might emerge as the dominant coarsening process. Finally, it should be noted that the structure of un-aged SAs is very fragile, as indicated by the fact that they regularly deform during SEM sample collection (Figure 9b-c). Hence, a certain degree of 'aging' might, in fact, be required to obtain SAs of reliable quality. These insights provide valuable guidelines for future efforts to produce

SAs of controlled quality, especially for compounds that exhibit polymorphism.

2.5 Concluding Remarks

In summary, spherical crystallization of glycine was demonstrated in monodisperse emulsions generated using a simple capillary-based microfluidic device and a heated thin-film evaporation platform. Spherical glycine crystal agglomerates were produced with a remarkable level of control over shape, size and size-distribution in an industrially relevant size range. By decoupling emulsion generation from crystallization, the well-known disadvantages of microfluidic crystallization platforms, such as clogging and fouling, have been completely bypassed. This study has also shed light on various operative phenomena during emulsion-based crystallization. It was shown that the formation of SAs occurs through the following four steps: (1) shrinkage of the droplets to a limiting size, (2) stochastic nucleation within the droplets that follows a compressed exponential model, (3) spherulitic crystal growth within the shrunken droplets, (4) aging of the spherulitic aggregate through solvent-mediated phase transformation.

This study also raised several interesting fundamental and practical questions and challenges while establishing the technological base for the remaining chapters of this thesis. Keeping in mind that the main goal of this thesis is to build a general, continuous, and scalable crystallization platform, there are three main issues that have to be resolved. Firstly, from a processing standpoint, the understanding of these previously unreported crystallization phenomena within emulsion droplets is crucial in identifying the conditions under which spherical agglomerates of a desired quality can be produced. In pursuit of this understanding, the processing parameter space is explored and the process is modeled in Chapter 3. Next, the scalability of emulsion generation, especially in the context of low-volume high-value pharmaceuticals, can be achieved by parallelization of the microfluidic emulsion generators. However, the platform presented in this chapter couples continuous droplet generation with batch evaporation. Therefore, it is semi-batch in nature. In order to achieve a fully continuous crystal-

lization process, a continuous downstream unit is required. This unit, a novel continuous thin-film evaporator, is presented in Chapter 4. Finally, the applicability of the method is explored in the context of advanced formulations in Chapter 5.

3 Dynamics and Morphological Outcomes in Thin-film Spherical Crystallization

3.1 Introduction

As reported in the previous chapter, agglomerates undergo spherulitic crystal growth after nucleation. This mechanism is particularly interesting because of its generality: besides its ubiquity in crystallization from metallic and polymeric melts [191], it has also been observed during the precipitation of small organic and inorganic molecules in reactive [208], evaporative [84] and antisolvent crystallization [79], [164]. Spherulitic crystallization typically occurs under highly non-equilibrium (i.e. supersaturated) conditions when crystal growth is faster than the reorientation of molecules at the growth front, which can result in polycrystalline aggregates of a variety of morphologies with a spherical shape at larger length scales [193]. The fine details of the actual spherulitic growth pattern and the final morphology of these aggregates is highly dependent on the operating parameters (such as supersaturation and temperature); it is generally accepted that a higher supersaturation leads to more compact spherulites due to the larger degree of branching [193]. These differences in the final morphology of the agglomerates will affect the downstream processing properties of the resulting powder. For example, loosely packed or fragile spherulitic aggregates have been reported to shed their individual crystallites and cause filtration problems in at least one case [209]. A number of studies have focused on these effects in conventional batch crystallization systems, reaching conclusions that are in line with the theoretical framework of spherulitic growth [208], [210], [211]. As mentioned above, however, the inherent spatio-temporal inhomogeneity of operating conditions in a batch crystallizer and the inherent difficulty in relating these to measurements of particle properties, typically made *post factum*, sets limits to the experimental understanding of spherical crystallization.

In Chapter 2 it was shown that thin-film evaporative crystallization from microfluidic emulsions not only facilitates the production of uniform spherical agglomerates (SAs), but also enables the on-line observation of the process. It can be anticipated, however, that by changing processing parameters, such as droplet size, film thickness and substrate temperature, the formation process, and hence the morphology of the obtained SAs could be influenced. Moreover, from a processing standpoint, it would be crucial to identify regions of the multi-dimensional processing parameter space that yield SAs of a desired morphology. This study exploits the advantages of monodisperse microfluidic droplet populations and the ability to monitor the crystallization process in individual droplets to gain further understanding of glycine SA formation in this system. Specifically, the influence of droplet size, shrinkage rate and temperature on the crystallization process was investigated. Experimental results indicate that lower temperatures, smaller droplet sizes, and faster shrinkage generally favor the formation of complete, spherical, compactly packed SAs (termed 'Morphology I', the generally desired morphology), while the converse leads to the formation of incomplete SAs or single crystals ('Morphology II' see Figure 13 for a visual description of the process). Further, it was shown that these measured parameters influence the progression of two important inferred parameters over time - supersaturation and the rate of nucleation. It was hypothesized that undesired morphologies are obtained when nucleation events occur in the droplets before they have reached the high supersaturation required for spherulitic growth. A mathematical model was formulated to test this hypothesis; using the classical theory of nucleation [22], [23] and by modeling nucleation within microfluidic droplets with time-varying supersaturation as a non-stationary Poisson process [169], a self-contained model was obtained. This model captures the competition between supersaturation and nucleation throughout the process. The results obtained from these simulations are in good agreement with overall experimental observations.

3.2 Experimental Section

Monodisperse microfluidic emulsions were generated with the same materials and methods as in Chapter 2. Flat bottom glass Petri dishes (ID = 26mm) made of borosilicate were manufactured by HCS Scientific & Chemical Pte Ltd, then silanized using 1H,1H,2H,2H-Perfluorooctyltriethoxysilane (98%) purchased from Sigma-Aldrich. After silanization, the Petri dishes were used as a crystallization platform and for sample collection. The dispersed phase (DP) was a glycine solution saturated at room temperature (24$\pm$1 °C); therefore the glycine content was approximately 25.4$\pm$0.5 g glycine/100 g water [83]. One drop of the generated emulsion was dispensed directly into the glass Petri dish which had a pre-dispensed layer of the continuous phase (CP) (0.5-1.5 mm nominal thickness), placed on a hotplate (Thermo Scientific CIMAREC) set between 45 and 85 °C. The temperature of the CP in the Petri dish was measured with a thermometer (Lutron TM-914C with a thermocouple) and is listed in Table 6 of Appendix B. Imaging of the process (always carried out at the center of the Petri dish to eliminate any potential meniscus effects) was performed with a high-speed digital camera (Basler pI640) mounted onto a stereomicroscope (Leica MZ16). An Olympus LG-PS2 light source with a ring light was used for illumination. A silicon wafer was placed under the glass Petri dish for improved contrast. A schematic of the experimental setup is provided in Figure 10. Nine experiments a 3x3 matrix of initial droplet diameters (d_0) and film thicknesses (h_f) - were performed at a heating temperature of 65 °C in order to investigate the effect of droplet size and shrinkage rate (controlled by film thickness) on the outcome of spherical crystallization in the droplet populations, and four additional experiments were performed to shed light on the effect of temperature, at 45, 55, 75, and 85 °C. Each experiment was repeated at least three times, and each trial typically included at least 100 droplets. All experiments were imaged at 1 frame per second time resolution. Microscopic image analysis was performed for droplet and SA size distribution, nucleation, and morphol-

ogy statistics. Structural information of the SAs was acquired by FE-SEM, as described in Chapter 2.

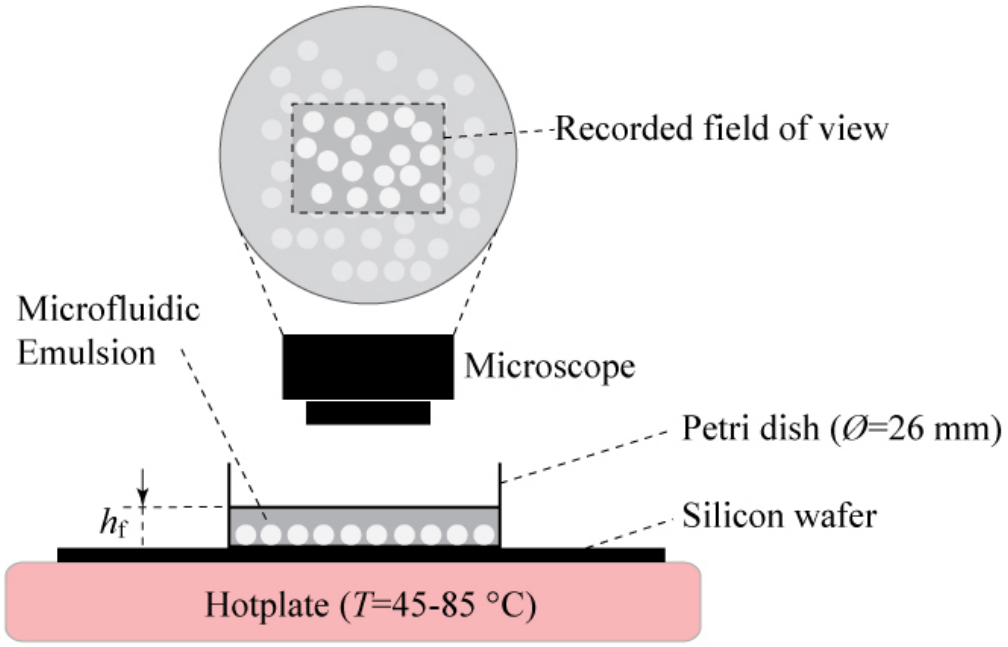

Figure 10: Schematic of the experimental setup used to monitor the crystallization of droplet populations.

3.3 Results and Discussion

The experimental conditions and the main outcome - the fraction of Morphology I SAs among the crystallized droplet population - are summarized in Table 2, while the effects of shrinkage rate and droplet size on the outcome of the process at a heating temperature of 65 °C are given in Figure 11. Briefly, at a fixed temperature, faster shrinkage rates (obtained in thinner films) and smaller initial droplet sizes favored the formation of a higher fraction of Morphology I SAs. On the other hand, this fraction exhibited an apparent maximum (at an intermediate temperature), on increasing temperature at fixed droplet size and film thickness.

In order to understand these observations, the progression of the crystallization process in the dispensed droplets was examined. Precise measurements of droplet size were conducted from dispensing until the onset of crystallization for at least 15 droplets per trial to determine how droplets shrank as water

Table 2: Summary of the experimental conditions used, along with shrinkage times, shrinkage rates and the percentage of Morphology I SAs. #: experiment label; d_0 : initial droplet diameter; d_A : SA diameter; T : heating temperature; h_f : film thickness; t_s : shrinkage time; d' : shrinkage rate (see text for further elaboration on shrinkage); f_I : observed fraction of Morphology I SAs among the crystallized ensemble.

#	d_0	d_A	T	h_f	t_s	d'	f_I
	μm	μm	°C	mm	s	nm/s	
1	53±3	39±2	65	0.5	62±2	220	0.99±0.00
2	53±3	39±2	65	1	1060±323	13	0.92±0.07
3	53±3	39±2	65	1.5	1637±459	8.6	0.61±0.24
4	85±10	62±7	65	0.5	88±9	260	0.96±0.01
5	85±10	62±7	65	1	2369±578	9.8	0.67±0.10
6	85±10	62±7	65	1.5	4074±1492	5.6	0.47±0.15
7	165±5	118±5	65	0.5	84±10	560	0.90±0.04
8	165±5	118±5	65	1	3130±1190	15	0.66±0.07
9	165±5	118±5	65	1.5	6055±2269	7.8	0.41±0.08
10	85±10	62±7	45	1	13500±900	1.7	0.48±0.05
11	85±10	62±7	55	1	7728±1883	3.0	0.64±0.07
12	85±10	62±7	75	1	2542±964	9.0	0.32±0.09
13	85±10	62±7	85	1	1500±180	15.0	0.28±0.06

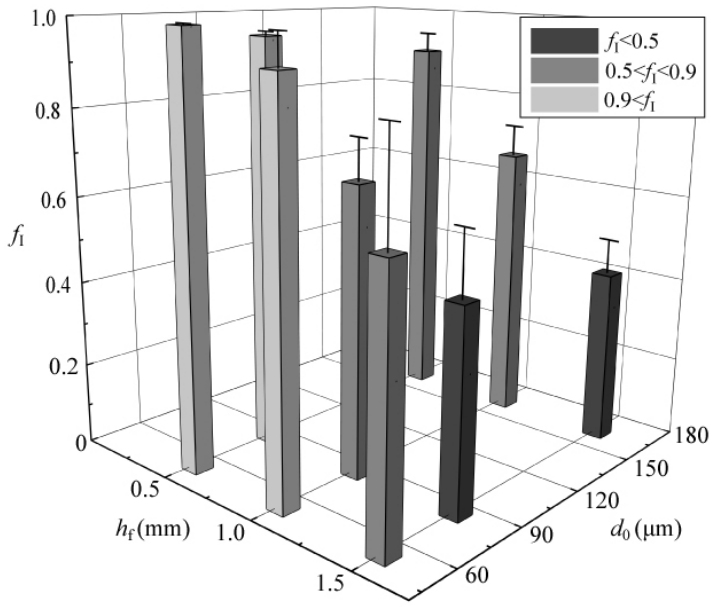

Figure 11: The fraction of Morphology I SAs obtained at T=65 °C under different conditions. The thicker the film (which leads to a lower shrinkage rate), and the larger the initial drop diameter, the lower the fraction of Morphology I (i.e. complete) SAs.

evaporated (a visual example is provided in Figure 12). It was found that in all cases, droplet diameter (d) decreased linearly with time (Figure 12b), as $d(t) = d_0 - d't$ where d' is the (measured) shrinkage rate, and d_0 is the dispensed (initial) diameter of the droplet. At a fixed temperature, shrinkage rate depends on the thickness of the continuous phase film containing the droplets, and is determined by the convective and diffusive transport of water through this film and into the ambient environment. While nominally constant ambient conditions - room temperature (~24 °C) and relative humidity (~57 %) - were maintained throughout our experiments, complete elimination of environmental fluctuations, such as those due to ambient air circulation, was not feasible. Therefore, to circumvent this challenge whilst retaining analytical rigor, *measured* shrinkage rates are used in the discussions below, with the understanding that these relate in a straightforward, quantifiable way to film thicknesses under highly controlled processing conditions typical in pharmaceutical manufacturing. An example of this relationship for our experiments is provided in Appendix B.

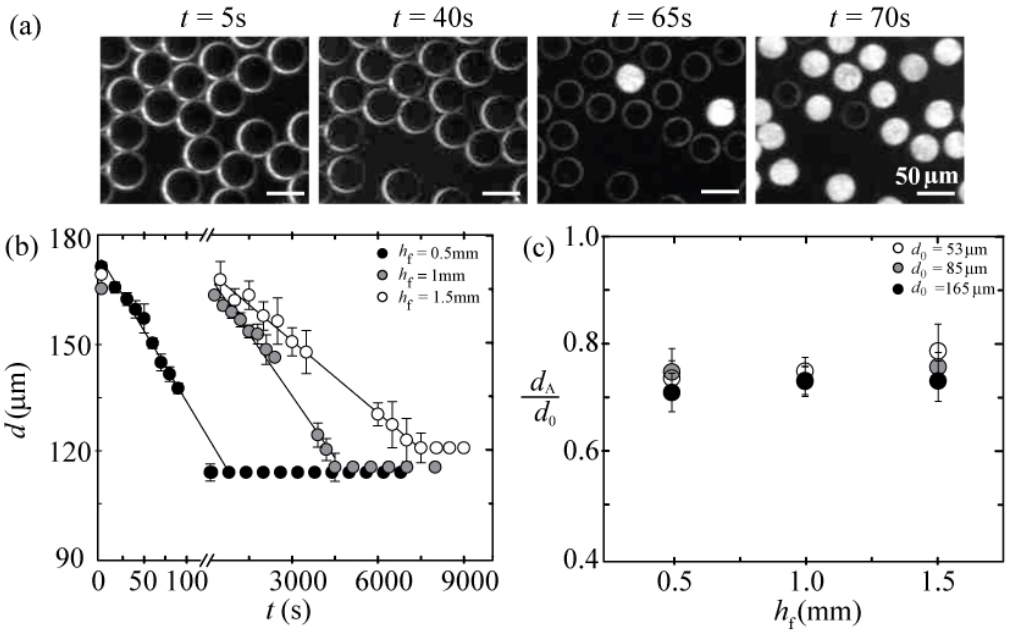

Figure 12: a) An image sequence of the droplet shrinkage process with a film thickness of 0.5 mm and T =65 °C. b) Droplet size measurements over time under different film thickness conditions. c) Final droplet diameter (SA diameter) as affected by the film height and initial droplet diameter for the 13 experiments. Droplets shrink by roughly the same extent under all conditions: d_A =0.73d_0 .

Next, the diameter of the Morphology I SAs was compared to the dispensed diameter of the corresponding droplets from which they were formed. Interestingly, as shown in Figure 12c, it was found that under all conditions, droplets shrank to roughly the same extent. In all cases, final SA diameter was ~73 % of the dispensed droplet diameter, implying, under the assumption that no glycine leaves the shrinking droplets, that there is a limiting concentration (and therefore, a 'critical' supersaturation S_c) beyond which shrinkage practically stops. This phenomenon of a limiting supersaturation has also been reported in previous studies [84], [199] and can be attributed to the dramatic drop of diffusivity in glycine solutions upon reaching this particular supersaturation level [198]. Moreover, it was also observed that single crystals or incomplete SAs (i.e. Morphology II) tended to crystallize when nucleation occurred in droplets before they reached this critical size. These observations imply that the attainment of the critical supersaturation (S_c) corresponding to this critical size is necessary for spherulitic growth to occur, which, in turn, can lead to the formation of com-

plete SAs. Previous studies also cite high supersaturation and severely limited diffusion as being essential to the growth of spherulites. A comprehensive recent theoretical and computational study by Gránásy *et al.* proposed that at high concentrations, the rotational and translational diffusivities of a solution are decoupled, and their ratio ($\chi = D_{rot}/D_{tr}$) decreases sharply as supersaturation is increased, which results in an enhancement of misoriented grain growth, leading to a spherical shape at larger length scales [193]. This transition between single crystalline and spherulitic growth of an increasing degree of branching (i.e. an increasingly spherical shape) with an increasing supersaturation was also observed in experimental studies [209]–[211]. As mentioned above, only SAs that grew into complete, compact spheres were classified as 'spherulitic' (Morphology I) and all other morphologies were classified as Morphology II.

Putting these pieces of evidence together, it can be hypothesized that droplet size and shrinkage rate take part in an interplay of two related phenomena; firstly, as droplets shrink and the concentration of glycine in a droplet increases, supersaturation is achieved and increases over time, and secondly, for supersaturation $S > 1$, nucleation occurs in each droplet at a finite, non-zero rate J . Therefore, as a droplet shrinks, there is a finite (and increasing) probability for a nucleation event to occur in that droplet before it reaches the supersaturation S_c required for spherulitic crystal growth. Thus, according to this line of reasoning, when a droplet reaches this critical supersaturation before the occurrence of a nucleation event, a Morphology I SA is obtained. On the other hand, if a nucleation event occurs before the critical supersaturation is reached within a droplet, a Morphology II SA will be obtained, the exact morphology depending on the conditions within the droplet. Figure 13a shows a schematic of this picture of crystallization in this microfluidic emulsion-based system, while 13b-d display SEM images of the different possible particle morphologies. The effect of droplet size and shrinkage rate can now be explained with the arguments presented above by noting that smaller shrinkage rates (for example by using

thicker oil films) lead to correspondingly slower rates of supersaturation generation, while larger droplet volumes are associated with a higher probability of a nucleation event at a given supersaturation level.

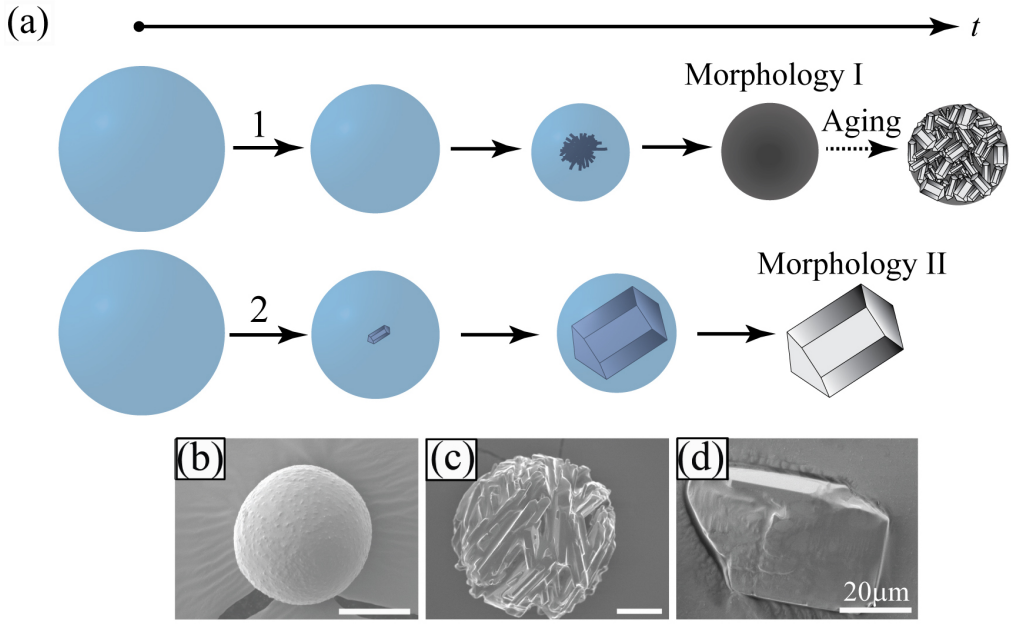

Figure 13: a) Schematic of the SA formation process. There are two possible outcomes: 1) Droplet reaches critical supersaturation before nucleation. This leads to the formation of Mophology I SAs. Once formed, the SA might go through an 'aging' process, in which its surface transitions from a smooth to a coarse structure, as seen in the previous chapter. 2) A nucleus forms within the droplet before it reaches critical supersaturation, which leads to crystals of Morphology II. b-d) SEM micrographs of different agglomerate morphologies obtained from our experiments: b-c) 'smooth' and 'coarse' complete SAs; d) single crystal.

Next, to model this process quantitatively, the following question has to be asked: what is the probability of nucleation within a single droplet before it reaches S_c, the critical supersaturation required for spherulitic growth? If, at the time required for droplets to reach critical supersaturation (t_s), the probability of a nucleation event within a droplet is low (or conversely the probability of no nucleation is high), a majority of Morphology I SAs can be expected to form from the droplet population. In other words, if the above hypothesis describes the process adequately, it can be expected that the probability of no nucleation (P_0) in a droplet at t_s to corresponds, albeit roughly, to the fraction of Morphology I SAs in a droplet population. A model to describe the stochastic nucleation

within small droplets with a time-varying supersaturation was formulated by Goh et al. [169] In this model, the evolution of $P_n(t)$, the probability of n nucleation events in a droplet, with time follows the following differential equations:

$$\frac{dP_0}{dt} = -\kappa(t)P_0(t) \qquad P_0(0) = 1 \tag{3.1}$$

$$\frac{dP_n}{dt} = -\kappa(t)[P_{n-1}(t) - P_n(t)] \qquad P_n(0) = 0 \qquad n = 1,2... \tag{3.2}$$

where $\kappa(t)$ is the nucleation rate in a single droplet, i. e.

$$\kappa(t) = JV(t) \tag{3.3}$$

Here, J is the nucleation rate (a function of $S(t)$, the time-varying supersaturation) and V is the volume of the droplet as a function of time. In this system, Morphology I SAs grow rapidly in ~0.1 s [199], and Morphology II crystals typically finish growing within a second; these growth times are far shorter than typical shrinkage times of >100 s. Therefore, it can be assumed that only one nucleation event occurs within a droplet - an assumption borne out in the experiments. This, in turn, implies that $P_0(t)$ adequately describes the process. By solving the differential equation for $P_0(t)$, the following expression is obtained [169]:

$$P_0(t) = \exp\left[-\int_0^t \kappa(t)\,dt\right] = \exp\left[-\int_0^t JV(t)\,dt\right] \tag{3.4}$$

In order to compute $P_0(t_s)$, $t = 0$ in the above integral is taken as the time at which the shrinking droplet reaches $S = 1$, and t_s is set to be equal to the time when the droplet stops shrinking. This equality assumes that S_c is very close to the final supersaturation attained by the droplets, which can be justified by noting that as mentioned above - the reduction in diffusivity arresting shrinkage [198] also facilitates spherulitic growth [193]. In this model, the measured

droplet sizes are used in the following expression for shrinkage time t_s :

$$t_s = \frac{(1-0.73)d_0}{d'} \tag{3.5}$$

where $0.73d_0$ is the average final size of the droplets (see discussion above).To evaluate the integral in the exponent, classical nucleation theory was applied to glycine to calculate the rate of nucleation as a function of supersaturation [22], [23], [162]:

$$J = AS\exp\left(-\frac{B}{\ln^2 S}\right) \tag{3.6}$$

where A is a pre-exponential factor, described as the diffusion-limited rate of nucleation (in this study A is a fitted parameter, see discussion below), S is the supersaturation expressed as the ratio of the glycine activity relative to its value at saturation (a/a_S), and B is given by:

$$B = \frac{16\pi v^2\sigma^3}{3(kT)^3} \tag{3.7}$$

where v is the molecular volume (assumed to be spherical for glycine with a diameter of 0.53 nm [162]), σ is the interfacial tension between the nucleus and the solution, k is the Boltzmann constant, and T is the absolute temperature. The interfacial tension, σ , can be obtained from the following expression [162], [212]:

$$\frac{\sigma d_m^2}{kT} = \frac{1}{\pi}\ln\frac{n_{Cr}}{a_S} \tag{3.8}$$

where d_m is the aforementioned molecular diameter, n_{Cr} =1575.3 g/L is the solid density of glycine [213], and a_S is expressed in units of g/L. The activity coefficients of glycine at various temperatures were obtained from AspenPlus VLE simulations via the built-in UNIFAC model. Simulated activity data at 25 $^{\circ}$C were validated with those reported by Na et al [214]. The calculated values of B and σ under the temperatures used in this study, and the polynomial fit used in the calculations are presented in Table 6 and Figure 38 of Appendix B

respectively. The solubility of glycine in water [83] and the density of aqueous glycine solutions [215] were obtained from existing literature. By measuring the initial droplet size d_0 , and the linear shrinkage rate d' , $V(t)$ was calculated as

$$V(t) = \frac{\pi}{6}[d(t)]^3 \tag{3.9}$$

where $d(t) = d_0 - d't$. Knowing the initial concentration of glycine in the droplets, $V(t)$, and the simulated relationship between concentration and activity, $S(t)$, and hence, $J(t)$ and $P_0(t)$ can be obtained. Ultimately, in order to obtain $P_0(t)$ at a given temperature from this model, only two measured parameters, d_0 (initial droplet diameter) and d' (linear droplet shrinkage rate) need to be specified. $P_0(t)$ was evaluated until t_s for all experimental conditions.

The simulation results and the corresponding observed Morphology I fractions for $T = 65\,^{\circ}\mathrm{C}$ are compared in Table 3. The value of the pre-exponential factor $A = 2 \times 10^{12}\ \mathrm{m^{-3}s^{-1}}$ at $T = 65\,^{\circ}\mathrm{C}$ was obtained by nonlinear least square regression performed in MATLAB on the results of all 9 experiments at this temperature. The calculated trends from the model are generally in a good agreement with experimental trends. Figure 14 shows three simulated $P_0(t)$ and $S(t)$ curves from three selected experimental conditions along with images from experimental runs. In the case shown in Figure 14a (and corresponding image in Figure 14d), d' is high, and d_0 is small (experiment 1, Table 2). Here, $P_0(t_s)$ is very close to 1, which indicates that there is a low probability for a nucleation event to occur before droplets reach critical supersaturation, leading to the majority of Morphology I SAs in this case. This is in good agreement with the experimental observations, where ~99% of the droplet population consists of Morphology I SAs. Figure 14b and 14e shows a case where d' is low and d_0 is large (experiment 9, Table 2). The calculated $P_0(t_s)$ value of 0.33 indicates that Morphology I SAs will be a minority in this sample, which is consistent with the experimental result of f_I ~0.4. In the simulation shown in Figure 14c, droplet size is increased drastically (to ~600 μm); thus P_0 drops to nearly zero well be-

fore t_s , which indicates that all droplets will likely nucleate before they reach S_c and yield non-spherulitic, faceted crystals. This prediction is well borne out in the corresponding experiment, shown in Figure 14f. Further validation comes from the fact that the smaller satellite droplets co-generated with their larger counterparts, in fact, yield the few Morphology I SAs that can be observed on Figure 14f.

Table 3: Comparison of the simulated P_0 (t_s) values (i.e. the probability of no nucleation occurring within a droplet before it shrank to its limiting diameter) to the fraction of Morphology I SAs at T=65 °C. The model accurately captures the overall trends.

#	d_0	d_A	d'	$P_0(t_s)$	f_I
	μm	μm	nm/s		
1	53±3	39±2	220	1	0.99±0.00
2	53±3	39±2	13	0.99	0.92±0.07
3	53±3	39±2	8.6	0.99	0.61±0.24
4	85±10	62±7	260	1	0.96±0.01
5	85±10	62±7	9.8	0.93	0.67±0.10
6	85±10	62±7	5.6	0.89	0.47±0.15
7	165±5	118±5	560	0.99	0.90±0.04
8	165±5	118±5	15	0.56	0.66±0.07
9	165±5	118±5	7.8	0.33	0.41±0.08

These case studies show that our model describes the overall trends rather accurately. There are, however, more subtle implications of the model that can translate into a further understanding of this process. In the model, as mentioned above, there are two parameters that determine $P_0(t_s)$ at a given temperature d' and d_0 . Firstly, the effect of d' is examined, where intuitively one can reason that since no nucleation events in a droplet are required before reaching S_c , the larger the d' , the better. However, increasing shrinkage rates also imply decreasing shrinkage times, thus implying steeper rates of supersaturation,

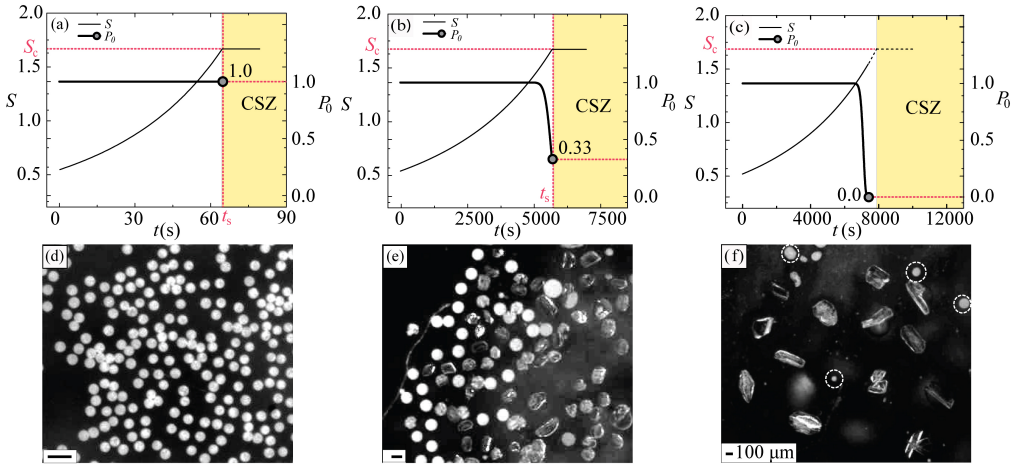

Figure 14: The competition between time varying supersaturation $S(t)$ and $P_0(t)$, the probability of no nuclei forming within a droplet over time, for three selected conditions. Data for $P_0(t)$ were obtained from the simulations described in the text, while $S(t)$ data were based on experimental measurements. If S reaches the critical supersaturation required for spherulitic growth, S_c , before the onset of nucleation, a certain fraction of Morphology I SAs form within the ensemble. This fraction corresponds to the value of P_0 at the time point when S reaches S_c . a) and d) d_0 =53 μm, h_f =0.5 mm and T =65 °C; b) and e) d_0 =165 μm, h_f =1.5 mm and T =65 °C; c) and f) d_0 =600 μm, h_f =1 mm and T =65 °C. The model accurately describes experimental trends. CSZ: critical supersaturation zone.

and concomitantly larger nucleation rates at comparable times. The variation of $P_0(t_s)$ as a function of d' at a fixed initial droplet size is therefore worth examining further, and model simulation results are shown in Figure 15a. These results do in fact point to a nonlinear increase in $P_0(t_s)$ with d' , with a region of sharp increase followed by a plateau. The simulations therefore recommend operation at the cross-over point between the two regimes, beyond which there are diminishing returns on increased shrinkage rates, especially for the smaller droplet sizes. Next, the effect of droplet size, d_0 , is examined via a similar analysis. At fixed shrinkage rate, the larger the droplet, the larger t_s and V , but again, J will be comparably smaller at each time point since S increases comparably slowly. Results shown in Figure 15b demonstrate that the larger the droplet size, the smaller $P_0(t_s)$, and the lower the expected fraction of Morphology I agglomerates from a corresponding experiment. Collectively, the above considerations imply that at a given shrinkage rate, there might exist a critical droplet diameter,

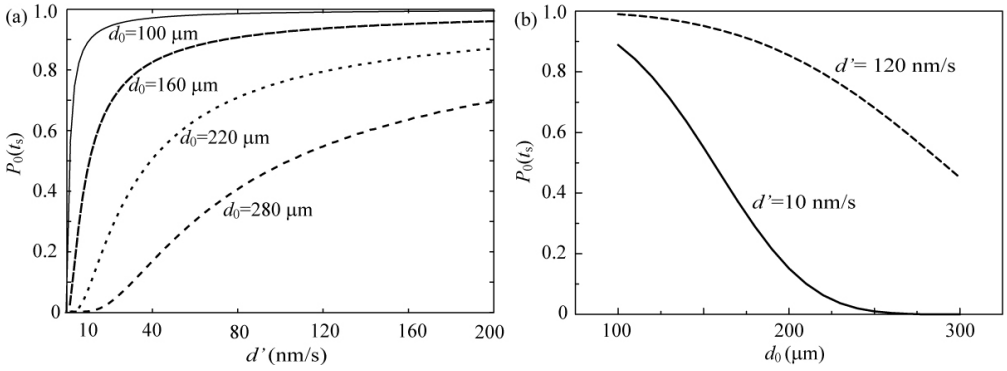

Figure 15: a) The simulated effects of initial droplet size d_0 and linear shrinkage rate d' on $P_0(t_s)$, the probability of no nucleation before shrinkage is complete; b) The effect of droplet diameter at a constant shrinkage rate, all at T =65 °C. It can be seen that at any given d_0 , the largest shrinkage rate gives the highest $P_0(t_s)$ value (i.e. the highest expected fraction of Morphology I SAs in the ensemble). Similarly, at any given shrinkage rate, as initial droplet size increases, $P_0(t_s)$ decreases, eventually reaching ~0 beyond a certain critical diameter d_c (e.g. in the case of d' =10 nm/s, the 280 μm droplets are above d_c).

d_c , above which no Morphology I SAs can be obtained from the system. To calculate this value, $P_0(t_s)$ can be simply set to ~0 (e.g. 0.001) and for a chosen d' , d_c can be obtained from the model. In fact, the choice of d_0 for Figure 14f was based on these simulations, and led to an SA population that consisted almost exclusively of Morphology II crystals. In principle, the same treatment for a decreasing d' could be used to obtain a critical value for shrinkage rate d' , but reducing the rate of evaporation is generally unfavorable from a productivity perspective. On the other hand, while increasing d' is favorable for the production of Morphology I SAs, the experimental apparatus used will necessarily set upper limits on d' . Therefore, one could imagine a scenario in which a solute has a high enough nucleation rate before S_c is reached to completely preclude spherulitic growth at droplet sizes achievable by microfluidic devices. Finally, it is also noted that the generality of this model means that it can describe the crystallization behavior of solutes in which, for example, the functional form of $J(S)$ is different from that used in Equation 3.6 above.

The experimentally observed effect of temperature at a given film thickness and initial droplet diameter is a more complex issue. The experimental results

in Table 2 (experiments 10-13) suggest an optimal intermediate temperature at which the highest fraction of Morphology I SAs is produced under otherwise identical conditions. In order to explain this trend, the behavior of the two parameters in the nucleation rate expression must be examined: while B can be calculated in straightforward fashion as outlined above, A is a rather sensitive parameter that is a complicated function of temperature and molecular properties [23]. In this study, A was fitted to the results of all experiments at h_f =1 mm and d_0 =85 μm (see Figure 39 of Appendix B). Knowing $A(T)$ now enables the prediction of $P_0(t_s)$ at any given point in the (d_0 , d') parameter space at a given temperature. Figure 16 shows illustrative simulated surfaces of $P_0(t_s)$ as a function of d_0 and d' at three representative temperatures within the range studied. It is instructive to observe that at each temperature, there exists a region on this map where $P_0(t_s)$ ~1, adjacent to a fairly steep intermediate region, ultimately leading to a domain where $P_0(t_s)$~0. It would generally be desirable to operate a crystallization process well within in the $P_0(t_s)$~1 region. The most practical way to achieve this is to use the highest possible shrinkage rate (and thus lowest practical film thickness) at a given temperature and droplet size. Next, to explain the optimal temperature reported in Table 2, note that the shrinkage rate at a given film thickness increases with temperature, and while film thickness is the tunable processing parameter, the shrinkage rate is what ultimately influences the outcome of the process. If the outcomes of experiments conducted at h_f =1 mm and d_0 =85 μm at different temperatures (#5, 10-13 in Table 2) are compared to simulated $P_0(t_s)$ values using a shrinkage-rate temperature relationship fitted to the measured shrinkage rates (see Figure 40 of Appendix B), the experimentally observed trend is recovered (Figure 16d).

Finally, the validity of the model was further tested in the following way. Three SA sizes were selected as targets under two selected conditions of d_0 and h_f within the previously described range. Measured f_I and simulated $P_0(t_s)$ data were compared to determine whether or not the model proved to be accurate in

predicting the superior processing conditions (i.e. which condition produced the higher fraction of Morphology I SAs). The experimental conditions and the results are presented in Table 4. It can be seen that the model provided correct predictions in all three cases, even though all the experiments were performed in the steep intermediate range of $P_0(t_s)$ described above.

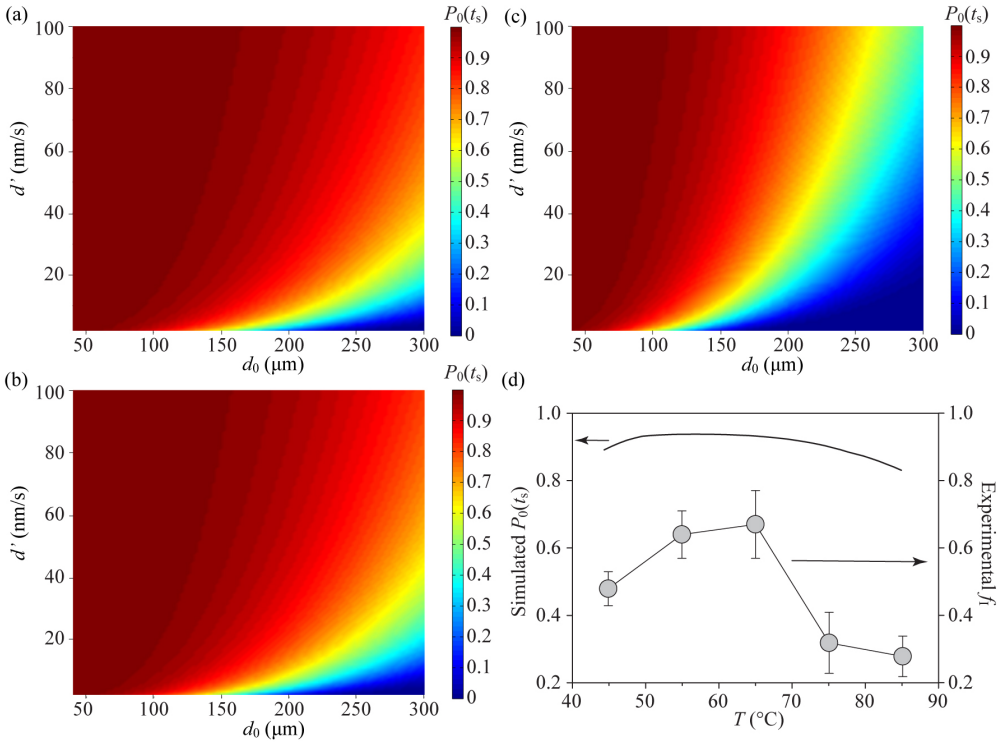

Figure 16: a-c) Simulated surface plots of $P_0(t_s)$ in the two-dimensional d_0 -d' space, at a) T =50 °C, b) T =60 °C, and c) T =70 °C. Note the expansion of the low $P_0(t_s)$ region with increasing temperature. d) Simulated $P_0(t_s)$ compared to experimental results for d_0 =85 μm and h_f =1 mm at different temperatures (shrinkage rate-temperature relationship used in the simulations is provided in Figure 40 of Appendix B). The model qualitatively captures the experimentally observed trends.

3.4 Concluding Remarks

The work presented in this chapter build has shed light on the dynamics and morphological outcomes in the thin-film spherical crystallization of glycine. Specifically, the effects of droplet size, shrinkage rate, and temperature were studied with the aim of understanding and delineating crystallization conditions that ensure spherulitic crystal growth in individual droplets, ultimately yielding compactly packed spherical crystal agglomerates (SAs). Experiments indicate

Table 4: Summary of the validation exercise to test the predictive capability of the model.

#	d_0	d_A	T	h_f	d'	$P_0(t_s)$	f_I
	μm	μm	°C	mm	nm/s		
V1	73±5	53±4	55	0.8	4.7	0.98	0.91±0.03
V2	73±5	53±4	75	1.3	6.7	0.91	0.26±0.05
V3	110±8	81±6	60	0.6	31	0.98	0.94±0.03
V4	110±8	81±6	50	0.9	3.3	0.91	0.71±0.07
V5	157±9	110±7	65	0.8	13	0.87	0.78±0.05
V6	157±9	110±7	70	0.65	51	0.95	0.91±0.01

that a smaller initial droplet diameter, a higher linear shrinkage rate, and a lower temperature favor the formation of complete SAs, while the opposite leads primarily to incomplete spherical agglomerates and faceted single crystals. The observations were analyzed within the framework of a simple physical model based on classical nucleation theory and the theory of non-homogeneous Poisson processes, which accurately captured the overall trends. According to this model, smaller droplets and faster shrinkage rates (in thinner films) favor the formation of compact SAs at a given temperature, and lower temperatures generally favor compact SA formation at a fixed drop size and shrinkage rate. The next chapter will focus on implementing these insights in a continuous, scalable thin-film evaporator.

4 Continuous Emulsion-based Crystallization

The previous two chapters demonstrated the production of unprecedentedly uniform SAs with a great reduction in processing time (as compared to conventional batch systems). However, the setup presented above couples continuous emulsion generation with batch evaporation, a shortcoming that was highlighted in a recent review that called for new, continuous pieces of equipment [216]. Therefore, it would be desirable to shift from a semi-batch crystallization step to a continuous one to be able to fully exploit the advantages of continuous microfluidic emulsion generation and to enhance production rates by accommodating a larger flux of emulsions from several emulsion generators.

This chapter presents a continuous emulsion-based crystallization platform based on the concept of the belt evaporator. Two prototypes were fabricated. The first prototype serves as a proof-of-concept whilst gaining understanding of the key parameters that have to be controlled. The second prototype was fabricated to use the gained understanding to test ideas for improvement. It was found that these apparatuses could produce good quality glycine SAs at rates on the order of 1-10 g/day. As the second prototype has a volumetric footprint of only ~10 L, it can be straightforwardly scaled up to industrially relevant rates by parallelization.

4.1 Prototype I: a Proof-of-concept

A conceptual schematic of the setup and is shown on Figure 17, while a model and a photograph of the prototype is shown on Figure 18: the key idea is a heated conveyor belt that has been adjusted to the requirements of emulsion-based crystallization. A continuous stream of the emulsion is dispensed onto one end of the belt, which then conveys the emulsion over a heated region to facilitate evaporative crystallization. Residence time is adjusted by adjusting the speed of the belt so that at a given operating temperature all of the droplets crystallize by the time they reach the outlet end, where a scraper is used to collect

the product.

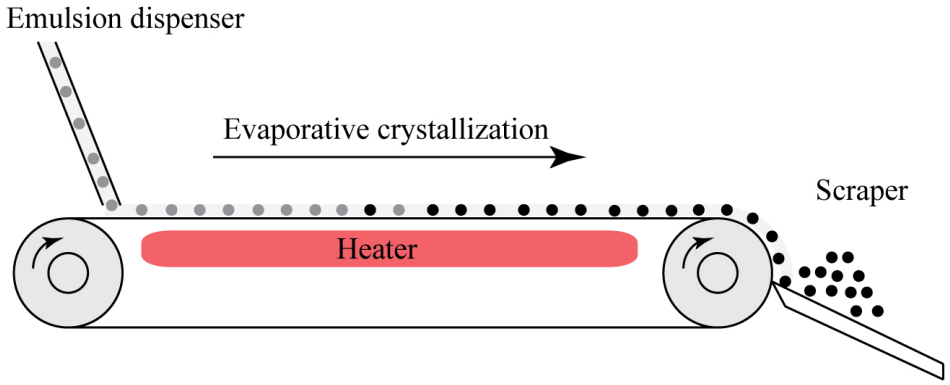

Figure 17: A conceptual schematic of the continuous crystallizer. Emulsions are dispensed on a heated conveyor belt, where solvent is evaporated from the droplets, which, in turn, leads to the formation of SAs. A scraper is used to collect the product.

4.1.1 Experimental

All parts were purchased from McMaster-Carr. The setup is mounted on structural framing and custom-made connecting elements. In this setup, a 2" diameter (6" width) conveyor belt pulley - coated with 1 mm of silicone rubber for better grip - is driven by a 0.6 rpm (maximum) DC gear motor equipped with a speed controller, while the other pulley is a 2" shaft. The two pulleys were horizontally aligned and their centers were mounted 50 cm apart, which allowed for the adjustment of residence times between 5 and 40 minutes. The belt is made of 6" wide, 0.1 mm thick stainless steel shim stock welded into a loop, and is tensioned manually. The heater is a 18"X6", 4 mm thick aluminum sheet that has a 12"X6", 720 W heating strip attached to its bottom side, while the top side is in direct contact with the belt. Temperature is controlled by a PID controller that gets feedback from a thermocouple attached to the aluminum sheet ~1 cm from the edge of the heating strip. The materials for preparing monodisperse microfluidic emulsions of an aqueous glycine solution in dodecane are identical to those used in the previous two chapters, as are the characterization techniques used on the final product. To generate the emulsions, however, a

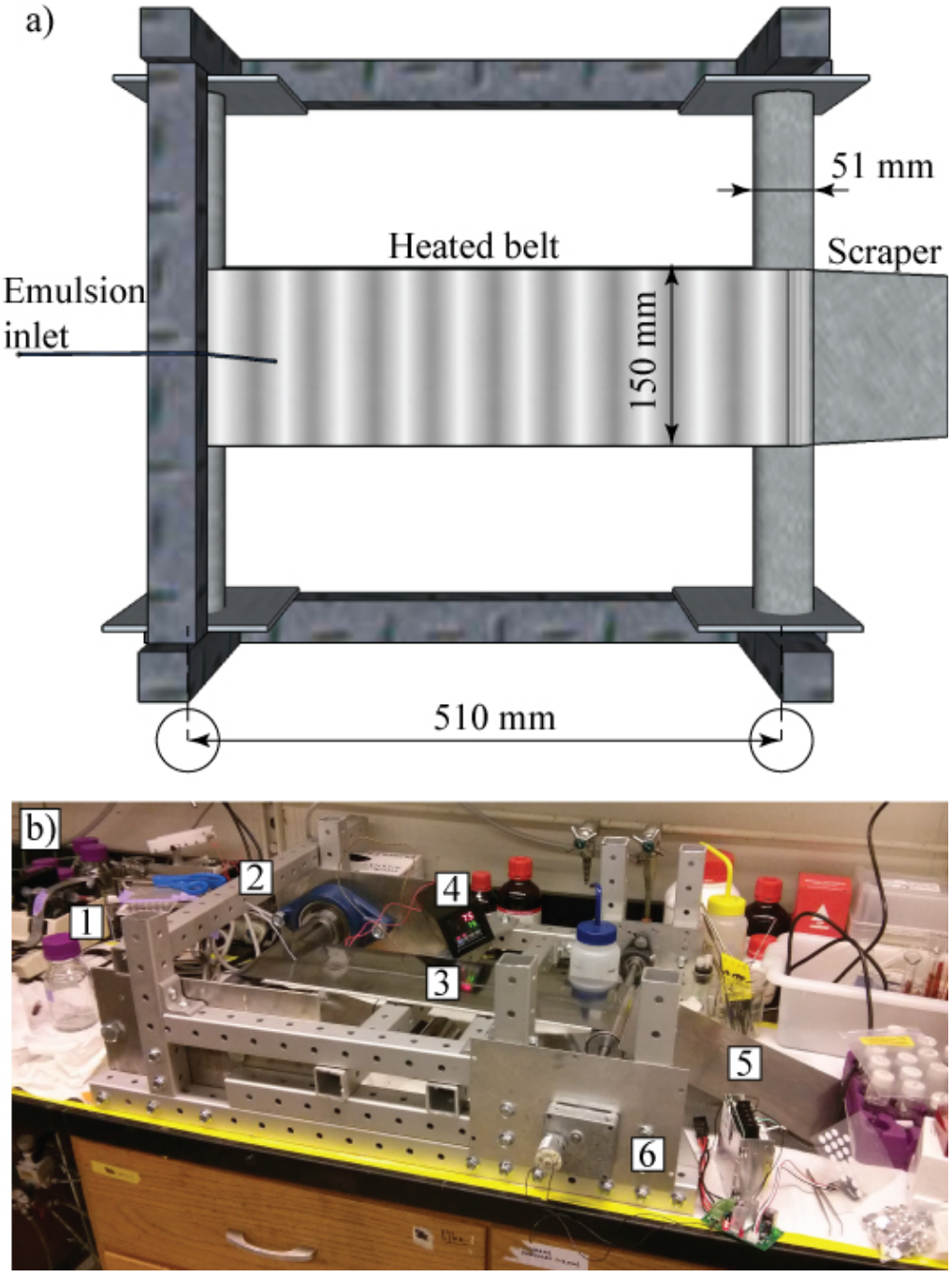

Figure 18: a) To-scale model of prototype, top view with key dimensions indicated; b) photograph of the prototype. The important parts are marked with numbers: 1) syringe pumps & microfluidic device; 2) inlet tube; 3) heated conveyor belt; 4) PID temperature controller; 5) scraper; 6) gear motor and speed controller.

robust flow-focusing PMMA emulsion generator was used instead of glass capillary devices. These PMMA devices are essentially single-channel versions of the high-throughput emulsion generator developed by Conchouso *et al.* [217]. The continuous and dispersed phases were infused using syringe pumps similar to those used in the previous chapters. The generated emulsions were then dispensed through an OD=1/16" and ID=0.01" PTFE tube on the belt at the starting point of the heating element (~1" from the center of the pulley) to maximize useful contact time.

4.1.2 Results and Discussion

Belt temperature at several locations was measured with a thermocouple in order to determine the temperature profile of the belt under the three control temperatures used for demonstration (35 °C, 55 °C, 75 °C). These profiles are presented on Figure 19. As can be seen, temperatures fluctuate over relatively wide (but distinct) ranges, with the edges and the inlet side being slightly cooler than the central areas. Although for a precise industrial device these fluctuations will have to be reduced (a few °C is considered acceptable in crystallization processes [18]), they did not prove to be an impediment to the production of quality SAs under any conditions. One industrially relevant SA diameter, ~50 μm was chosen for proof-of-concept studies. These could be obtained at a continuous phase flow rate of 0.2 ml/min, and a dispersed phase flow rate of 0.02 ml/min. A single stream of emulsion was used. The necessary residence times for complete crystallization for the three temperatures used were determined to be ~30 min (35 °C), ~15 min (55 °C) and ~6 min (75 °C). The width of the dispensed stream varied with belt speed between ~1 and ~5 cm, which means that a 6" belt would allow for 3 parallel streams at the lowest belt speed setting. The product was collected using a stainless steel scraper for further analysis, and the belt was stopped and manually cleaned after each turnaround to simulate a cleaning and drying mechanism that would be present in an industrial apparatus.

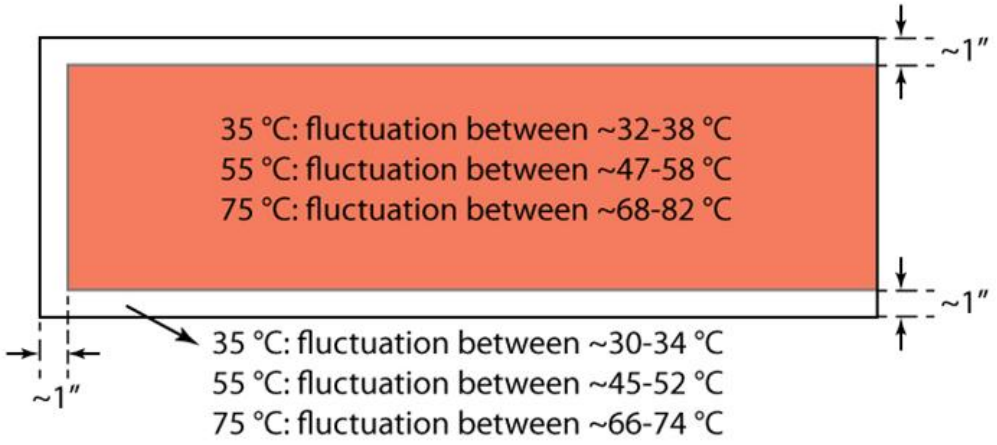

Figure 19: Belt temperature profile of the prototype on the heated section (there is an 1" un-heated section between the heater and each pulley). The inlet side is on the left of the figure. Measurements were taken at the nodes of a 1" mesh on the 18"X6" section. Note the relatively large fluctuations and the slightly lower temperatures at the edges and the inlet side. These fluctuations did not have a noticeable effect on the quality of the product.

Figure 20a-c shows SEM images of the product obtained from the scraper under the three different temperatures, as compared to the product from semi-batch crystallization (obtained by dispensing a drop of emulsion onto the stationary belt at a particular temperature setting and waiting until crystallization finishes). The images show that the SAs obtained from the scraper are indistinguishable in their quality from their semi-batch counterparts, thus proving the viability of the concept. Figure 20d presents similar results obtained from an experiment performed with an emulsion generated in batch (crystallization performed at 80 $^{\circ}$C control temperature), which points out that this setup can also compliment traditional methods of emulsification. If 0.02 mL/min (20 μL/min) is taken as a benchmark for dispersed phase flow rate, a glycine solubility of 24.41 g/100 g water [83] and a solution density of ~1.1 g/mL is assumed [215], the nominal productivity of this prototype is ~5.8 g/day.

Although this prototype - tested on a robust, well-studied emulsion-based crystallization process - proves that the apparatus is conceptually viable, three major aspects need to be improved. Firstly, dispensing the emulsion directly on the belt results in a film thickness that is entirely controlled by the spreading

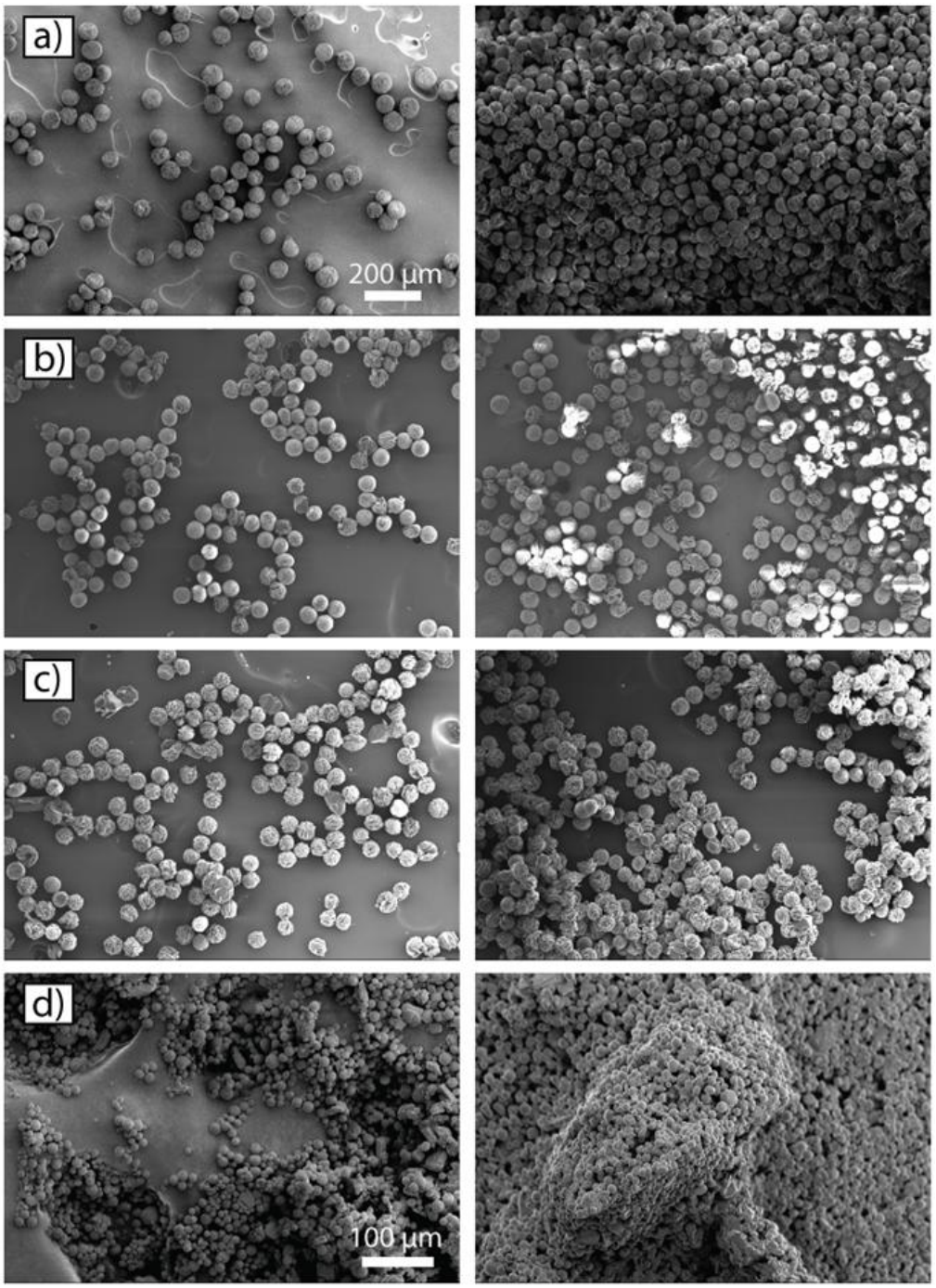

Figure 20: Comparison of SEM images of 50 µm glycine SAs produced by the prototype and the semi-batch method described in Chapter 2 under different control temperatures: a) 35 °C, b) 55 °C, c) 75 °C. Left column: semi-batch SAs, right column: SAs collected from the scraper. The scale bar is valid throughout a-c; d) Comparison of SAs obtained from the semi-batch method (left) and from the scraper (right) when batch emulsification was used at a heater temperature of 80 °C and a residence time of 6 minutes. As can be seen, there is no qualitative difference between the SAs obtained from the semi-batch method and those obtained from the prototype.

properties of the continuous phase on the belt material. A nominal film thickness for such cases can be roughly estimated if the contact angle, θ_c , between the substrate and the continuous phase is known, e.g. by first estimating the width of the dispensed stream by the θ_c /2 method [218] and then using the $h_f \cdot w \cdot v_b = Q_t$ relationship to calculate the nominal film thickness. Here, w is the estimated stream width, v_b is the belt velocity and Q_t is the total flow rate of the emulsion. Moreover, belt irregularities (such as minor folds in the shim stock) resulted in a tendency of continuous phase drainage to the side. Therefore, there's a need to control the stream width and the film thickness, perhaps with the horizontal confinement of the film (i.e. division of the belt into trenches of controlled width and height). Secondly, a more precise control of the environment, i.e. temperature and humidity is needed (which requires an improved heater design and an enclosure for the setup). Finally, it would be desirable to reduce the volumetric footprint of the unit to increase productivity per unit volume. A second prototype built to implement these improvements is presented in the next section.

4.2 Prototype II: an Improved Design

4.2.1 Experimental

A model and a photograph of the prototype is shown in Figure 21. All parts were purchased from McMaster-Carr, unless indicated otherwise, and the apparatus was fabricated in a machine shop. The setup is enclosed in a 1" thick acrylic box that has inner dimensions of 557x117x60 mm. The two 1/2" shafts that hold the belt are placed 20" apart, one of which is attached to a 5 rpm (maximum) DC gear motor. The belt was custom made of 2" wide, 1 mm thick silicone rubber, and a strip of 1/2" wide oil-resistant tape (3M-444) was placed on each side to create a 1" (~25 mm) wide trench of ~100 μm depth. The heater is an 18"x2" mineral insulated strip heater custom made by PTI Singapore. This heater has a maximum output of 1000 W, but is operated at 30%. The heater is suspended

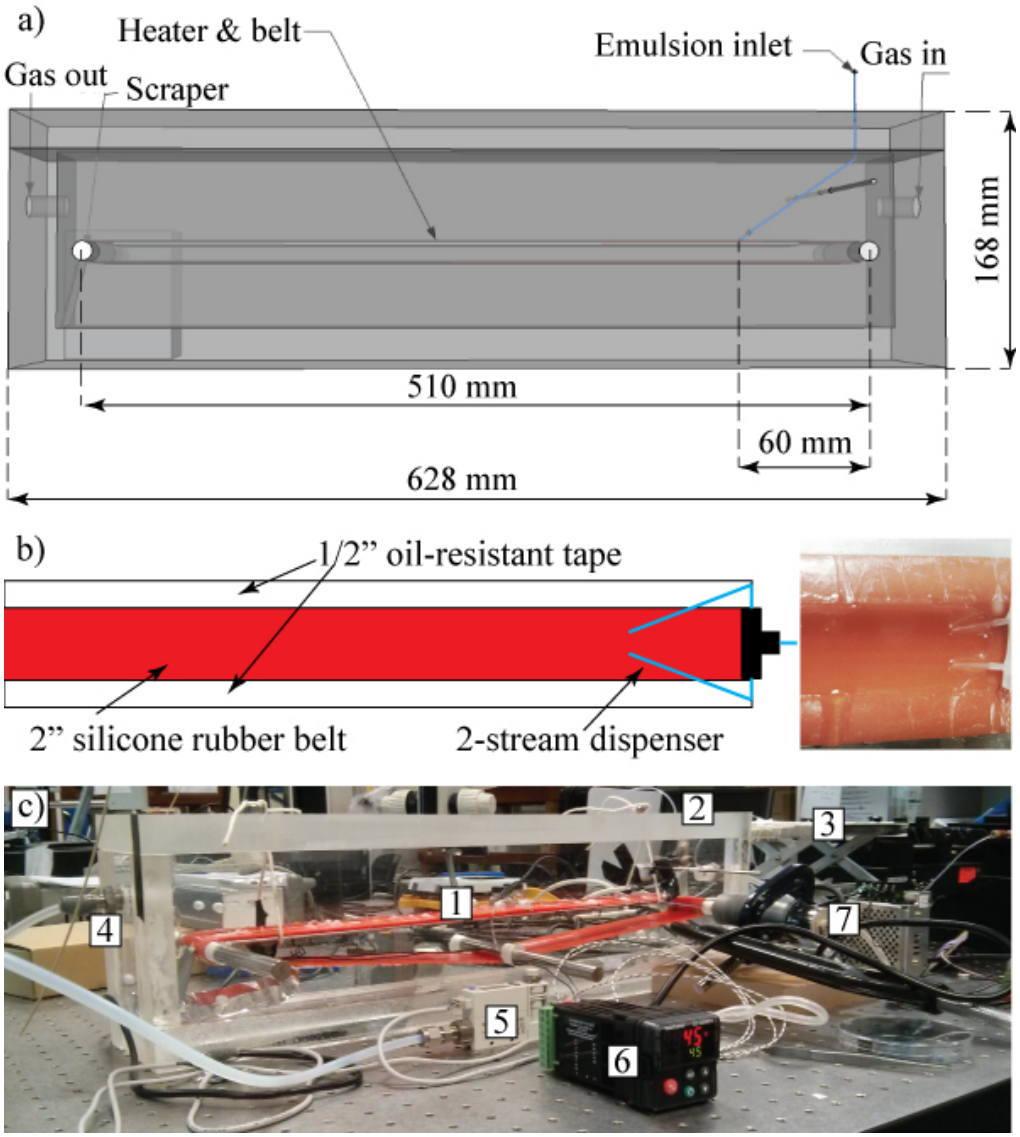

Figure 21: a) to-scale model of prototype with main dimensions indicated; b) schematic of belt setup with photograph of emulsion inlet and film at the 38 °C experiment, as listed in Table 5; c) photograph of the second prototype: 1) belt with heater; 2) emulsion inlet; 3) emulsion generator & syringe pumps; 4) gas outlet (inlet on the other end); 5) gas flow controller; 6) temperature controller; 7) gear motor.

below the belt so that the belt slides on its surface, giving a heated length of ~45 cm. Heating temperature is controlled (with an accuracy of 1 °C) by a Watlow EZ-zone PID controller (also purchased from PTI Singapore) that gets feedback from a thermocouple attached to the surface of the heater. Pure nitrogen gas is flown through the enclosure to flush out the evaporated solvent. The flow rate of this gas is controlled by a mass flow controller (SMC PFM750S, purchased from RS Components Singapore), and it is set to 4 L/min, which corresponds to a gas residence time of 1 minute. The emulsions are dispensed through an OD=1/16" and ID=0.01" PTFE tube. The stream of emulsion was split into two with a T-junction so that the resulting two inlets could provide a more uniform distribution of the emulsion on the belt. The two inlets were then placed ~6 cm from the input end of the belt, which leaves a utilizable belt surface of ~45 cm x 2.5 cm. A stainless steel scraper was used for sample collection. The scraper was placed in an aluminum box to prevent dodecane leakage and to aid sample collection. Emulsions were generated in the PMMA device described in the previous section.

4.2.2 Results and Discussion

Four preliminary experiments were carried out to gain insights about feasible operating ranges of the setup. First, T_B , the surface temperature of the belt as a function of T , the set temperature was measured with a thermocouple at the two edges and the center of the belt at every 5 cm of heated length at the highest speed setting, ~24 cm/min (Figure 22a). Figure 23 shows T_B as a function of T . It was found that the belt surface temperature only fluctuates within the 1 °C measurement error of the thermocouple, a remarkable uniformity compared to the previous prototype. Next, two experiments were carried out with a stationary belt (all trials in triplicate). First, to determine the minimum and maximum nominal film thickness achievable, 2.5x2.5 cm segments of the belt were isolated with oil-resistant tape, and pure continuous phase was dispensed at three

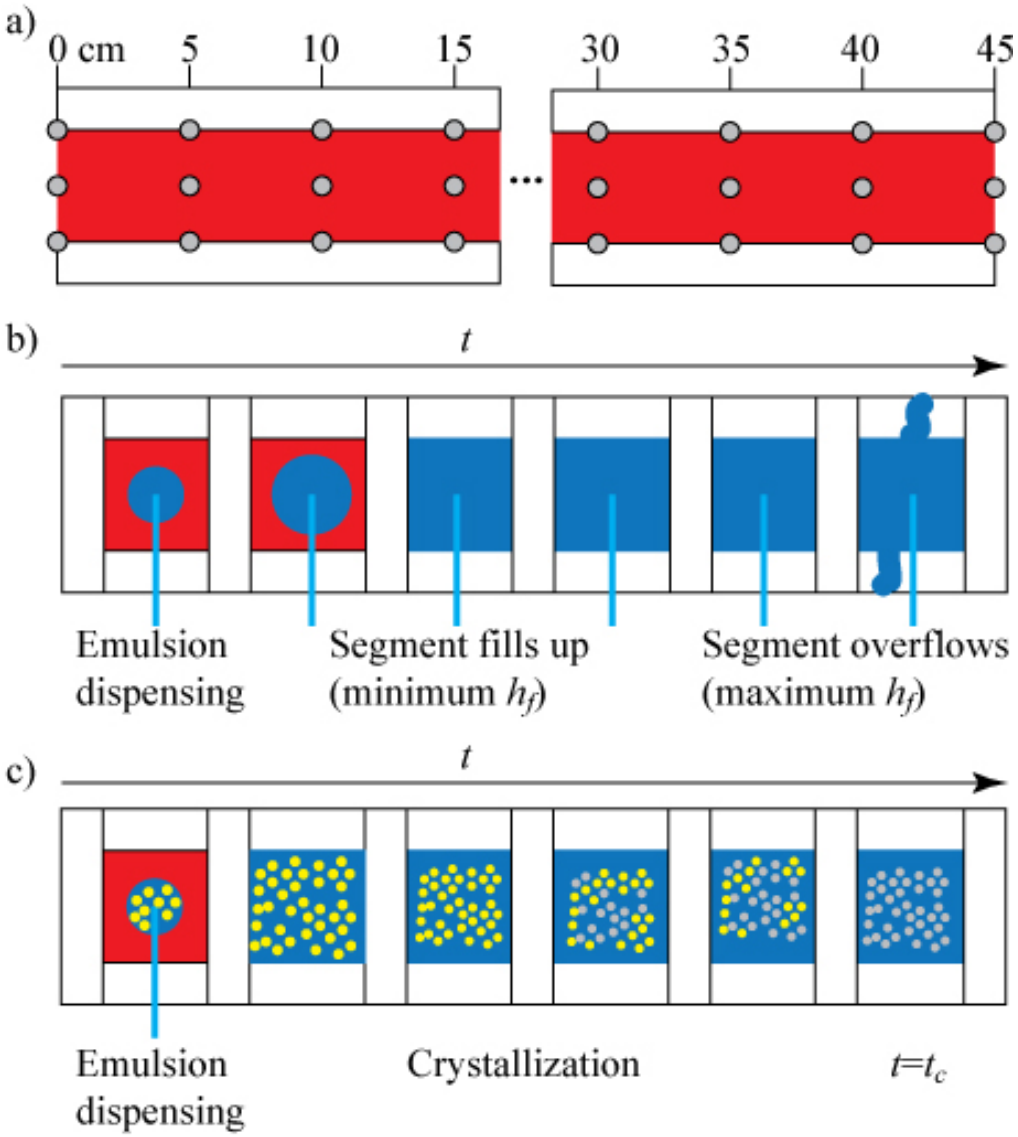

Figure 22: a) Measurement of belt temperature as a function of heating temperature b) the measurement of minimum and maximum film thicknesses with a stationary belt; c) the measurement of crystallization times on a stationary belt.

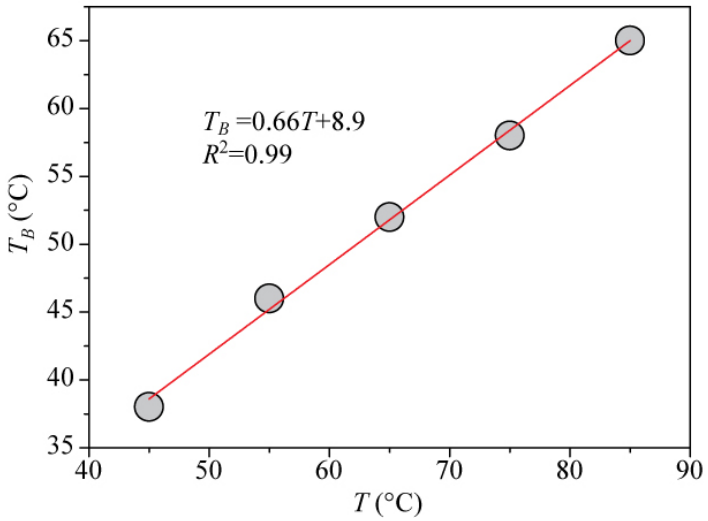

Figure 23: Belt surface temperature T_B as a function of set temperature T . The temperature of the belt fluctuated only within the measurement error of the thermocouple (hence the lack of error bars).

belt temperatures, 38, 48, and 58 °C (roughly corresponding to three temperatures used in Chapter 3) until the segments filled up and overflowed (Figure 22b). It was found that a nominal film thickness of ~80 μm is the minimal amount that can fill up the channel, and overflow occurred at ~160 μm. Subsequently, crystallization experiments were carried out in these segments (Figure 22c) at the three temperatures and the two extreme film thicknesses to determine the time required for crystallization. These experiments used 50 μm agglomerates (generated under $Q_{CP} = 200$ μL/min and $Q_{DP} = 20$ μL/min, identically to the previous section), because these relatively small SAs are expected to form slower - as shown in Chapter 3 - and can therefore be used to get a conservative (upper) estimate of time required for crystallization. Figure 24 shows the results of these measurements. Difficulties in imaging the crystallization process (due to the glossy belt material and the fact that the distance between the belt and the top of the enclosure is larger than the focal length of the available microscopes) resulted in a large standard deviation of crystallization time results. Therefore, twice the mean was taken as a minimum crystallization time when determining feasible operating conditions. Since the flow rate of the emulsion and the film thickness also determines an actual residence time, successful operation of the

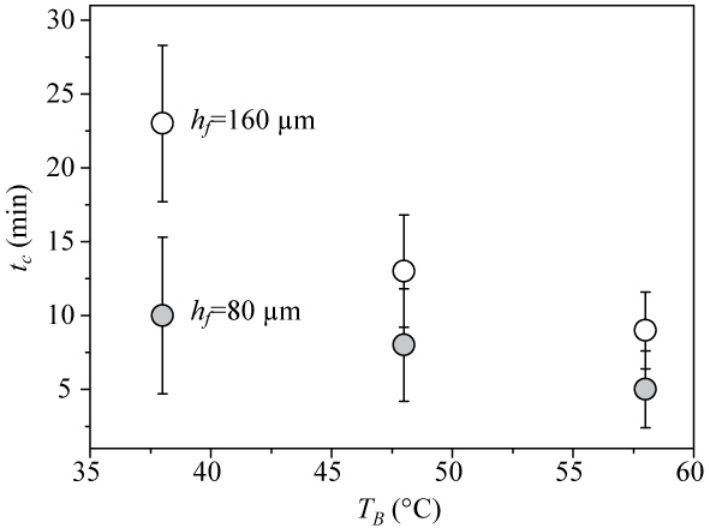

Figure 24: Crystallization time, t_c , as a function of belt surface temperature T_B and nominal film thickness h_f .

process requires this residence time to be more than the time required for crystallization. Finally, from a productivity standpoint - since the dispersed phase carries the crystallizing compound - a high volumetric ratio of dispersed to continuous phase would be desirable. Therefore, several semi-batch crystallization experiments - similar to those presented in Chapter 2 - were performed to determine the minimum CP:DP volume ratio under which secondary agglomeration - the tendency of agglomerates to stick together - is still negligible. This ratio was found to be approximately 3:1.

Based on the fact that crystallization times at a nominal film thickness of 80 μm are less than half of crystallization times at 160 μm (an observation consistent with the film thickness-evaporation time relationship seen in Chapter 3), three total flow rates were selected for productivity measurements at the three different belt temperatures and a fixed nominal film thickness of 80 μm. This nominal film thickness is defined by the width of the trench, the total flow rate, and the belt velocity (i.e. the residence time, as listed in Table 5). Flow rate ratios were kept at CP:DP=3:1 to maximize productivity. The experiments were run for 2 hours (each performed twice), and the crystallized sample was collected and dried (overnight in a 70 °C oven) and weighed for productivity measurements, while minute amounts of wet samples were collected and dried at

room temperature for SEM analysis. The experimental conditions, along with the results are summarized in Table 5. Productivities of up to 5.3 g/day were

Table 5: Summary of the experimental conditions and the outcome of the continuous crystallization runs. T_B : belt temperature; Q_t : total flow rate (always at CP:DP=3:1; t_r : residence time (always at a nominal film thickness of 80 μm); d_A : average agglomerate diameter; Y_e : experimental productivity; Y_t : theoretical productivity.

T_B	Q_t	t_r	d_A	Y_e	Y_t
°C	μL/min	min	μm	g/day	g/day
38	40	23	73±5	2.1±0.2	2.6
48	65	14	70±4	3.3±0.2	4.2
58	95	10	56±4	5.3±0.3	6.2

measured, typically reaching ~80% of the theoretical yield. SEM comparison of the SAs obtained from the scraper to their semi-batch counterparts gives further interesting insights into design criteria (Figure 25). As can be seen, samples collected from the scraper contain a significant amount of broken SAs, as opposed to the purely spherical populations observed with the previous prototype. These differences may arise due to two factors: firstly, the proof-of-concept studies used a smaller SA diameter (<50 μm). Observational evidence suggests that small agglomerates 'age' less and have a more compact structure (e.g. see Figure 5 of Chapter 2). This, in turn, results in less attrition during scraping and sample collection. Secondly, although a CP:DP ratio of 3:1 is sufficient in a semi-batch setup to reduce secondary agglomeration and undesirable interaction between the droplets to an acceptable level, a scenario of a constantly moving film might require a larger ratio. The optimization of a future industrial process - be it pure crystallization or an advanced formulation, such as the one presented in the next chapter - will require the adjustment of both the flow rate ratio and the size and morphology of the generated SAs. While such optimization exercises are beyond the scope of this study, the preparation for an industrial process will

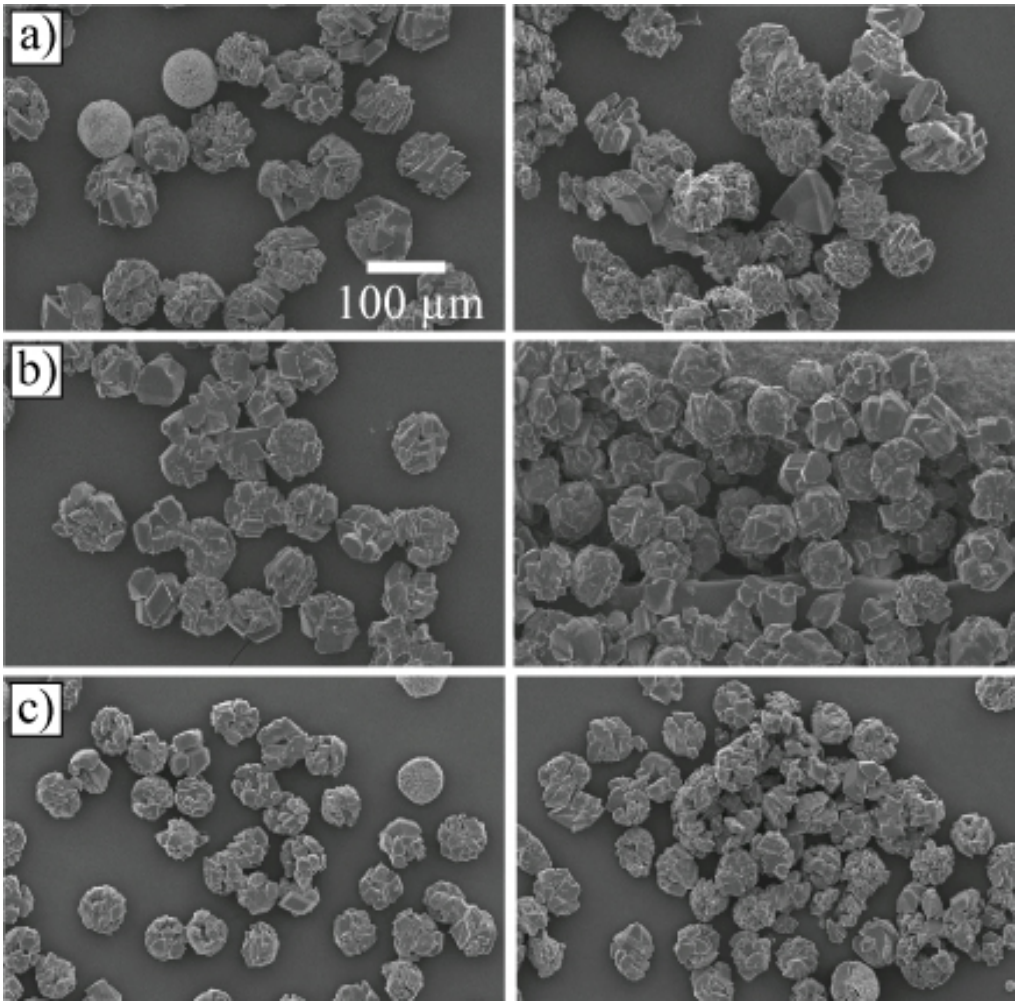

Figure 25: SEM images of SAs obtained from the second continuous crystallizer at the three different belt temperatures, as compared to their semi-batch counterparts. Left column: semi batch SAs; right column: SAs collected from the scraper. a) 38 °C; b) 48 °C; c) 58 °C. The scale bar applies for all images.

require a simultaneous control of flow rate ratio and droplet size, a feat achievable through the design of microfluidic device geometry or the addition/removal of continuous phase after emulsion generation.

4.2.3 Conclusions

In conclusion, this prototype demonstrated the continuous production of glycine SAs on the ~5 g/day scale. The following improvements were implemented, as compared to the first prototype: 1) superior heater design provides a very uniform belt temperature; 2) the application of an inert flushing gas provides a controlled atmosphere for the process whilst removing the evaporated solvent; 3) confinement of the dispensed emulsion to a trench provides an improved control over film thickness; 4) the volumetric footprint of the entire apparatus was reduced to ~10 L. With this demonstration and with the experience gained regarding the design criteria for continuous emulsion-based crystallization processes, the stage is set for an industrial application. However, there are still some challenges that need to be overcome before the first microfluidics-enabled continuous crystallizer surfaces in the industry. Some of these challenges - such as improving the yield of the process and the robustness of the device - are purely a matter of design and fabrication, and will therefore not be addressed in detail. On the other hand, challenges in designing robust spherical particles in microfluidics and conceptual considerations for scale-up are of great relevance to R&D scientists. Therefore, these ideas will be presented in the next chapter, which discusses the future prospects of this thesis.

5 Future Prospects

This chapter will give the reader of the overview of possible future paths that this thesis opened up for exploration. First, advanced drug-excipient formulations with an exquisite control of API polymorphism are explored in the context of an ongoing study. Next, the path towards the industrial application of microfluidic emulsion-based crystallization platforms is laid out. Finally, interesting fundamental directions that could be explored with these platforms are summarized.

5.1 Advanced Microfluidic Formulations

While a pure, readily crystallizing API compound, glycine, is suitable for the proof-of-concept studies presented in the previous chapters, industrial formulations are rarely this simple. Firstly, due to the high potency of most new API compounds, the final solid form often contains only a minute amount of API crystals. This necessitates the co-formulation of actives with excipients [219]. Secondly, APIs are often complex molecules that can pack into several conformational polymorphs with very similar stabilities [43]. More often than not, these polymorphs appear concomitantly, resulting in a product with inconsistent downstream properties. Therefore, there is a great need for formulation methods that can simultaneously control polymorphism and ensure consistency in the size, shape, and composition of the solid form.

In a study currently in progress in our group - and the specifics of which will be published elsewhere - ROY, a molecule exhibiting an extreme (and colorful) case of conformational polymorphism [220], was co-formulated with an excipient into monodisperse ~150 μm spherical particles using a microfluidic thin-film evaporation platform similar to the one presented in Chapter 3. The polymorphic outcome of crystallization could be tuned by changing the film thickness of the continuous phase (and thereby, the rate of evaporation).

First, control experiments were carried out without the excipient. Generally,

crystallization took 4-5 hours (even in the thin-film case), and emulsions were comparatively unstable. Optical micrographs and SEM images of the resulting particles are shown on Figure 26. As can be seen, particle morphology is inconsistent, and polymorphs of two different colors (yellow and orange) form concomitantly. The situation changed dramatically when experiments were car-

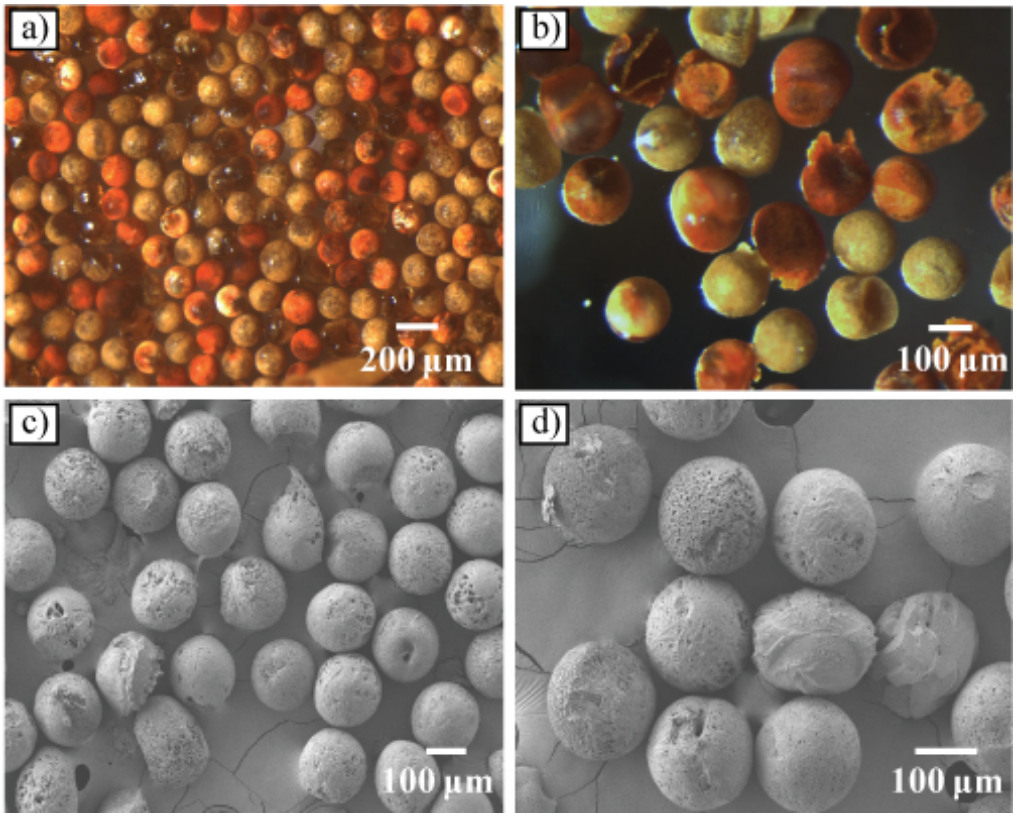

Figure 26: Pure ROY spherical agglomerates. As can be seen the morphology and the polymorphic outcome of the product is inconsistent. a) and c): thick film; b) and d): thin film.

ried out with the excipient. Firstly, overall crystallization times were reduced to ~30-45 minutes (thin film) and 3 hours (thick film). Secondly, as shown in Figure 27 spherical particles of remarkable uniformity were obtained. Finally, and most importantly, thin film experiments exclusively resulted in the crystallization of one of the yellow polymorphs, and thick film experiments exclusively yielded an orange polymorph.

Such systems, in which excipients enhance nucleation (manifested in the reduced crystallization times) and aid polymorphic control in co-formulation scenarios, can be anticipated to become widespread in microfluidics-based spheri-

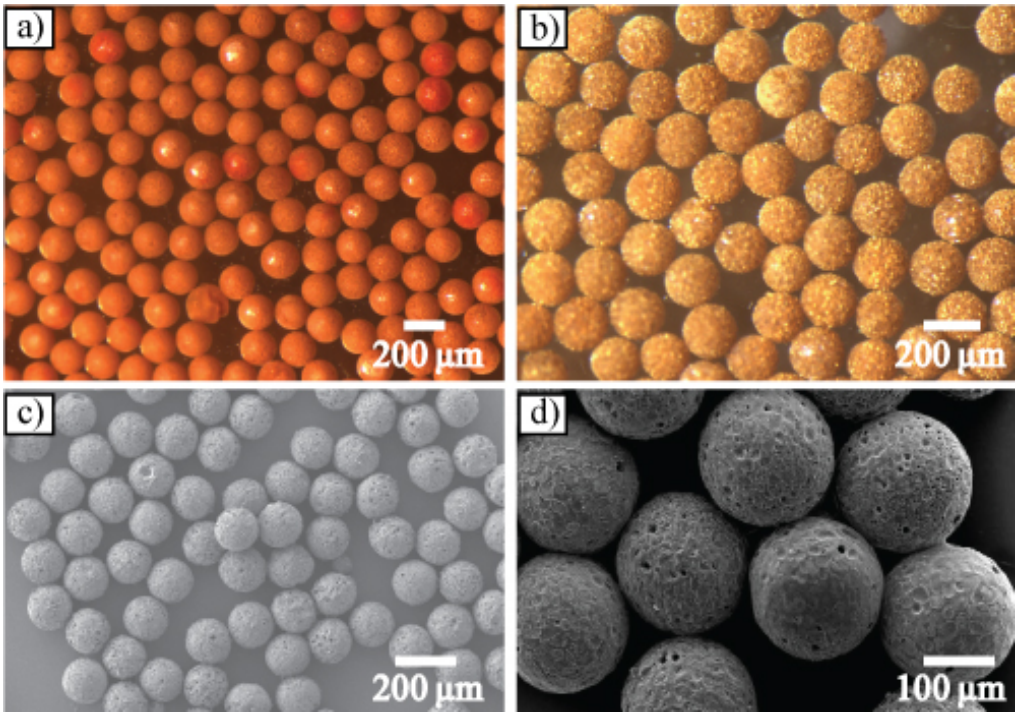

Figure 27: Co-formulated ROY-excipient spherical particles. By tuning the film thickness, the polymorphic outcome of the process can be changed. a) and c): thick film; b) and d): thin film.

cal crystallization techniques. Future work in this area will include the discovery of new microfluidic drug-excipient co-formulation methods, and the application of the discovered techniques to industrially relevant actives. There is a virtually infinite variety of additives and configurations that could be explored to improve the structural or polymorphic outcome of the process, but for the sake of brevity only one will be highlighted: recently our group has demonstrated the co-formulation of an excipient with a hydrophilic and a hydrophobic API compound into monodisperse spherical particles using microfluidic double emulsions [203]. Such advanced API-excipient co-formulations are of great interest, because they can be expected to be the primary choice in potential industrial applications.

5.2 Towards Industrial Application

The prototypes presented in Chapter 4 are suitable for the continuous production of high quality SAs. However, there are two challenges that have to be solved before the industrial application of such apparatuses. Firstly, while

the production rate of ~10 g/day is suitable for some small-volume compounds, scaling it up by at least an order of magnitude would open up a host of other opportunities.[1] Secondly, some formulations, such as the one presented in the previous section, require relatively thick continuous phase films (more than 0.5 mm) with precise control. Deeper trenches, and a dispenser that is flush with the trench could enable the use of such film thicknesses. However, as the film thickness increases, the influence of gravity becomes dominant over interfacial forces [221], which could result in the drainage - and thereby the disruption of the uniformity - of the film at the outlet end. Therefore, the confinement of the film along the moving direction may be necessary for thicker films. The following sections present tentative solutions to these two problems.

5.2.1 Scale-up

Increasing production rates is straightforward both conceptually and practically, as parallelization is a well-known method for the scale-up of microfluidic systems [222]. However, the construction and operation of the bench-top prototypes provided some valuable practical guidelines for scale-up. To start with, in an industrial setup, high-throughput microfluidic emulsion-generation will be necessary. Fortunately, several such technologies emerged recently, e.g. massively parallelized flow-focusing devices [217], microfluidic post arrays [223], or emulsion generation driven by gradients of confinement [224]. The generated emulsions (and therefore, the emulsion generators) will also have to be optimized for the quality of the crystals and the productivity of the process - as seen in Chapter 4. Since syringe pumps are limited by the volume of the syringes, these emulsion generators will most likely be driven by continuous peristaltic pumps. Next, to ensure consistent evaporation and crystallization times, a precise control over nominal film thickness will be necessary. Such control can be achieved by changing the width of each 'trench' (fabricated into the belt, rather

[1] Based on discussions with GSK personnel.

than added with tape) so that a single stream of emulsion fills it up (i.e. the width of the trench is less than the spread of the emulsion stream on the belt material). In order to accommodate for systems requiring both long and short evaporation times, industrial setups will likely have longer belts that are able to move at a wide range of velocities. The material of the belt should be selected based on two considerations: 1) it should possess a relatively high heat conductivity to ensure a uniform temperature, 2) it should be preferentially wetted by the continuous phase to prevent droplets and SAs from sticking to the belt. A single belt, contained in a single enclosure, will accommodate several parallel trenches, thereby reducing the excess volume taken up by the enclosure wall. Finally, the continuous unit will have to be integrated with downstream steps, such as filtration and drying. To achieve such integration, the stationary scraper will have to be complemented with a stream of flushing liquid that serves a dual purpose: mobilizes the resultant powder for downstream processing, and cleans the belt from residual particles. This flushing liquid will most likely be a non-solvent that is miscible with (or identical to) the continuous phase.

5.2.2 Accommodating Thicker Films

As seen above, some formulations require relatively thick continuous phase films with a precise control over the film thickness. The continuous thin-film evaporator described above, however, only caters to processes that benefit from higher shrinkage rates (and thinner films). Therefore, a need will inevitably arise for continuous evaporator designs that are capable of handling thicker films. A schematic of one such design is presented in figure 28. In this design, the belt is compartmentalized into 'carts'. Initially, the emulsion is dispensed on a stationary belt until the first cart is filled to the desired level. Next, the belt moves so that the dispenser jumps to the second cart. The carts are then conveyed as evaporation and crystallization progresses. Finally, as crystallization is finished and the cart reaches the end of the belt, a stream of washing liquid flushes the parti-

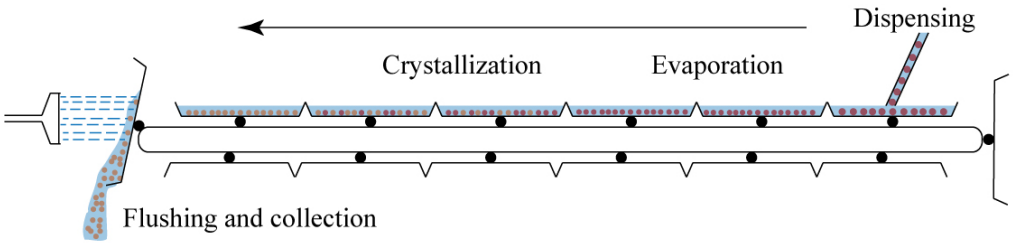

Figure 28: Schematic of a continuous evaporator design for systems that require well-controlled and relatively thick continuous phase films.

cles from the carts to the next processing step. To allow for a higher throughput, the carts could be 'parked' outside the moving belt, and only re-enter when crystallization is complete.

5.3 Fundamental Directions

As shown in Chapters 2 and 3, the on-line microscopic monitoring of crystallization from monodisperse emulsions enables the investigation of crystallization dynamics in emulsion droplets. Based on these studies, it can confidently be stated that a sufficient phenomenological understanding of the process has been gained. However, as the individual phases of crystallization influence the final quality of the product obtained, they all deserve further attention. Possible future research directions in these fields are summarized in the sections below.

5.3.1 Nucleation

The investigation of nucleation from monodisperse microfluidic emulsions should be a top priority for future studies. Firstly, Chapter 2 hypothesizes that the reason why the probability of no nucleation over time follows a compressed exponential model is the interaction between droplets and crystallized SAs. While this hypothesis is certainly backed by evidence, it might not explain the phenomenon entirely. Recently, Sear pointed out that a compressed exponential process may arise simply due to nucleation at a surface that changes irreversibly with time [88]. With a bit of abstraction, this 'surface' can be set to be equivalent to changing conditions within the droplets in a crystallizing population.

These changes in conditions can arise if the droplets still shrink after reaching the 'critical' size, albeit at an unnoticeably slow rate. To simulate one such case, the model developed in Chapter 3 is invoked. It is assumed that a 100 μm droplet at 59 °C shrank to d_c - 73 μm - at an infinitely high rate, so that P_0 remains 1 by this point in time. Then, it is assumed that the droplet continues to shrink 5% of d_c (~3.6 μm, i.e. within experimental measurement error) at a - very low - rate of 1 nm/s. Figure 29 presents the progression of $\ln(P_0)$ as the function of time in this case. As can be seen, a compressed exponential model is recovered from

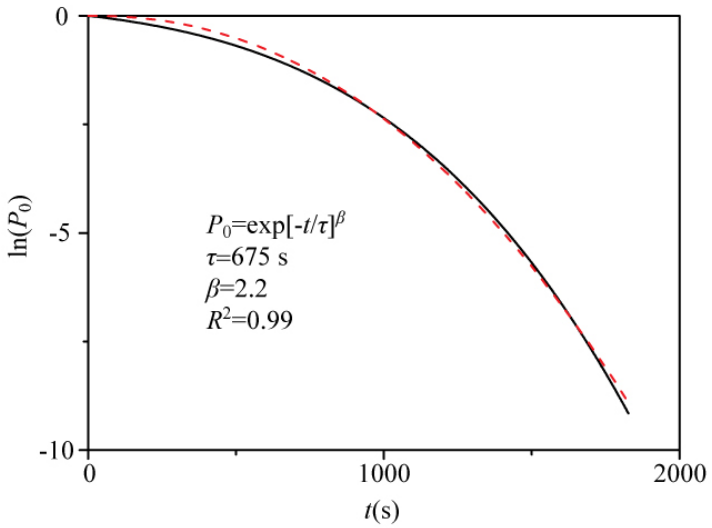

Figure 29: Simulated nucleation statistics in the case of continued slow droplet shrinkage, along with a compressed exponential fit.

the simulated nucleation statistics. However, the evidence for interaction between droplets presented in Chapter 2 suggests that continued shrinkage alone cannot account for the compressed exponential process. Therefore, further experimental investigation and modeling work will be needed to shed light on the importance of these factors and their dependence on operating conditions (such as droplet size, shrinkage rate, and temperature).

Secondly, influencing nucleation through additives is an invaluable tool when dealing with compounds that behave in an undesirable way in their pure form. Beside the drug-excipient co-formulation presented above, one could imagine emulsion droplets laden with functional molecules or particles that template the

nucleation of a desired polymorph, a technique often demonstrated in conventional systems [32], [33], [38], [39], [85]. Furthermore, some solutes might exhibit nucleation rates that are high enough to completely preclude spherulitic growth in microfluidic droplets. Additives that either slow down nucleation or provide conditions that favor spherulitic growth (such as an increased viscosity [193]) could be used to improve chances of SA formation. On the other end of the scale lie solutes that experience a dramatic reduction in nucleation rate at high supersaturations, and end up sitting around in a glassy, melt-like state indefinitely [225]. Investigation of additives that enhance the nucleation of such solutes would obviously be beneficial for the process.

5.3.2 Growth

The growth of spherulites is a well-studied phenomenon in polymeric and metallic melts [192], [193]. However, the difficulty of reaching concentrations conducive of spherulitic growth and the extremely high growth rates have thus far prohibited the *in situ* investigation of spherulitic growth in the context of small organic compounds. With the methods presented in Chapter 2, such investigations become straightforward. In future studies, growth rates could be measured as a function of processing parameters (most notably, temperature), types of spherulitic growth could be observed (category I or II [193]) in different crystallizing materials, and in sufficiently large droplets with sufficiently large shrinkage rates, a switch between spherulitic and diffusion-controlled growth could be observed [191] to precisely identify the concentration at which spherulitic growth still proceeds. These experimental observations could then be complemented with phase-field modeling [193] to extract physical parameters (such as viscosity and rotational and translational diffusivities) in highly supersaturated systems. If a sufficient amount of simulated and experimental data is amassed, the *prediction* of the spherulite-forming tendency of small organic molecules could eventually become possible.

5.3.3 Aging

The final step of SA formation, aging, is very important because of its role in influencing the structure of the SAs - which, in turn, affects their downstream performance, as seen in Chapter 4. In Chapter 2 it was determined that this phenomenon is a solvent-mediated phase transformation in the case of glycine. However, observational and circumstantial evidence indicate that both the rate and extent of aging are highly dependent on both SA size (smaller SAs age less, e.g. see Figure 5 of Chapter 2) and temperature (higher temperature leads to more and faster aging, e.g. see Figure 20 of Chapter 4). In light of these pieces of evidence, it could be hypothesized that because the stochastic nucleation of the α and the β polymorphs occurs at different rates, only in some droplets will the α polymorph also nucleate before trapped water is completely evaporated from the SA. These SAs then undergo solvent-mediated phase transformation, while the SAs with no α-glycine nucleation remain un-aged. In a future setup, a Raman microscope with tunable temperatures could be used to observe the aging of SAs *in situ*. After a statistically significant amount of data has been collected, a mathematical model similar to the one presented in Chapter 3 could be formulated. This model could not only predict aging, but it could also yield nucleation rate parameters for the two polymorphs at different temperatures, an important piece of information currently not available in the literature.

6 Conclusion

In conclusion, this thesis presented the start-to-finish development of a new, continuous and scalable API crystallization platform to produce uniform spherical particles. First, emulsion-based crystallization techniques were combined with droplet microfluidics and off-chip thin film evaporation to produce spherical crystalline agglomerates (SAs) of a model API compound with unprecedented uniformity. Not only did this setup overcome the typical problem associated with batch emulsion crystallization, the polydispersity of the SAs, but it also circumvented the issue of clogging, a typical microfluidic crystallization problem. In addition, on-line microscopic monitoring enabled the observation of the distinct phases of crystallization: droplet shrinkage, stochastic nucleation, spherulitic growth, and agglomerate aging - a solvent-mediated phase transformation process.

Next, the effect of operating conditions (temperature, droplet size, rate of srhinkage) on the morphological outcome of thin-film spherical crystallization from monodisperse emulsions was investigated through experiments and mathematical modeling. It was determined that spherulitic crystal growth [193] is required to form SAs of a reliable quality, which can only be achieved if a critical supersaturation is attained within a droplet before nucleation occurs. This scenario was modeled by using the classical nucleation theory [22] in conjunction with a theory for nucleation in small volumes with time-varying supersaturation [169] to obtain $P_0(t_s)$, the probability of *no* nucleation occurring within a single droplet before attaining critical supersaturation. This calculated probability was compared to f_I , the experimentally observed fraction of complete SAs among the ensemble. The experimental trends were accurately captured by the simulations.

Subsequently, prototypes of a continuous thin-film evaporator were built to complement continuous microfluidic emulsion generation. These prototypes

were capable of producing SAs of good quality at rates on the order of 1-10 g/day. As the second prototype has a volumetric footprint of only ~10 L, scaling the process to industrially relevant rates by parallelization is straightforward.

Finally, future research opportunities opened up by this thesis were described. These include advanced spherical formulation techniques enabled by microfluidics, the industrial implementation of the developed continuous crystallization process, and the use of monodisperse microfluidic emulsions for the fundamental investigation of spherical crystallization.

6.1 List of Publications

6.1.1 Papers

1. **Arpad I. Toldy**, Abu Zayed M. Badruddoza, Lu Zheng, T. Alan Hatton, Rudiyanto Gunawan, Raj Rajagopalan, and Saif A. Khan: *Spherical Crystallization of Glycine from Monodisperse Microfluidic Emulsions*
Crystal Growth & Design, 2012, 12 (8), pp 3977-3982

2. **Arpad I. Toldy**, Lu Zheng, Abu Zayed Md. Badruddoza, T. Alan Hatton, and Saif A. Khan: *Dynamics and Morphological Outcomes in Thin-Film Spherical Crystallization of Glycine from Microfluidic Emulsions: Experimental Studies and Modeling*
Crystal Growth & Design, 2014, 14 (7), pp 3485-3492

3. Abu Zayed Md. Badruddoza, **Arpad I. Toldy**, T. Alan Hatton, and Saif A. Khan: *Functionalized Silica Nanoparticles as Additives for Polymorphic Control in Emulsion-Based Crystallization of Glycine*
Crystal Growth & Design, 2013, 13 (6), pp 2455-2461

4. Reno A.L. Leon, Abu Zayed Md Badruddoza, Lu Zheng, Eunice W.Q. Yeap, **Arpad I. Toldy**, Kay Yan Wong, T. Alan Hatton, and Saif A. Khan: *Highly selective, kinetically driven polymorphic selection in microfluidic emulsion-based pharmaceutical crystallization and formulation*
Crystal Growth & Design, 2015, 15 (1), pp 212218

6.1.2 Conferences

1. **Arpad I. Toldy**, Abu Zayed M. Badruddoza, Lu Zheng, T. Alan Hatton, Rudiyanto Gunawan, Raj Rajagopalan, and Saif A. Khan: *Spherical Crystallization of Glycine from Monodisperse Microfluidic Emulsions*
Gordon Research Conferences, 2012, poster - presented 1st paper

2. **Arpad I. Toldy**, Abu Zayed M. Badruddoza, Lu Zheng, T. Alan Hatton, Rudiyanto Gunawan, Raj Rajagopalan, and Saif A. Khan: *Pharmaceutical Crystal Engineering in Microfluidic Emulsions*
μTAS, 2012, poster

Bibliography

[1] P. T. Anastas and J. C. Warner, *Green chemistry: theory and practice*. Oxford University Press, 2000.

[2] P. T. Anastas and J. B. Zimmerman, "Peer reviewed: design through the 12 principles of green engineering," *Environmental Science & Technology*, vol. 37, no. 5, 94A–101A, 2003.

[3] R. A. Sheldon, "The e factor: fifteen years on," *Green Chemistry*, vol. 9, pp. 1273–1283, 12 2007.

[4] J. A. DiMasi, R. W. Hansen, and H. G. Grabowski, "The price of innovation: new estimates of drug development costs," *Journal of Health Economics*, vol. 22, no. 2, pp. 151 –185, 2003.

[5] P. Suresh and P. K. Basu, "Improving pharmaceutical product development and manufacturing: impact on cost of drug development and cost of goods sold of pharmaceuticals," *Journal of Pharmaceutical Innovation*, vol. 3, no. 3, pp. 175–187, 2008.

[6] C. Jimnez-Gonzlez, C. S. Ponder, R. E. Hannah, *et al.*, "Designing a sustainable pharmaceutical industry: the role of chemical engineers," in *Chemical Engineering in the Pharmaceutical Industry*. John Wiley & Sons, Inc., 2010, pp. 57–65.

[7] A. Leila and S. Henry, "New prescriptions for drug makers: update the plants," *Wall Street Journal*, vol. 9, no. 12, 2003.

[8] "Challenge and opportunity on the critical path to new medical products.," *US Department of Health and Drug Administration*, 2004.

[9] P. McKenzie, S. Kiang, J. Tom, *et al.*, "Can pharmaceutical process development become high tech?" *AIChE Journal*, vol. 52, no. 12, pp. 3990–3994, 2006.

[10] M. Fujiwara, Z. K. Nagy, J. W. Chew, *et al.*, "First-principles and direct design approaches for the control of pharmaceutical crystallization," *Journal of Process Control*, vol. 15, no. 5, pp. 493 –504, 2005.

[11] T. Kourti, "Pharmaceutical manufacturing: the role of multivariate analysis in design space, control strategy, process understanding, troubleshooting, and optimization," in *Chemical Engineering in the Pharmaceutical Industry*. John Wiley & Sons, Inc., 2010, pp. 853–878.

[12] A. I. Stankiewicz and J. A. Moulijn, "Process intensification: transforming chemical engineering," *Chemical Engineering Progress*, vol. 96, no. 1, pp. 22–34, 2000.

[13] S. Mascia, P. L. Heider, H. Zhang, *et al.*, "End-to-end continuous manufacturing of pharmaceuticals: integrated synthesis, purification, and final dosage formation," *Angewandte Chemie International Edition*, vol. 52, no. 47, pp. 12 359–12 363, 2013.

[14] P. L. Heider, S. C. Born, S. Basak, *et al.*, "Development of a multi-step synthesis and workup sequence for an integrated, continuous manufacturing process of a pharmaceutical," *Organic Process Research & Development*, vol. 18, no. 3, pp. 402–409, 2014.

[15] H. Zhang, R. Lakerveld, P. L. Heider, *et al.*, "Application of continuous crystallization in an integrated continuous pharmaceutical pilot plant," *Crystal Growth & Design, Article ASAP*, 2014.

[16] A. S. Myerson, *Handbook of Industrial Crystallization*. Butterworth-Heinemann, 2002.

[17] N. Variankaval, A. S. Cote, and M. F. Doherty, "From form to function: crystallization of active pharmaceutical ingredients," *AIChE Journal*, no. 7, 16821688, 2008.

[18] R. R. McKeown, J. T. Wertman, and P. C. Dell'Orco, "Crystallization design and scale-up," in *Chemical Engineering in the Pharmaceutical Industry*. John Wiley & Sons, Inc., 2010, pp. 213–247.

[19] D. Mangin, F. Puel, and S. Veesler, "Polymorphism in processes of crystallization in solution: a practical review," *Organic Process Research & Development*, vol. 13, no. 6, pp. 1241–1253, 2009.

[20] B. Shekunov and P York, "Crystallization processes in pharmaceutical technology and drug delivery design," *Journal of Crystal Growth*, vol. 211, no. 14, pp. 122 –136, 2000.

[21] J. J. De Yoreo and P. G. Vekilov, "Principles of crystal nucleation and growth," *Reviews in mineralogy and geochemistry*, vol. 54, no. 1, pp. 57–93, 2003.

[22] P. Debenedetti, *Metastable Liquids: Concepts and Principles*, ser. Physical chemistry : science and engineering. Princeton University Press, 1996.

[23] D. Kashchiev and G. M. van Rosmalen, "Review: nucleation in solutions revisited," *Crystal Research and Technology*, vol. 38, no. 7-8, pp. 555–574, 2003.

[24] C. Pina and A. Putnis, "The kinetics of nucleation of solid solutions from aqueous solutions: a new model for calculating non-equilibrium distribution coefficients," *Geochimica et Cosmochimica Acta*, vol. 66, no. 2, pp. 185 –192, 2002.

[25] M. Moscosa-Santillan, O. Bals, H. Fauduet, *et al.*, "Study of batch crystallization and determination of an alternative temperature-time profile by on-line turbidity analysis application to glycine crystallization," *Chemical Engineering Science*, vol. 55, no. 18, pp. 3759 –3770, 2000.

[26] Y. Hu, J. K. Liang, A. S. Myerson, *et al.*, "Crystallization monitoring by raman spectroscopy: simultaneous measurement of desupersaturation profile and polymorphic form in flufenamic acid systems," *Industrial & Engineering Chemistry Research*, vol. 44, no. 5, pp. 1233–1240, 2005.

[27] D. Erdemir, A. Y. Lee, and A. S. Myerson, "Nucleation of crystals from solution: classical and two-step models," *Accounts of Chemical Research*, vol. 42, no. 5, pp. 621–629, 2009.

[28] A. F. Wallace, L. O. Hedges, A. Fernandez-Martinez, *et al.*, "Microscopic evidence for liquid-liquid separation in supersaturated caco3 solutions," *Science*, vol. 341, no. 6148, pp. 885–889, 2013.

[29] K. Chen, L. Goh, G. He, *et al.*, "Identification of nucleation rates in droplet-based microfluidic systems," *Chemical Engineering Science*, vol. 77, no. 0, pp. 235 –241, 2012, 18th International Symposium on Industrial Crystallization.

[30] R. P. Sear, "Estimation of the scaling of the nucleation time with volume when the nucleation rate does not exist," *Crystal Growth & Design*, vol. 13, no. 3, pp. 1329–1333, 2013.

[31] J. Bernstein, *Polymorphism in molecular crystals*. Oxford University Press, 2002, vol. 14.

[32] K. Chadwick, A. Myerson, and B. Trout, "Polymorphic control by heterogeneous nucleation - a new method for selecting crystalline substrates," *CrystEngComm*, vol. 13, pp. 6625–6627, 22 2011.

[33] J. L. Quon, K. Chadwick, G. P. F. Wood, *et al.*, "Templated nucleation of acetaminophen on spherical excipient agglomerates," *Langmuir*, vol. 29, no. 10, pp. 3292–3300, 2013.

[34] J. Aizenberg, A. J. Black, and G. M. Whitesides, "Control of crystal nucleation by patterned self-assembled monolayers," *Nature*, vol. 398, no. 6727, pp. 495–498, 1999.

[35] A. Y. Lee, A. Ulman, and A. S. Myerson, "Crystallization of amino acids on self-assembled monolayers of rigid thiols on gold," *Langmuir*, vol. 18, no. 15, pp. 5886–5898, 2002.

[36] I. S. Lee, K. T. Kim, A. Y. Lee, *et al.*, "Concomitant crystallization of glycine on patterned substrates: the effect of ph on the polymorphic outcome," *Crystal Growth & Design*, vol. 8, no. 1, pp. 108–113, 2008.

[37] A. Singh, I. S. Lee, and A. S. Myerson, "Concomitant crystallization of roy on patterned substrates: using a high throughput method to improve the chances of crystallization of different polymorphs," *Crystal Growth & Design*, vol. 9, no. 2, pp. 1182–1185, 2009.

[38] Y. Diao, T. Harada, A. S. Myerson, *et al.*, "The role of nanopore shape in surface-induced crystallization," *Nature Materials*, vol. 10, no. 11, pp. 867–871, 2011.

[39] Y. Diao, K. E. Whaley, M. E. Helgeson, *et al.*, "Gel-induced selective crystallization of polymorphs," *Journal of the American Chemical Society*, vol. 134, no. 1, pp. 673–684, 2012.

[40] J. Bernstein, "Polymorphism a perspective," *Crystal Growth & Design*, vol. 11, no. 3, pp. 632–650, 2011.

[41] S. R. Chemburkar, J. Bauer, K. Deming, *et al.*, "Dealing with the impact of ritonavir polymorphs on the late stages of bulk drug process development," *Organic Process Research & Development*, vol. 4, no. 5, pp. 413–417, 2000.

[42] J. Bernstein, R. J. Davey, and J.-O. Henck, "Concomitant polymorphs," *Angewandte Chemie International Edition*, vol. 38, no. 23, pp. 3440–3461, 1999.

[43] A. J. Cruz-Cabeza and J. Bernstein, "Conformational polymorphism," *Chemical Reviews*, vol. 114, no. 4, pp. 2170–2191, 2014.

[44] P. T. Cardew, R. J. Davey, and A. J. Ruddick, "Kinetics of polymorphic solid-state transformations," *J. Chem. Soc., Faraday Trans. 2*, vol. 80, pp. 659–668, 6 1984.

[45] P. T. Cardew and R. J. Davey, "The kinetics of solvent-mediated phase transformations," *Proceedings of the Royal Society of London. A. Mathematical and Physical Sciences*, vol. 398, no. 1815, pp. 415–428, 1985.

[46] X. Wang, J. C. D. Anda, and K. Roberts, "Real-time measurement of the growth rates of individual crystal facets using imaging and image analysis: a feasibility study on needle-shaped crystals of l-glutamic acid," *Chemical Engineering Research and Design*, vol. 85, no. 7, pp. 921 – 927, 2007.

[47] P. York, "Solid-state properties of powders in the formulation and processing of solid dosage forms," *International Journal of Pharmaceutics*, vol. 14, no. 1, pp. 1 –28, 1983.

[48] P. Bennema, "Theory of growth and morphology applied to organic crystals; possible applications to protein crystals," *Journal of Crystal Growth*, vol. 122, no. 14, pp. 110 –119, 1992.

[49] M Lahav and L Leiserowitz, "Tailor-made auxiliaries for the control of nucleation, growth and dissolution of two- and three-dimensional crystals," *Journal of Physics D: Applied Physics*, vol. 26, no. 8B, B22, 1993.

[50] I. Weissbuch, R. Popovitz-Biro, M. Lahav, *et al.*, "Understanding and control of nucleation, growth, habit, dissolution and structure of two- and three-dimensional crystals using 'tailor-made' auxiliaries," *Acta Crystallographica Section B*, vol. 51, no. 2, pp. 115–148, 1995.

[51] S. Gnanasambandam and R. Rajagopalan, “Growth morphology of [small alpha]-glycine crystals in solution environments: an extended interface structure analysis,” *CrystEngComm*, vol. 12, pp. 1740–1749, 6 2010.

[52] M. Rhodes, “Particle size reduction,” in *Introduction to Particle Technology*. John Wiley & Sons, Ltd, 2008, pp. 311–335.

[53] M. Warman, “Continuous processing in secondary production,” in *Chemical Engineering in the Pharmaceutical Industry*. John Wiley & Sons, Inc., 2010, pp. 837–851.

[54] K. D. Seibert, P. C. Collins, and E. Fisher, “Milling operations in the pharmaceutical industry,” in *Chemical Engineering in the Pharmaceutical Industry*. John Wiley & Sons, Inc., 2010, pp. 365–378.

[55] A. Bauer-Brandl, “Polymorphic transitions of cimetidine during manufacture of solid dosage forms,” *International Journal of Pharmaceutics*, vol. 140, no. 2, pp. 195 –206, 1996.

[56] J. Ottino and D. Khakhar, “Mixing and segregation of granular materials,” *Annual Review of Fluid Mechanics*, vol. 32, pp. 55–91, 2000.

[57] Z. T. Chowhan and L.-H. Chi, “Drug-excipient interactions resulting from powder mixing iii: solid state properties and their effect on drug dissolution,” *Journal of Pharmaceutical Sciences*, vol. 75, no. 6, pp. 534–541, 1986.

[58] Z. T. Chowhan and L. Chi, “Drug-excipient interactions resulting from powder mixing iv: role of lubricants and their effect on in vitro dissolution,” *Journal of Pharmaceutical Sciences*, vol. 75, no. 6, pp. 542–545, 1986.

[59] U. Sindel, A. Schweiger, and I. Zimmermann, “Determination of the optimum mixing time for a mixture of lactose and colloidal silicon dioxide,” *Journal of Pharmaceutical Sciences*, vol. 87, no. 4, pp. 524–526, 1998.

[60] M. D. Tousey, "The granulation process 101," *Pharm Tech*, pp. 8–13, 2002.

[61] M. W. Wong and A. G. Mitchell, "Physicochemical characterization of a phase change produced during the wet granulation of chlorpromazine hydrochloride and its effects on tableting," *International Journal of Pharmaceutics*, vol. 88, no. 13, pp. 261 –273, 1992.

[62] Y. Kawashima and C. Capes, "An experimental study of the kinetics of spherical agglomeration in a stirred vessel," *Powder Technology*, vol. 10, no. 1-2, pp. 85 –92, 1974.

[63] Y. Kawashima, M. Okomura, and H. Takenaka, "Spherical crystallization: direct spherical agglomeration of salicylic acid crystals during crystallization," *Science*, vol. 216, no. 4550, pp. 1127–1128, 1982.

[64] D. Amaro-Gonzlez and B. Biscans, "Spherical agglomeration during crystallization of an active pharmaceutical ingredient," *Powder Technology*, vol. 128, no. 23, pp. 188 –194, 2002.

[65] S. Patil and S. Sahoo, "Spherical crystallization: a method to improve tabletability," *Research J Pharm Tech. 2009*, vol. 2, no. 2, pp. 234–237, 2009.

[66] M. S. Gordon and Z. T. Chowhan, "Manipulation of naproxen particle morphology via the spherical crystallization technique to achieve a directly compressible raw material," *Drug Development and Industrial Pharmacy*, vol. 16, no. 8, pp. 1279–1290, 1990.

[67] M Jbilou, A Ettabia, A.-M. Guyot-Hermann, *et al.*, "Ibuprofen agglomerates preparation by phase separation," *Drug development and industrial pharmacy*, vol. 25, no. 3, pp. 297–305, 1999.

[68] M Deshpande, K Mahadik, A Pawar, *et al.*, "Evaluation of spherical crystallization as a particle size enlargement technique for aspirin," *Indian journal of pharmaceutical sciences*, vol. 59, no. 1, p. 32, 1997.

[69] Y Kawashima, T Iwamoto, T Niwa, *et al.*, "Role of the solvent-diffusion-rate modifier in a new emulsion solvent diffusion method for preparation of ketoprofen microspheres," *Journal of microencapsulation*, vol. 10, no. 3, pp. 329–340, 1993.

[70] T. Niwa, H. Takeuchi, T. Hino, *et al.*, "Preparation of agglomerated crystals for direct tabletting and microencapsulation by the spherical crystallization technique with a continuous system," *Pharmaceutical research*, vol. 11, no. 4, pp. 478–484, 1994.

[71] Y Kawashima, F Cui, H Takeuchi, *et al.*, "Improvements in flowability and compressibility of pharmaceutical crystals for direct tabletting by spherical crystallization with a two-solvent system," *Powder technology*, vol. 78, no. 2, pp. 151–157, 1994.

[72] F. Espitalier, "Procédé discontinu de cristallisation d'un principe actif pharmaceutique par le mécanisme de quasi-émulsion," PhD thesis, 1994.

[73] F. Espitalier, B. Biscans, J.-R. Authelin, *et al.*, "Modelling of the mechanism of formation of spherical grains obtained by the quasi-emulsion crystallization process," *Chemical Engineering Research and Design*, vol. 75, no. 2, pp. 257 –267, 1997.

[74] M. Nocent, L. Bertocchi, F. Espitalier, *et al.*, "Definition of a solvent system for spherical crystallization of salbutamol sulfate by quasi-emulsion solvent diffusion (qesd) method," *Journal of Pharmaceutical Sciences*, vol. 90, no. 10, pp. 1620–1627, 2001.

[75] F. Espitalier, B. Biscans, and C. Laguerie, "Particle design part b: batch quasi-emulsion process and mechanism of grain formation of ketoprofen," *Chemical Engineering Journal*, vol. 68, no. 2-3, pp. 103 –114, 1997.

[76] M. R and B Biscans, "Preparation of microspheres of ketoprofen with acrylic polymers by a quasi-emulsion solvent diffusion method," *Powder Technology*, vol. 101, no. 2, pp. 120 –133, 1999.

[77] B. Kovačič, F. Vrečer, and O. Planinšek, "Spherical crystallization of drugs," *Acta Pharmaceutica*, vol. 62, no. 1, pp. 1–14, 2012.

[78] M. Tanaka, S. Yamanaka, Y. Shirakawa, *et al.*, "Preparation of porous particles by liquid - liquid interfacial crystallization," *Advanced Powder Technology*, vol. 22, no. 1, pp. 125 –130, 2011.

[79] S. Teychene, N. Sicre, and B. Biscans, "Is spherical crystallization without additives possible?" *Chemical Engineering Research and Design*, vol. 88, no. 12, pp. 1631 –1638, 2010.

[80] K. Kachrimanis, G. Ktistis, and S. Malamataris, "Crystallisation conditions and physicomechanical properties of ibuprofeneudragit {s100} spherical crystal agglomerates prepared by the solvent-change technique," *International Journal of Pharmaceutics*, vol. 173, no. 12, pp. 61 –74, 1998.

[81] B. Sjostrom, B. Kronberg, and J. Carlfors, "A method for the preparation of submicron particles of sparingly water-soluble drugs by precipitation in oil-in-water emulsions. i: influence of emulsification and surfactant concentration," *Journal of Pharmaceutical Sciences*, vol. 82, no. 6, pp. 579–583, 1993.

[82] B. Sjostrom, B. Bergenstahl, and B. Kronberg, "A method for the preparation of submicron particles of sparingly water-soluble drugs by precipitation in oil-in-water emulsions. ii: influence of the emulsifier, the solvent, and the drug substance," *Journal of Pharmaceutical Sciences*, vol. 82, no. 6, pp. 584–589, 1993.

[83] K. Allen, R. J. Davey, E. Ferrari, *et al.*, "The crystallization of glycine polymorphs from emulsions, microemulsions, and lamellar phases," *Crystal Growth & Design*, vol. 2, no. 6, pp. 523–527, 2002.

[84] K. Chadwick, R. J. Davey, R. Mughal, *et al.*, "Crystallisation from water-in-oil emulsions as a route to spherical particulates: glycine and the hydrochloride salts of glutamic acid and ephedrine," *Organic Process Research & Development*, vol. 13, no. 6, pp. 1284–1290, 2009.

[85] A. Z. Md. Badruddoza, A. I. Toldy, T. A. Hatton, *et al.*, "Functionalized silica nanoparticles as additives for polymorphic control in emulsion-based crystallization of glycine," *Crystal Growth & Design*, vol. 13, no. 6, pp. 2455–2461, 2013.

[86] B. Vonnegut, "Variation with temperature of the nucleation rate of supercooled liquid tin and water drops," *Journal of Colloid Science*, vol. 3, no. 6, pp. 563 –569, 1948.

[87] D. Turnbull and R. E. Cech, "Microscopic observation of the solidification of small metal droplets," *Journal of Applied Physics*, vol. 21, no. 8, 1950.

[88] R. P. Sear, "Nucleation of a new phase on a surface that is changing irreversibly with time," *Phys. Rev. E*, vol. 89, p. 022 405, 2 2014.

[89] J. Cordiez, G Grange, and B Mutaftschiev, "Droplet freezing experiments in stearic acid-water emulsions role of the droplet-medium interface," *Journal of Colloid and Interface Science*, vol. 85, no. 2, pp. 431 –441, 1982.

[90] R. J. Davey, J. Garside, A. M. Hilton, *et al.*, "Purification of molecular mixtures below the eutectic by emulsion crystallization," *Nature*, vol. 375, no. 22, pp. 664–666, 1995.

[91] J. N. Coupland, "Crystallization in emulsions," *Current Opinion in Colloid & Interface Science*, vol. 7, no. 56, pp. 445 –450, 2002.

[92] D. J. McClements, "Crystals and crystallization in oil-in-water emulsions: implications for emulsion-based delivery systems," *Advances in Colloid and Interface Science*, vol. 174, no. 0, pp. 1 –30, 2012.

[93] A. Nokhodchi, M. Maghsoodi, D. Hassan-Zadeh, *et al.*, "Preparation of agglomerated crystals for improving flowability and compactibility of poorly flowable and compactible drugs and excipients," *Powder Technology*, vol. 175, no. 2, pp. 73 –81, 2007.

[94] P. D. Martino, C. Barthlmy, F. Piva, *et al.*, "Improved dissolution behavior of fenbufen by spherical crystallization," *Drug Development and Industrial Pharmacy*, vol. 25, no. 10, pp. 1073–1081, 1999.

[95] E. G. Chatzi, A. D. Gavrielides, and C. Kiparissides, "Generalized model for prediction of the steady-state drop size distributions in batch stirred vessels," *Industrial & Engineering Chemistry Research*, vol. 28, no. 11, pp. 1704–1711, 1989.

[96] G. M. Whitesides, "The origins and the future of microfluidics," *Nature*, vol. 442, pp. 368–373, 2006.

[97] D. Qin, Y. Xia, and G. M. Whitesides, "Rapid prototyping of complex structures with feature sizes larger than 20 m," *Advanced Materials*, vol. 8, no. 11, pp. 917–919, 1996.

[98] H. Zorbas, "Miniature continuous-flow polymerase chain reaction: a breakthrough?" *Angewandte Chemie International Edition*, vol. 38, no. 8, pp. 1055–1058, 1999.

[99] T. M. Squires and S. R. Quake, "Microfluidics: fluid physics at the nanoliter scale," *Rev. Mod. Phys.*, vol. 77, pp. 977–1026, 3 2005.

[100] R. L. Hartman, J. P. McMullen, and K. F. Jensen, "Deciding whether to go with the flow: evaluating the merits of flow reactors for synthesis," *Angewandte Chemie International Edition*, vol. 50, no. 33, pp. 7502–7519, 2011.

[101] A. Odedra and P. H. Seeberger, "5-(pyrrolidin-2-yl)tetrazole-catalyzed aldol and mannich reactions: acceleration and lower catalyst loading in a continuous-flow reactor," *Angewandte Chemie International Edition*, vol. 48, no. 15, pp. 2699–2702, 2009.

[102] F. E. Valera, M. Quaranta, A. Moran, *et al.*, "The flows the thing or is it? assessing the merits of homogeneous reactions in flask and flow," *Angewandte Chemie International Edition*, vol. 49, no. 14, pp. 2478–2485, 2010.

[103] L. Saias, J. Autebert, L. Malaquin, *et al.*, "Design, modeling and characterization of microfluidic architectures for high flow rate, small footprint microfluidic systems," *Lab Chip*, vol. 11, pp. 822–832, 5 2011.

[104] J. R. Goodell, J. P. McMullen, N. Zaborenko, *et al.*, "Development of an automated microfluidic reaction platform for multidimensional screening: reaction discovery employing bicyclo[3.2.1]octanoid scaffolds," *The Journal of Organic Chemistry*, vol. 74, no. 16, pp. 6169–6180, 2009.

[105] N. Zaborenko, M. W. Bedore, T. F. Jamison, *et al.*, "Kinetic and scale-up investigations of epoxide aminolysis in microreactors at high temperatures and pressures," *Organic Process Research & Development*, vol. 15, no. 1, pp. 131–139, 2011.

[106] H. Pennemann, V. Hessel, and H. Lwe, "Chemical microprocess technology - from laboratory-scale to production," *Chemical Engineering Science*, vol. 59, no. 2223, pp. 4789 –4794, 2004.

[107] C.-C. Lee, G. Sui, A. Elizarov, *et al.*, "Multistep synthesis of a radiolabeled imaging probe using integrated microfluidics," *Science*, vol. 310, no. 5755, pp. 1793–1796, 2005.

[108] J. Pelleter and F. Renaud, "Facile, fast and safe process development of nitration and bromination reactions using continuous flow reactors,"

Organic Process Research & Development, vol. 13, no. 4, pp. 698–705, 2009.

[109] B. Pieber and C. O. Kappe, "Direct aerobic oxidation of 2-benzylpyridines in a gas-liquid continuous-flow regime using propylene carbonate as a solvent," *Green Chemistry*, vol. 15, pp. 320–324, 2 2013.

[110] T. Asai, A. Takata, Y. Ushiogi, *et al.*, "Switching reaction pathways of benzo[b]thiophen-3-yllithium and benzo[b]furan-3-yllithium based on high-resolution residence-time and temperature control in a flow microreactor," *Chemistry Letters*, vol. 40, no. 4, pp. 393–395, 2011.

[111] A. Shimoyama, Y. Fujimoto, and K. Fukase, "Stereoselective glycosylation of 3-deoxy-d-manno-2-octulosonic acid with batch and microfluidic methods," *Synlett*, vol. 2011, no. 16, pp. 2359–2362, 2011.

[112] H. R. Sahoo, J. G. Kralj, and K. F. Jensen, "Multistep continuous-flow microchemical synthesis involving multiple reactions and separations," *Angewandte Chemie*, vol. 119, no. 30, pp. 5806–5810, 2007.

[113] S. J. Haswell and P. Watts, "Green chemistry: synthesis in micro reactors," *Green Chemistry*, vol. 5, pp. 240–249, 2 2003.

[114] K. S. Elvira, X. C. i Solvas, R. C. Wootton, *et al.*, "The past, present and potential for microfluidic reactor technology in chemical synthesis," *Nature chemistry*, vol. 5, no. 11, 905 915, 2013.

[115] S.-Y. Teh, R. Lin, L.-H. Hung, *et al.*, "Droplet microfluidics," *Lab Chip*, vol. 8, pp. 198–220, 2 2008.

[116] A. Huebner, S. Sharma, M. Srisa-Art, *et al.*, "Microdroplets: a sea of applications?" *Lab Chip*, vol. 8, pp. 1244–1254, 8 2008.

[117] H. Song, J. D. Tice, and R. F. Ismagilov, "A microfluidic system for controlling reaction networks in time," *Angewandte Chemie International Edition*, vol. 42, no. 7, pp. 768–772, 2003.

[118] A. Günther, M. Jhunjhunwala, M. Thalmann, *et al.*, "Micromixing of miscible liquids in segmented gas-liquid flow," *Langmuir*, vol. 21, no. 4, pp. 1547–1555, 2005.

[119] A. J. Demello, "Control and detection of chemical reactions in microfluidic systems.," *Nature*, vol. 442, no. 7101, pp. 394–402, 2006.

[120] S. L. Anna, N. Bontoux, and H. A. Stone, "Formation of dispersions using flow focusing in microchannels," *Applied physics letters*, vol. 82, p. 364, 2003.

[121] D. R. Link, S. L. Anna, D. A. Weitz, *et al.*, "Geometrically mediated breakup of drops in microfluidic devices," *Phys. Rev. Lett.*, vol. 92, p. 054 503, 5 2004.

[122] C. N. Baroud and H. Willaime, "Multiphase flows in microfluidics," *Comptes Rendus Physique*, vol. 5, no. 5, pp. 547 –555, 2004.

[123] P. Garstecki, M. J. Fuerstman, H. A. Stone, *et al.*, "Formation of droplets and bubbles in a microfluidic t-junctionscaling and mechanism of breakup," *Lab on a Chip*, vol. 6, no. 3, pp. 437–446, 2006.

[124] G. F. Christopher and S. L. Anna, "Microfluidic methods for generating continuous droplet streams," *Journal of Physics D: Applied Physics*, vol. 40, no. 19, R319, 2007.

[125] A. S. Utada, L.-Y. Chu, A. Fernandez-Nieves, *et al.*, "Dripping, jetting, drops, and wetting: the magic of microfluidics," *MRS Bulletin*, vol. 32, pp. 702–708, 2007.

[126] A. Utada, E. Lorenceau, D. Link, *et al.*, "Monodisperse double emulsions generated from a microcapillary device," *Science*, vol. 308, no. 5721, pp. 537–541, 2005.

[127] L.-Y. Chu, A. S. Utada, R. K. Shah, *et al.*, "Controllable monodisperse multiple emulsions," *Angewandte Chemie International Edition*, vol. 46, no. 47, pp. 8970–8974, 2007.

[128] S Torza and S. Mason, "Three-phase interactions in shear and electrical fields," *Journal of Colloid and Interface Science*, vol. 33, no. 1, pp. 67 –83, 1970.

[129] X. Feng, Y. Yi, X. Yu, *et al.*, "Generation of water-ionic liquid droplet pairs in soybean oil on microfluidic chip," *Lab Chip*, vol. 10, pp. 313–319, 3 2010.

[130] Z. Barikbin, M. T. Rahman, P. Parthiban, *et al.*, "Ionic liquid-based compound droplet microfluidics for 'on-drop' separations and sensing," *Lab Chip*, vol. 10, pp. 2458–2463, 18 2010.

[131] S. Hui Sophia Lee, P. Wang, S. Kun Yap, *et al.*, "Tunable spatial heterogeneity in structure and composition within aqueous microfluidic droplets," *Biomicrofluidics*, vol. 6, no. 2, pp. 022 005–, 2012.

[132] M. Hashimoto, P. Garstecki, and G. Whitesides, "Synthesis of composite emulsions and complex foams with the use of microfluidic flow-focusing devices," *Small*, vol. 3, no. 10, pp. 1792–1802, 2007.

[133] S. A. Khan and S. Duraiswamy, "Microfluidic emulsions with dynamic compound drops," *Lab Chip*, vol. 9, pp. 1840–1842, 13 2009.

[134] H. Song, D. L. Chen, and R. F. Ismagilov, "Reactions in droplets in microfluidic channels," *Angewandte Chemie International Edition*, vol. 45, no. 44, pp. 7336–7356, 2006.

[135] J.-T. Wang, J. Wang, and J.-J. Han, "Fabrication of advanced particles and particle-based materials assisted by droplet-based microfluidics," *small*, vol. 7, no. 13, pp. 1728–1754, 2011.

[136] J. H. Kim, T. Y. Jeon, T. M. Choi, *et al.*, "Droplet microfluidics for producing functional microparticles," *Langmuir*, vol. 30, no. 6, pp. 1473–1488, 2014.

[137] T. Nisisako, T. Torii, and T. Higuchi, "Novel microreactors for functional polymer beads," *Chemical Engineering Journal*, vol. 101, no. 13, pp. 23 –29, 2004.

[138] D. Dendukuri, K. Tsoi, T. A. Hatton, *et al.*, "Controlled synthesis of nonspherical microparticles using microfluidics," *Langmuir*, vol. 21, no. 6, pp. 2113–2116, 2005.

[139] M. Seo, Z. Nie, S. Xu, *et al.*, "Continuous microfluidic reactors for polymer particles," *Langmuir*, vol. 21, no. 25, pp. 11 614–11 622, 2005.

[140] D. Dendukuri, D. C. Pregibon, J. Collins, *et al.*, "Continuous-flow lithography for high-throughput microparticle synthesis," *Nature materials*, vol. 5, no. 5, pp. 365–369, 2006.

[141] D. Dendukuri, S. S. Gu, D. C. Pregibon, *et al.*, "Stop-flow lithography in a microfluidic device," *Lab Chip*, vol. 7, pp. 818–828, 7 2007.

[142] D. C. Pregibon, M. Toner, and P. S. Doyle, "Multifunctional encoded particles for high-throughput biomolecule analysis," *Science*, vol. 315, no. 5817, pp. 1393–1396, 2007.

[143] J. Ugelstad, L. Söderberg, A. Berge, *et al.*, "Monodisperse polymer particles-a step forward for chromatography," *Nature*, vol. 303, pp. 95–96, 1983.

[144] M. T. Rahman, Z. Barikbin, A. Z. M. Badruddoza, *et al.*, "Monodisperse polymeric ionic liquid microgel beads with multiple chemically switchable functionalities," *Langmuir*, vol. 29, no. 30, pp. 9535–9543, 2013.

[145] S. Dubinsky, H. Zhang, Z. Nie, *et al.*, "Microfluidic synthesis of macroporous copolymer particles," *Macromolecules*, vol. 41, no. 10, pp. 3555–3561, 2008.

[146] R. K. Shah, J.-W. Kim, and D. A. Weitz, "Janus supraparticles by induced phase separation of nanoparticles in droplets," *Advanced Materials*, vol. 21, no. 19, pp. 1949–1953, 2009.

[147] R. K. Shah, J. Kim, and D. A. Weitz, "Monodisperse stimuli-responsive colloidosomes by self-assembly of microgels in droplets," *Langmuir*, vol. 26, no. 3, pp. 1561–1565, 2010.

[148] J. L. Steinbacher, R. W. Y. Moy, K. E. Price, *et al.*, "Rapid self - assembly of core - shell organosilicon microcapsules within a microfluidic device," *Journal of the American Chemical Society*, vol. 128, no. 29, pp. 9442–9447, 2006.

[149] S. H. Sophia Lee, M. K. Dawood, W. K. Choi, *et al.*, "Hierarchical materials synthesis at soft all-aqueous interfaces," *Soft Matter*, vol. 8, pp. 3924–3928, 14 2012.

[150] O. D. Velev, A. M. Lenhoff, and E. W. Kaler, "A class of microstructured particles through colloidal crystallization," *Science*, vol. 287, no. 5461, pp. 2240–2243, 2000.

[151] G.-R. Yi, V. Manoharan, S. Klein, *et al.*, "Monodisperse micrometer-scale spherical assemblies of polymer particles," *Advanced Materials*, vol. 14, no. 16, pp. 1137–1140, 2002.

[152] H. C. Shum, J.-W. Kim, and D. A. Weitz, "Microfluidic fabrication of monodisperse biocompatible and biodegradable polymersomes with controlled permeability," *Journal of the American Chemical Society*, vol. 130, no. 29, pp. 9543–9549, 2008.

[153] L. Liu, J.-P. Yang, X.-J. Ju, *et al.*, "Monodisperse core-shell chitosan microcapsules for ph-responsive burst release of hydrophobic drugs," *Soft Matter*, vol. 7, pp. 4821–4827, 10 2011.

[154] Z. Nie, S. Xu, M. Seo, *et al.*, "Polymer particles with various shapes and morphologies produced in continuous microfluidic reactors," *Journal of the American Chemical Society*, vol. 127, no. 22, pp. 8058–8063, 2005.

[155] J. Leng and J.-B. Salmon, "Microfluidic crystallization," *Lab on a Chip*, vol. 9, no. 1, pp. 24–34, 2009.

[156] S. Blundell and K. M. Blundell, *Concepts in thermal physics*. Oxford University Press, 2006.

[157] D. Turnbull, "Kinetics of solidification of supercooled liquid mercury droplets," *The Journal of Chemical Physics*, vol. 20, no. 3, 1952.

[158] G. M. Pound and V. K. L. Mer, "Kinetics of crystalline nucleus formation in supercooled liquid tin1,2," *Journal of the American Chemical Society*, vol. 74, no. 9, pp. 2323–2332, 1952.

[159] D. Kashchiev, N. Kaneko, and K. Sato, "Kinetics of crystallization in polydisperse emulsions," *Journal of Colloid and Interface Science*, vol. 208, no. 1, pp. 167 –177, 1998.

[160] M. L. White and A. A. Frost, "The rate of nucleation of supersaturated potassium nitrate solutions," *Journal of Colloid Science*, vol. 14, no. 3, pp. 247 –251, 1959.

[161] P. Laval, J.-B. Salmon, and M. Joanicot, "A microfluidic device for investigating crystal nucleation kinetics," *Journal of Crystal Growth*, vol. 303, no. 2, pp. 622 –628, 2007.

[162] G. He, V. Bhamidi, R. B. H. Tan, *et al.*, "Determination of critical supersaturation from microdroplet evaporation experiments," *Crystal Growth & Design*, vol. 6, no. 5, pp. 1175–1180, 2006.

[163] R. D. Dombrowski, J. D. Litster, N. J. Wagner, *et al.*, "Crystallization of alpha-lactose monohydrate in a drop-based microfluidic crystallizer," *Chemical Engineering Science*, vol. 62, no. 17, pp. 4802 –4810, 2007.

[164] S. Teychene and B. Biscans, "Microfluidic device for the crystallization of organic molecules in organic solvents," *Crystal Growth & Design*, vol. 11, no. 11, pp. 4810–4818, 2011.

[165] T. Gong, J. Shen, Z. Hu, *et al.*, "Nucleation rate measurement of colloidal crystallization using microfluidic emulsion droplets," *Langmuir*, vol. 23, no. 6, pp. 2919–2923, 2007.

[166] A. Sanjoh and T. Tsukihara, "Spatiotemporal protein crystal growth studies using microfluidic silicon devices," *Journal of Crystal Growth*, vol. 196, no. 24, pp. 691 –702, 1999.

[167] D. Knezic, J. Zaccaro, and A. S. Myerson, "Nucleation induction time in levitated droplets," *The Journal of Physical Chemistry B*, vol. 108, no. 30, pp. 10 672–10 677, 2004.

[168] M. Ildefonso, E. Revalor, P. Punniam, *et al.*, "Nucleation and polymorphism explored via an easy-to-use microfluidic tool," *Journal of Crystal Growth*, vol. 342, no. 1, pp. 9 –12, 2012, 6th National Congress on Industrial Crystallization (CRISTAL-6).

[169] L. Goh, K. Chen, V. Bhamidi, *et al.*, "A stochastic model for nucleation kinetics determination in droplet-based microfluidic systems," *Crystal Growth & Design*, vol. 10, no. 6, pp. 2515–2521, 2010.

[170] N. E. Chayen, "Tackling the bottleneck of protein crystallization in the post-genomic era," *Trends in Biotechnology*, vol. 20, no. 3, pp. 98 –, 2002.

[171] C. L. Hansen, E. Skordalakes, J. M. Berger, *et al.*, "A robust and scalable microfluidic metering method that allows protein crystal growth by free interface diffusion," *Proceedings of the National Academy of Sciences*, vol. 99, no. 26, pp. 16 531–16 536, 2002.

[172] G. Jurez-Martnez, P. Steinmann, A. W. Roszak, *et al.*, "High-throughput screens for postgenomics: studies of protein crystallization using microsystems technology," *Analytical Chemistry*, vol. 74, no. 14, pp. 3505–3510, 2002.

[173] B. Zheng, L. S. Roach, and R. F. Ismagilov, "Screening of protein crystallization conditions on a microfluidic chip using nanoliter-size droplets," *Journal of the American Chemical Society*, vol. 125, no. 37, pp. 11 170–11 171, 2003.

[174] L. Li, D. Mustafi, Q. Fu, *et al.*, "Nanoliter microfluidic hybrid method for simultaneous screening and optimization validated with crystallization of membrane proteins," *Proceedings of the National Academy of Sciences*, vol. 103, no. 51, pp. 19 243–19 248, 2006.

[175] C. L. Hansen, S. Classen, J. M. Berger, *et al.*, "A microfluidic device for kinetic optimization of protein crystallization and in situ structure determination," *Journal of the American Chemical Society*, vol. 128, no. 10, pp. 3142–3143, 2006.

[176] C. J. Gerdts, V. Tereshko, M. K. Yadav, *et al.*, "Time-controlled microfluidic seeding in nl-volume droplets to separate nucleation and growth stages of protein crystallization," *Angewandte Chemie International Edition*, vol. 45, no. 48, pp. 8156–8160, 2006.

[177] J.-u. Shim, G. Cristobal, D. R. Link, *et al.*, "Control and measurement of the phase behavior of aqueous solutions using microfluidics," *Journal of the American Chemical Society*, vol. 129, no. 28, pp. 8825–8835, 2007.

[178] A. Y. Lee, I. S. Lee, S. S. Dette, *et al.*, "Crystallization on confined engineered surfaces: a method to control crystal size and generate different polymorphs," *Journal of the American Chemical Society*, vol. 127, no. 43, pp. 14 982–14 983, 2005.

[179] J. Leng, B. Lonetti, P. Tabeling, *et al.*, "Microevaporators for kinetic exploration of phase diagrams," *Phys. Rev. Lett.*, vol. 96, p. 084 503, 8 2006.

[180] P. Laval, C. Giroux, J. Leng, *et al.*, "Microfluidic screening of potassium nitrate polymorphism," *Journal of Crystal Growth*, vol. 310, no. 12, pp. 3121 –3124, 2008.

[181] S. Duraiswamy and S. A. Khan, "Droplet-based microfluidic synthesis of anisotropic metal nanocrystals," *Small*, vol. 5, no. 24, pp. 2828–2834, 2009.

[182] M. Sultana and K. F. Jensen, "Microfluidic continuous seeded crystallization: extraction of growth kinetics and impact of impurity on morphology," *Crystal Growth & Design*, vol. 12, no. 12, pp. 6260–6266, 2012.

[183] M. Sultana, "Microfluidic systems for continuous crystallization of small organic molecules," PhD thesis, Massachusetts Institute of Technology, 2010.

[184] K. Jasch, N. Barth, S. Fehr, *et al.*, "A microfluidic approach for a continuous crystallization of drug carrier nanoparticles," *Chemical Engineering & Technology*, vol. 32, no. 11, pp. 1806–1814, 2009.

[185] J. Thiele, M. Windbergs, A. R. Abate, *et al.*, "Early development drug formulation on a chip: fabrication of nanoparticles using a microfluidic spray dryer," *Lab Chip*, vol. 11, pp. 2362–2368, 14 2011.

[186] R. Amelia, W. D. Wu, J. Cashion, *et al.*, "Microfluidic spray drying as a versatile assembly route of functional particles," *Chemical Engineering Science*, vol. 66, no. 22, pp. 5531 –5540, 2011.

[187] J. Kim and S. A. Vanapalli, "Microfluidic production of spherical and nonspherical fat particles by thermal quenching of crystallizable oils," *Langmuir*, vol. 29, no. 39, pp. 12 307–12 316, 2013.

[188] S. Sugiura, M. Nakajima, J. Tong, *et al.*, "Preparation of monodispersed solid lipid microspheres using a microchannel emulsification technique," *Journal of Colloid and Interface Science*, vol. 227, no. 1, pp. 95 –103, 2000.

[189] B. J. Sun, H. C. Shum, C. Holtze, *et al.*, "Microfluidic melt emulsification for encapsulation and release of actives," *ACS Applied Materials & Interfaces*, vol. 2, no. 12, pp. 3411–3416, 2010.

[190] S.-H. Kim, S. Y. Lee, G.-R. Yi, *et al.*, "Microwave-assisted self-organization of colloidal particles in confining aqueous droplets," *Journal of the American Chemical Society*, vol. 128, no. 33, pp. 10 897–10 904, 2006.

[191] H. D. Keith and J. F. J. Padden, "A phenomenological theory of spherulitic crystallization," *Journal of Applied Physics*, vol. 34, no. 8, pp. 2409–2421, 1963.

[192] N. Goldenfeld, "Theory of spherulitic crystallization," *Journal of Crystal Growth*, vol. 84, no. 4, pp. 601 –608, 1987.

[193] L. Gránásy, T. Pusztai, G. Tegze, *et al.*, "Growth and form of spherulites," *Phys. Rev. E*, vol. 72, p. 011 605, 1 2005.

[194] S. K. Poornachary, P. S. Chow, and R. B. H. Tan, "Influence of solution speciation of impurities on polymorphic nucleation in glycine," *Crystal Growth & Design*, vol. 8, no. 1, pp. 179–185, 2008.

[195] S. M. Ross, *Simulation*. Elsevier Academic Press, 2006, p. 32.

[196] C. Chen, O. Cook, C. E. Nicholson, *et al.*, "Leapfrogging ostwalds rule of stages: crystallization of stable -glycine directly from microemulsions," *Crystal Growth & Design*, vol. 11, no. 6, pp. 2228–2237, 2011.

[197] P. Laval, A. Crombez, and J.-B. Salmon, "Microfluidic droplet method for nucleation kinetics measurements," *Langmuir*, vol. 25, no. 3, pp. 1836–1841, 2009.

[198] Y. C. Chang and A. S. Myerson, "Diffusivity of glycine in concentrated saturated and supersaturated aqueous solutions," *AIChE Journal*, vol. 32, no. 9, pp. 1567–1569, 1986.

[199] A. I. Toldy, A. Z. M. Badruddoza, L. Zheng, *et al.*, "Spherical crystallization of glycine from monodisperse microfluidic emulsions," *Crystal Growth & Design*, vol. 12, no. 8, pp. 3977–3982, 2012.

[200] W. Ostwald, M. Bodenstein, K. Clusius, *et al.*, *Zeitschrift für physikalische Chemie*, v. 22. Akademische Verlagsgesellschaft Geest & Portig, 1897.

[201] X. Yang, J. Lu, X. Wang, *et al.*, "In situ monitoring of the solution-mediated polymorphic transformation of glycine: characterization of the polymorphs and observation of the transformation rate using raman spectroscopy and microscopy," *Journal of Raman Spectroscopy*, vol. 39, no. 10, pp. 1433–1439, 2008.

[202] N. V. Surovtsev, S. V. Adichtchev, V. K. Malinovsky, *et al.*, "Glycine phases formed from frozen aqueous solutions: revisited," *The Journal of Chemical Physics*, vol. 137, no. 6, 065103, pp. –, 2012.

[203] R. A. L. Leon, W. Y. Wan, A. Z. M. Badruddoza, *et al.*, "Simultaneous spherical crystallization and co-formulation of drug(s) and excipient from microfluidic double emulsions," *Crystal Growth & Design*, vol. 14, no. 1, pp. 140–146, 2014.

[204] N. P. Funnell, A. Dawson, D. Francis, *et al.*, "The effect of pressure on the crystal structure of l-alanine," *CrystEngComm*, vol. 12, pp. 2573–2583, 9 2010.

[205] B. Garetz and A. Myerson, *Method for producing crystal polymorphs and crystal polymorphs produced thereby*, US Patent App. 10/056,490, 2002.

[206] G. Perlovich, L. Hansen, and A. Bauer-Brandl, “The polymorphism of glycine. thermochemical and structural aspects,” *Journal of Thermal Analysis and Calorimetry*, vol. 66, no. 3, pp. 699–715, 2001.

[207] E. S. Ferrari, R. J. Davey, W. I. Cross, *et al.*, “Crystallization in polymorphic systems: the solution-mediated transformation of to glycine,” *Crystal Growth & Design*, vol. 3, no. 1, pp. 53–60, 2003.

[208] C. P. M. Roelands, J. H. ter Horst, H. J. M. Kramer, *et al.*, “Precipitation mechanism of stable and metastable polymorphs of l-glutamic acid,” *AIChE Journal*, vol. 53, no. 2, pp. 354–362, 2007.

[209] R. Beck, D. Malthe-Srenssen, and J.-P. Andreassen, “Polycrystalline growth in precipitation of an aromatic amine derivative and l-glutamic acid,” *Journal of Crystal Growth*, vol. 311, no. 2, pp. 320 –326, 2009.

[210] J.-P. Andreassen, E. M. Flaten, R. Beck, *et al.*, “Investigations of spherulitic growth in industrial crystallization,” *Chemical Engineering Research and Design*, vol. 88, no. 9, pp. 1163 –1168, 2010, Special Issue 17th International Symposium on Industrial Crystallization.

[211] R. Beck, E. Flaten, and J.-P. Andreassen, “Influence of crystallization conditions on the growth of polycrystalline particles,” *Chemical Engineering & Technology*, vol. 34, no. 4, pp. 631–638, 2011.

[212] J. Christoffersen, E. Rostrup, and M. Christoffersen, “Relation between interfacial surface tension of electrolyte crystals in aqueous suspension and their solubility; a simple derivation based on surface nucleation,” *Journal of Crystal Growth*, vol. 113, no. 34, pp. 599 –605, 1991.

[213] R. C. Houck, “A note on the density of glycine.,” *Journal of the American Chemical Society*, vol. 52, no. 6, pp. 2420–2420, 1930.

[214] H.-S. Na, S. Arnold, and A. S. Myerson, “Cluster formation in highly supersaturated solution droplets,” *Journal of Crystal Growth*, vol. 139, no. 12, pp. 104 –112, 1994.

[215] O. Grineva and E. Belyaeva, "Structure of water-glycine solutions in saturated and near-saturated regions according to compressibility data," *Journal of Structural Chemistry*, vol. 52, no. 6, pp. 1139–1143, 2011.

[216] P. Moschou, M. H. de Croon, J. van der Schaaf, *et al.*, "Advances in continuous crystallization: toward microfluidic systems," *Reviews in Chemical Engineering*, vol. 30, no. 2, pp. 127–138, 2014.

[217] D. Conchouso, D. Castro, S. A. Khan, *et al.*, "Three-dimensional parallelization of microfluidic droplet generators for high-volume production (1 l/hr) of monodisperse emulsions," *Lab on a Chip*, vol. Submitted, 2014.

[218] Y. Yuan and T. Lee, "Contact angle and wetting properties," English, in *Surface Science Techniques*, ser. Springer Series in Surface Sciences, G. Bracco and B. Holst, Eds., vol. 51, Springer Berlin Heidelberg, 2013, pp. 3–34.

[219] M. Jivraj, L. G. Martini, and C. M. Thomson, "An overview of the different excipients useful for the direct compression of tablets," *Pharmaceutical Science & Technology Today*, vol. 3, no. 2, pp. 58 –63, 2000.

[220] S. Chen, I. A. Guzei, and L. Yu, "New polymorphs of roy and new record for coexisting polymorphs of solved structures," *Journal of the American Chemical Society*, vol. 127, no. 27, pp. 9881–9885, 2005.

[221] A. Oron, S. H. Davis, and S. G. Bankoff, "Long-scale evolution of thin liquid films," *Reviews of modern physics*, vol. 69, no. 3, p. 931, 1997.

[222] W. Li, J. Greener, D. Voicu, *et al.*, "Multiple modular microfluidic (m3) reactors for the synthesis of polymer particles," *Lab on a Chip*, vol. 9, no. 18, pp. 2715–2721, 2009.

[223] E Amstad, S. Datta, and D. Weitz, "The microfluidic post-array device: high throughput production of single emulsion drops," *Lab on a Chip*, vol. 14, no. 4, pp. 705–709, 2014.

[224] R. Dangla, S. C. Kayi, and C. N. Baroud, “Droplet microfluidics driven by gradients of confinement,” *Proceedings of the National Academy of Sciences*, vol. 110, no. 3, pp. 853–858, 2013.

[225] D. Turnbull, “Under what conditions can a glass be formed?” *Contemporary physics*, vol. 10, no. 5, pp. 473–488, 1969.

Appendices

A Supporting Information for Chapter 2

A.1 Fabrication of Capillary Microfluidic Devices

A schematic of the assembly and a photograph of the capillary microfluidic devices used in our experiments is provided in Figure 30. Square (ID=1 mm) and round (ID=0.8 mm, OD=1 mm) borosilicate capillaries were purchased from VitroCom Inc. A micropipette puller (Sutter Instruments P-97) was used to pull the round capillaries. Pulled capillaries were broken manually to produce tapered capillaries with different nozzle diameters. The capillaries were all functionalized with Trichloro-(1H,1H,2H,2H-perfluorooctyl)-silane under vacuum for 8 hours in order to render their surfaces hydrophobic. Teflon tubing (VICI, OD=1/16 in, ID=0.01 in) was used to connect the capillary device to the syringes containing the continuous and dispersed phases (CP and DP, respectively). The same were used as outlets. Silicone rubber transition tubes (Saint Gobain, ID=1 mm, OD=3 mm) were used to connect the inlets to the square capillaries. Fittings were purchased from Upchurch Scientific. DEVCON 5 min Epoxy was used to seal the connection between the square capillaries and the transition tubes.

A.2 Droplet Breakup

Figures 31, 32, 33, and 34 show droplet breakup images taken at 200 frames per second under the four conditions shown in the paper. As mentioned above, manually broken capillaries were used. Although it would be desirable to work with perfectly regular tips, droplet breakup was sufficiently reliable for our work, as confirmed by subsequent size distribution measurements on droplets.

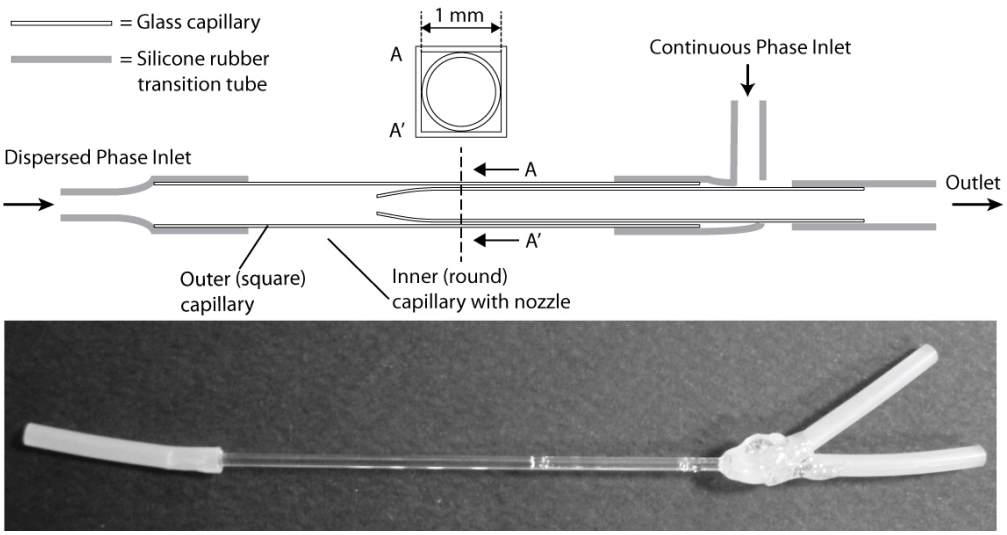

Figure 30: Schematic and photograph of a capillary microfluidic device used in our experiments. A tapered round capillary (OD=1 mm) is inserted into a square capillary (ID=1 mm). The two ends of the square capillary function as inlets, and the round capillary functions as a collection tube/outlet. Silicone rubber transition tubes are used to connect the capillaries to the standard Teflon microfluidic tubing connected to the syringe pumps (not shown on figure).

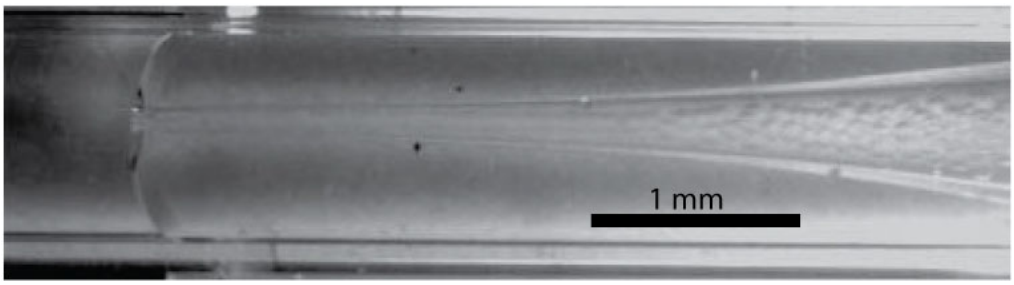

Figure 31: Droplet breakup in the narrow device at Q_{CP} =100 μL/min, Q_{DP}=20 μL/min. Droplet diameter was measured to be 80 μm with a standard deviation of ~1%.

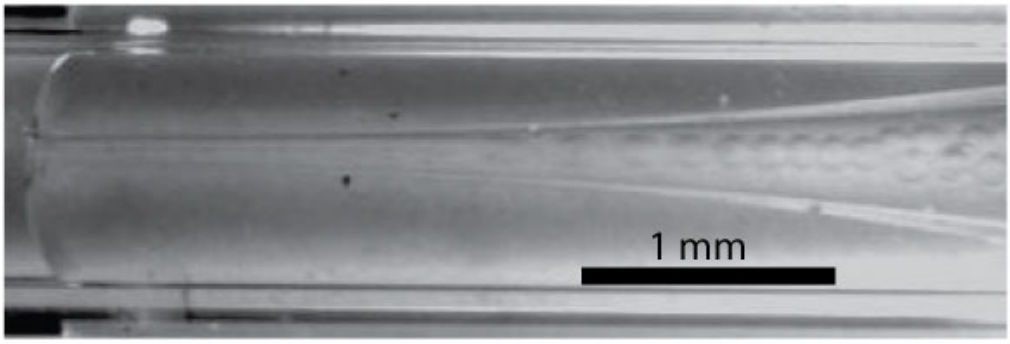

Figure 32: Droplet breakup in the narrow device at Q_{CP} =100 μL/min, Q_{DP}=30 μL/min. Droplet diameter was measured to be 115 μm with a standard deviation of ~1%.

Figure 33: Droplet breakup in the wide device at Q_{CP} =1000 μL/min, Q_{DP}=20 μL/min. Droplet diameter was measured to be 210 μm with a standard deviation of ~1%.

Figure 34: Droplet breakup in the wide device at Q_{CP} =1000 μL/min, Q_{DP}=40 μL/min. Droplet diameter was measured to be 310 μm with a standard deviation of ~1%.

A.3 Observational Evidence of SA-Triggered Nucleation

Figure 35 shows an instance of nucleation triggered by the formation of a spherical agglomerate in the immediate vicinity of a droplet in a populations of 45 μm SAs under indentical conditions to the one presented in the manuscript.

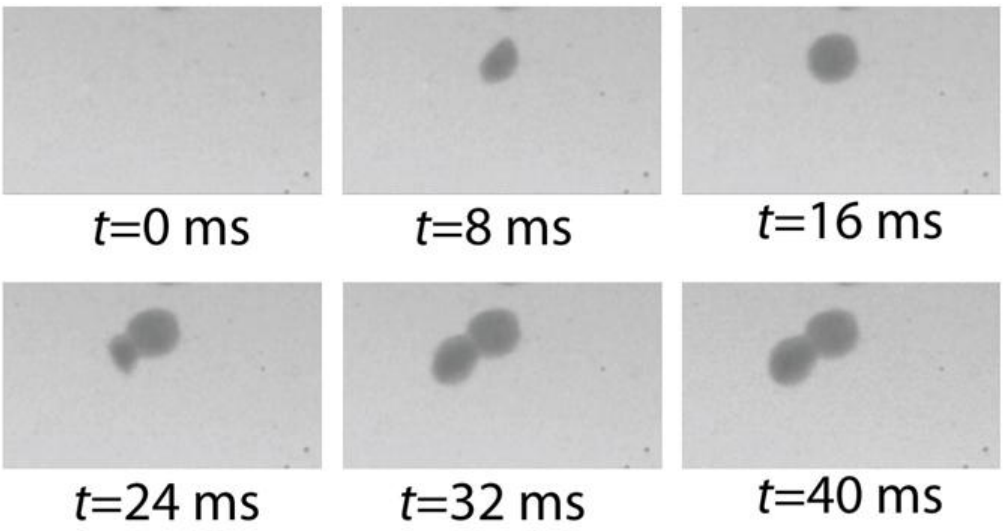

Figure 35: Observational evidence of nucleation triggered by an adjacent spherical agglomerate.

A.4 Microscopic Observation of the Aging Phenomenon

Figure 36 shows a series of micrographs for a typical aging event. It can be seen that the initial agglomerate visibly coarsens from an initially uniform and smooth (black) optical texture in the matter of a few seconds.

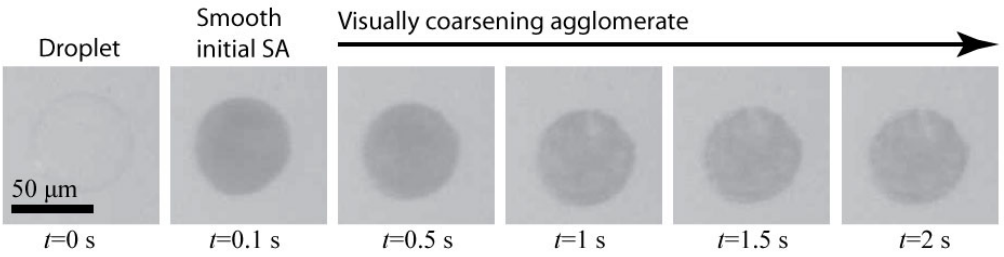

Figure 36: Aging of a ~50 μm glycine spherical agglomerate.

B Supporting Information for Chapter 3

B.1 The relationship between film thickness and shrinkage at a constant temperature

Figure 37 presents an empirical relationship between the effective film thickness h_e , (defined as $h_f - d_0$, where h_f is the dispensed film thickness, and d_0 is the initial droplet diameter) and the linear shrinkage rate d' at T =65 °C for all nine experiments at this temperature. It can be seen that as the film thickness increases, the shrinkage rate decreases with the cube of the film thickness. In a purely diffusive case, we could expect a linear decrease, which suggests the presence of a convective enhancement (possibly due to natural convection) in this system.

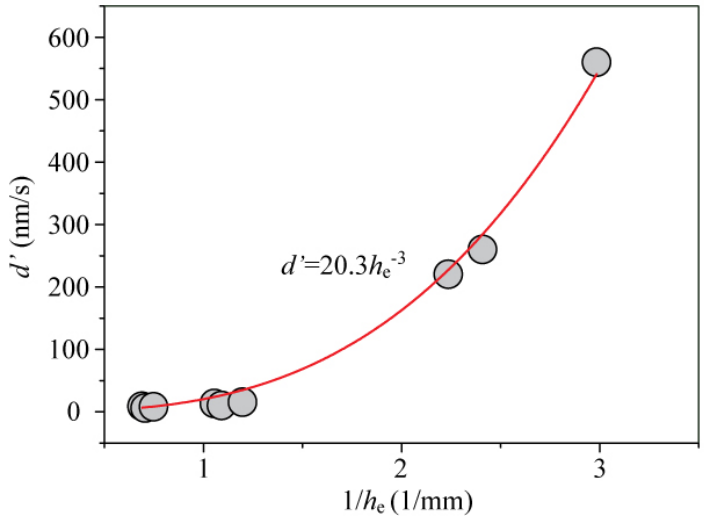

Figure 37: An empirical relationship between the effective film thickness h_e , (defined as $h_f - d_0$, where h_f is the dispensed film thickness, and d_0 is the initial droplet diameter) and the linear shrinkage rate d' at T =65 °C for all nine experiments at this temperature

B.2 The calculated values of classical nucleation theory parameters

Table 6 presents the calculated values of CNT parameters at the temperatures used in this study, while Figure 38 shows the parameter B as a function of continuous phase temperature. Fitted B values were used for modeling.

Table 6: The calculated value of classical nucleation parameters under the temperatures used in this study. #: experiment label (as seen in Table 2 and Table 4); T : heating temperature; T_{CP} : measured continuous phase temperature; σ : interfacial tension between the nucleus and the crystallizing solution; B : dimensionless exponent B .

#	T	T_{CP}	σ	B
	°C	°C	mJ/m^2	
10	45	39	12.8	2.69
V3	50	45	12.4	2.28
11, V1	55	48	12.2	2.13
V4	60	52	11.9	1.89
1-9, V5	65	59	11.5	1.59
V6	70	63	11.2	1.44
12, V2	75	68	11.0	1.27
13	85	78	10.5	1.03

B.3 Fitting of the CNT parameter *A*

B.4 Shrinkage Rate and Temperature

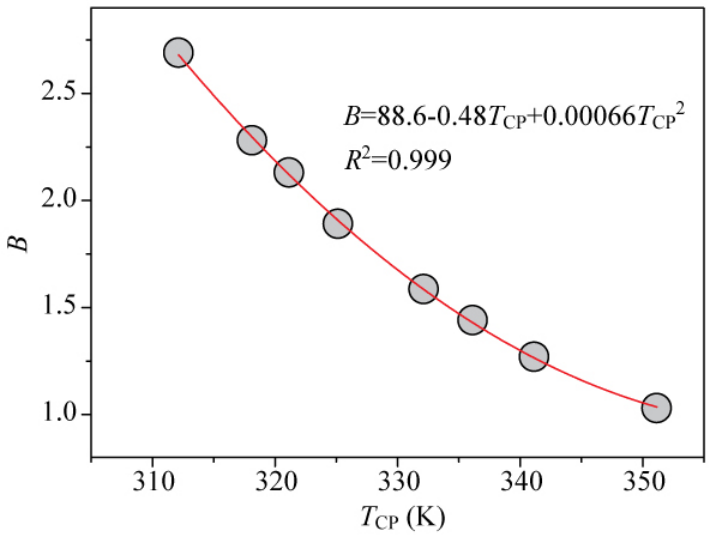

Figure 38: Parameter B as a function of continuous phase temperature along with the polynomial fit used for modeling.

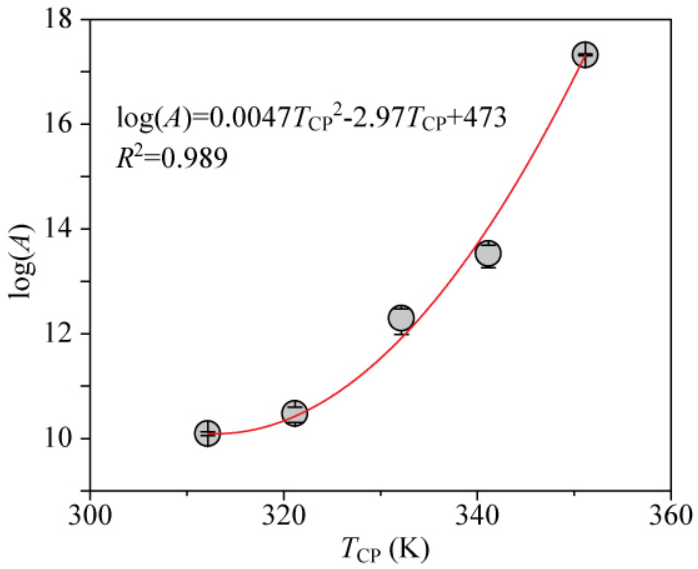

Figure 39: Experimentally derived $log(A)$ values as a function of continuous phase temperature along with the fitted quadratic curve that was used in the modeling. This fit implies that the relationship is of the form $A = A_0 \exp[f(T)]$, which is consistent with previous reports [24].

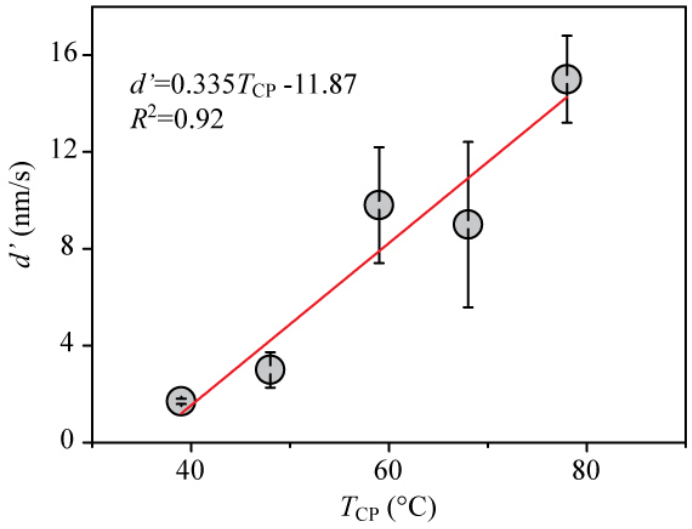

Figure 40: Experimentally measured shrinkage rates at various continuous phase temperature along with the linear fit used in the simulations for Figure 16d.